Dynamic Functional Polymer Networks based on Reversible Bonds

Zur Erlangung des akademischen Grades eines

DOKTORS DER NATURWISSENSCHAFTEN

(Dr. rer. nat.)

von der KIT-Fakultät für Chemie und Biowissenschaften

des Karlsruher Instituts für Technologie (KIT)

genehmigte

DISSERTATION

von

M.Sc. Xiaohui Li

aus

Henan, V.R. China

KIT-Dekan: Prof. Dr. Manfred Wilhelm

Referent: Prof. Dr. Patrick Théato

Korreferent: Prof. Dr. Pavel Levkin

Tag der mündlichen Prüfung: 12.02.2021

Die vorliegende Arbeit wurde vom Oktober 2016 bis März 2021 unter Anleitung von Prof. Dr. Patrick Théato am Karlsruher Institut für Technologie (KIT) und der Universität Hamburg (UHH) im Rahmen einer gemeinschaftlichen Betreuung angefertigt.

Erklärung

Ich versichere hiermit, dass ich diese Arbeit selbständig angefertigt habe und keine anderen, als die angegebenen Quellen und Hinweise benutzt, sowie die wörtlich oder inhaltlich übernommenen Stellen als solche kenntlich gemacht und die Satzung des Karlsruher Instituts für Technologie (KIT) zur Sicherung guter wissenschaftlicher Praxis in der gültigen Fassung beachtet habe. Die elektronische Version der Arbeit stimmt mit der schriftlichen überein und die Abgabe und Archivierung der Primärdaten gemäß Abs. A (6) der Regeln zur Sicherung guter wissenschaftlicher Praxis der KIT beim Institut ist gesichert.

Ort, Datum, Unterschrift

Abstract

Dynamic polymer networks represent a broad class of polymer networks cross-linked with reversible bonds, involving dynamic non-covalent and covalent bonds, which can undergo reversible cleavage and recombination upon specific stimuli. Accordingly, dynamic polymer networks have gained enormous research interest in the recent years by their virtue of autonomous self-healable ability, good recyclability and facile implementation into broad range of applications ranging from dynamic and reprocessable coatings to sealants and elastomers. In this thesis, dynamic functional polymer networks were designed and investigated in-depth as both hydrogels and bulk polymer, with the particular emphasize on polymer networks that have been synthesized by employing dynamic covalent boronic ester bonds.

First, the synthesis of conductive hydrogel composites with autonomous self-healing ability was studied in Chapter 4. The initial trial with a non-covalently cross-linked network based on host-guest and electrostatic interactions manifested the successful preparation, nevertheless due the tedious synthesis protocols, a novel conductive and self-repaired hydrogel based on boronate ester bonds was subsequently developed. For this, a functional copolymer decorated with pyrene and phenylboronic acid moieties was synthesized, followed by reacting with SWCNTs and PVA to prepare the targeted hydrogel composites. Importantly, the interaction between pyrene moieties and SWCNTs in addition to the conductivity and self-recovery ability in electric conductivity were investigated in depth.

Subsequently, in Chapter 5, the design of a novel anti-fatigue and self-healable hydrogel was proposed via borax catalyzed thiol-ene click reaction and borax-diol chemistry. To achieve this, a functional copolymer bearing pendent acrylate and 1,2-diol groups was first synthesized, followed by reacting with thiol-functionalized PF127 under the catalyst, i.e. borax. Through this way, boronate ester bonds and PF127 micelles act as two distinguishable dynamic cross-linking mechanisms within one hydrogel system, and the as-fabricated hydrogels were further investigated by evaluating the mechanical properties and self-healing ability.

Ultimately, in Chapter 6, a dynamically cross-linked polymer network embedded with reversible boronic ester bonds was synthesized via *para*-fluoro-thiol click reaction (PFTR). A model reaction mimicking the final polymeric network was first investigated to gain insight into the role of utilized organic superbases and their respective effect on the regioselectivity of PFTR. Subsequently, an analogue polymeric network was

designed, which exhibited a reprocessability and self-healing ability due to the reversible and dynamic boronic ester cross-links. The thermodynamic behavior of the polymeric network, as well as its malleability and self-healing ability have been investigated in detail.

Zusammenfassung

Dynamische Polymernetzwerke stellen eine breite Klasse von Polymernetzwerken dar, die mit reversiblen Bindungen vernetzt sind und dynamische nichtkovalente und kovalente Bindungen umfassen. Bei bestimmten Stimuli können diese Bindungen eine reversible Spaltung und Rekombination durchlaufen. Dementsprechend haben dynamische Polymernetzwerke in den letzten Jahren aufgrund ihrer autonomen Selbstheilungsfähigkeit, guten Recyclingfähigkeit und einfachen Implementierung in ein breites Anwendungsspektrum, das von dynamischen und wiederaufbereitbaren Beschichtungen bis hin zu Dichtungsmassen und Elastomeren reicht, enormes Forschungsinteresse gewonnen. In dieser Arbeit wurden dynamische funktionelle Polymernetzwerke sowohl als Hydrogele als auch als Bulk-Polymer entworfen und eingehend untersucht, wobei der Schwerpunkt auf Polymernetzwerken lag, die unter Verwendung dynamischer kovalenter Boronsäureester-Bindungen synthetisiert wurden.

Zunächst wurde in Kapitel 4 die Synthese leitfähiger Hydrogel-Komposite mit autonomer Selbstheilungsfähigkeit untersucht. Der erste Versuch mit einem nicht kovalent vernetzten Netzwerk auf der Basis von Wirt-Gast- und elektrostatischen Wechselwirkungen zeigte die erfolgreiche Herstellung. Jedoch aufgrund der langwierigen Synthese wurde anschließend ein neues leitfähiges und selbstreparierendes Hydrogel auf Basis von Boronatester-Bindungen entwickelt. Zu diesem Zweck wurde ein mit Pyren- und Phenylboronsäureeinheiten dekoriertes funktionelles Copolymer synthetisiert und anschließend mit SWCNTs und PVA umgesetzt, um die angestrebten Hydrogel-Verbundstoffe herzustellen. Insbesondere die Wechselwirkung zwischen Pyreneinheiten und SWCNTs zusätzlich zur Leitfähigkeit und Selbstwiederherstellungsfähigkeit der elektrischen Leitfähigkeit eingehend untersucht.

Anschließend wurde in Kapitel 5 der Entwurf eines neuartigen Anti-Ermüdungs- und selbstheilenden Hydrogels über die Borax-katalysierte Thiol-En-Klick-Reaktion und die Borax-Diol-Chemie vorgestellt. Um dies zu erreichen, wurde zunächst ein funktionelles Copolymer mit anhängenden Acrylat- und 1,2-Diolgruppen synthetisiert, gefolgt von der Reaktion mit Thiol-funktionalisiertem PF127 mittels eines Katalysators, z. B. Borax. Auf diese Weise wirken Boronatester-Bindungen und PF127-Mizellen als zwei unterscheidbare dynamische Vernetzungsmechanismen innerhalb eines Hydrogelsystems. Die so hergestellten Hydrogele wurden weiter untersucht, indem die mechanischen Eigenschaften und die Selbstheilungsfähigkeit bewertet wurden.

Letztendlich wurde in Kapitel 6 ein dynamisch vernetztes Polymernetzwerk, eingebettet in reversible Boronsäureesterbindungen, über die *para*-Fluor-Thiol-Klick-Reaktion (PFTR) synthetisiert. Zunächst wurde eine Modellreaktion untersucht, dem endgültigen polymer entsprechende Modellreaktion untersucht, um den Einfluss der verwendeten organischen Superbasen und ihre jeweilige Wirkung auf die Regioselektivität von PFTR zu ermitteln. Anschließend wurde ein analoges polymeres Netzwerk entworfen, das aufgrund der reversiblen und dynamischen Boronsäureestervernetzung eine Wiederaufbereitbarkeit und Selbstheilungsfähigkeit aufwies. Das thermodynamische Verhalten des polymeren Netzwerks sowie seine Formbarkeit und Selbstheilungsfähigkeit wurden eingehend untersucht.

Content

1.   Introduction

Since Hermann Staudinger proposed the revolutionary macromolecular hypothesis in 1920,[1] the use of synthetic polymer materials has been rapidly rising, and now polymer materials have been playing a dominant role in almost every imaginable aspect of our daily life. Indeed, over the past century, mankind had witnessed an enormous growth of polymeric commodities while their excellent durability and chemical inertness, in turn, resulted in a serious environmental problem, particularly, in the forms of landfills and oceanic pollution.[2] Accordingly, designing polymers that can be self-repaired upon damage in a multiply fashion is an attractive and logical way to weaken their environmental impact by remarkably prolonging the respective service life.

In regard to self-healable polymers, a plethora of research has been reported by embedding diverse noncovalent and dynamic covalent bonds into the polymer systems.[3-5] The noncovalent bonds, such as host-guest interaction, electrostatic interaction, hydrogen bonding and hydrophobic interaction, feature inherent reversibility and have been intensively employed to design self-healable polymers.[6, 7] Additionally, dynamic covalent chemistry offers a variety of reversible covalent bonds, e.g. Diels-Alder reaction, disulfide bond, imine bond, acylhydrazone bond and boronic ester bond exchange reactions, which exhibit higher stability compared to the non-covalent bonds while affording continuous reversibility upon specific stimuli.[8, 9] Among the diverse possibilities associated with dynamic chemistry, this thesis mainly aims at designing dynamic functional polymer networks with self-healable character, with the emphasize on the organoboron species with dynamic covalent boronic ester bonds.

To achieve this, studies towards the implementations of both reversible non-covalent bonds (i.e. host-and-guest and electrostatic interactions) and covalent bonds (i.e. boronic ester bonds) to the design of dynamic hydrogel networks are first presented. Two distinct chapters of the presented thesis are devoted to these hydrogel systems. Prior to the fabrication of hydrogel networks, functional copolymers are synthesized by employing controlled living polymerization and facile post-polymerization modification. The resulting copolymers are characterized by standard techniques, such as ^{1}H and ^{19}F nuclear magnetic resonance spectroscopy, FT-IR spectroscopy and size-exclusion chromatography, and the corresponding hydrogels are further investigated in detail on their mechanical properties and autonomous self-healing abilities.

Last but not the least, bulk polymeric networks with dynamic nature are studied within the frame of this work. Particularly, *para*-fluoro-thiol click reaction (PFTR) is employed to construct a dynamically cross-linked network based on reversible boronic ester bonds. The thermodynamic behavior of the polymeric network, as well as its chemical resistance, malleability and self-healing ability are investigated in depth.

2.   Theoretical background and literature overview

2.1   Dynamic chemistry

Constitutional dynamic polymers, also termed as dynamers, represent a broad class of polymers linked through reversible connections and have therefore the capacity to modify their constitution by exchange and reshuffling of their components.[10] Dynamers can be classified into dynamic non-covalent and dynamic covalent polymers depending on whether the connections are non-covalent interactions or reversible covalent bonding. Constitutional dynamic polymers are typically featured with both "dynamic" and "reversible" characters, which impart the dynamers with distinctively adaptable, exchangeable and self-healable properties under the effect of external chemical or physical triggers, thus making them outstandingly attractive materials in terms of their widespread applications in polymeric fields.[11, 12]

2.1.1   Supramolecular chemistry

Supramolecular polymers, or dynamic non-covalent polymers, are constructed by a series of directional and reversible secondary interactions implemented in supramolecular chemistry, including hydrogen bonding, electrostatic, donor-acceptor, Van der Waals and metal ion coordination.[13] Nature always inspires scientists with various supramolecular polymer examples , e.g. proteins, enzymes as well as the our fundamental DNA that is held together by π-π stacking and hydrogen bonding.[14] Recognition of supramolecular chemistry was first achieved when Lehn, Pedersen and Gram were awarded the 1987 Noble Prize in chemistry for their development and use of molecules with structure-specific interactions of high selectivity.[15] Thus, over subsequent decades, supramolecular chemistry have provided the frameworks for the design of supramolecular polymers with tunable and interactive properties,[16] which have been widely employed in sensors,[10] biological and cell imaging,[17] drug delivery[18] as well as self-healing systems.[19]

2.1.2   Dynamic covalent chemistry

Dynamic covalent chemistry involves chemical reactions that proceed reversibly under equilibrium-controlled conditions. Essentially, dynamic covalent chemistry are thermodynamic controlled reactions, where the relative stability (ΔG^0) of products determines the proportions of final products, rather than the relative energies (ΔE_a) as in kinetically controlled chemistry.[20, 21] As schematically illustrated in **Scheme**

2.1, although the relative magnitudes ($\Delta G_B^{\ddagger}$ versus $\Delta G_c^{\ddagger}$) of the transition states to B is higher than C. A goes to B rather than C due to the relatively better stabilities of the resulting product B compared to C. The reversible nature of dynamic covalent materials originates from a series of dynamic covalent bonds, which are capable of undergoing dissociation / association procedures to achieve the most thermodynamically stable products distributions upon external stimuli.[21]
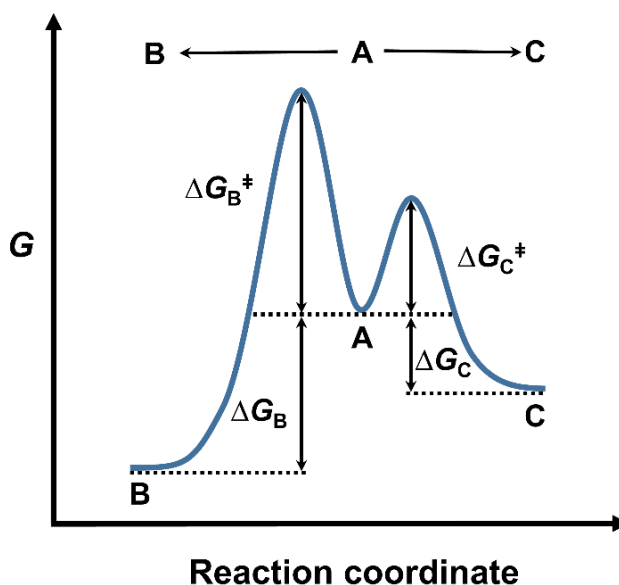
Scheme 2.1. Free energy profile illustrating the kinetically (A→C) versus thermodynamic (A→B) controlled reaction.

Thus far, diverse of dynamic covalent bonds have been intensively explored, including dynamic C-C, C-O, C-N, C-S, S-S, B-O as summarized in **Scheme 2.2 and 2.3**. A classic dynamic C-C bond formation is the Diels-Alder (DA) reaction between for example an electro-rich furan and an electro-poor maleimide, and corresponding reversible exchange reactions could be triggered at relative high temperature (normally above 75 °C).[22, 23] Besides, transition-metal-catalyzed olefin metathesis is another powerful synthetic methodology related to dynamic C-C bonds, featuring high efficiency under ambient conditions.[24] The crucial components in dynamic C-N bonds are imine bonds that are generated by the condensation reaction of aldehydes and amines. Exchanges take place among dynamic imine bonds through imine formation and transamination.[25] In biological fields, dynamic C-N bonds in oximes and hydrazones have garnered increasing research interest due to their well-suited compatibility.[26, 27] However, compared to imine bonds, oximes and hydrazones are normally more stable, hence the dynamic bond rearrangements within oximes and hydrazones systems usually occur in the presence of efficient catalyst.[28, 29] Furthermore, urea bonds formed

through reactions of isocyanates and amines are the latest studies in dynamic C-N bonds, and have shown great value in industrial poly(urea-urethane) thermosets fields.[30, 31]
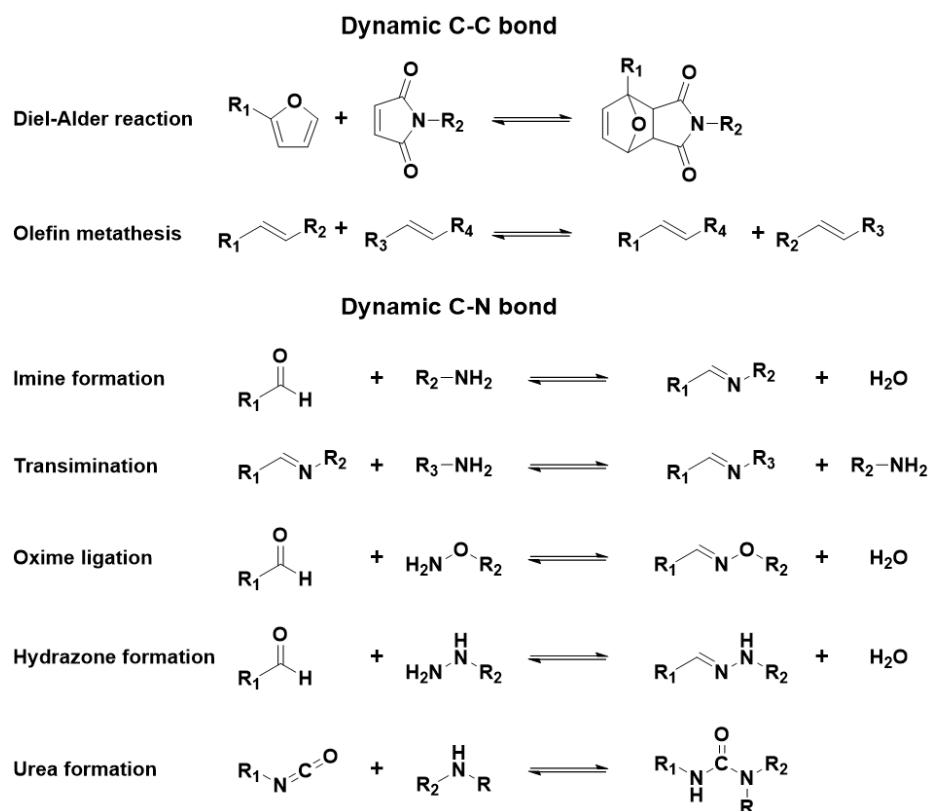
Scheme 2.2. The represented dynamic C-C and C-N bonds, and their corresponding dynamic chemistry.

As for dynamic C-O bonds, ester formation and exchange are the typical reactions that been extensively employed for organic synthesis and dynamic covalent network.[32, 33] Sulfur-containing dynamic bonds involve reversible C-S and S-S bonds, as featured with thioacetal exchange and disulfide exchange reactions.[34, 35] In general, dynamic B-O bonds are represented by boronic acid condensation reactions, where boronic acids could either reversibly complex with *cis-* 1,2 or 1,3 diols to form dynamic boronic ester bonds,[36, 37] or directly yield cyclic oligomers called boroxines through dehydration.[38, 39]

When integrated as crosslinks in polymer networks as dynamic covalent linkages, these exchangeable covalent bonds facilitate the construction of polymer networks with unique adaptive properties, thus linking the macroscopic rheological and mechanical properties of the polymer networks to the controllable reaction kinetics of the dynamic covalent chemistry.[40, 41]

Dynamic C-O bond

Eester formation

Ester exchange

Dynamic C-S bond

Acetal exchange

Dynamic S-S bond

Disulfide exchange

Dynamic B-O bond

Boronic acid
condensation
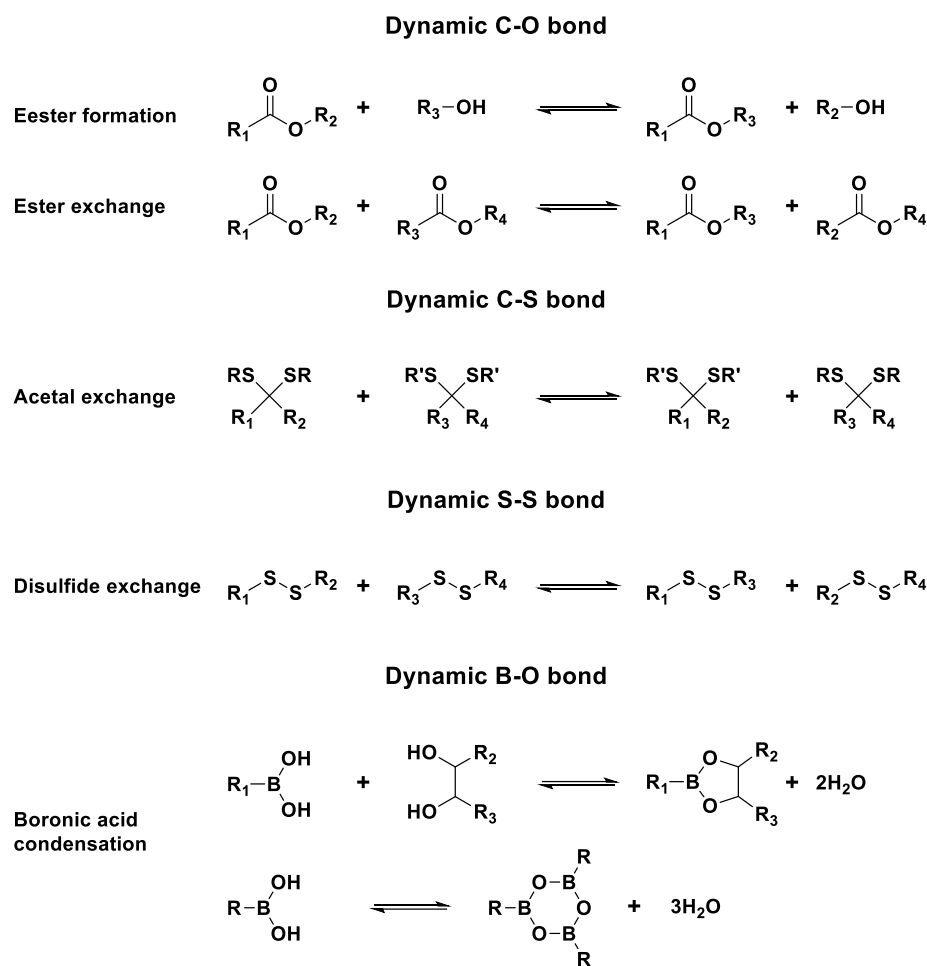
Scheme 2.3. The represented dynamic C-O, C-S, S-S and B-O bonds, as well as their corresponding dynamic chemistry.

The thermodynamic equilibrium constants K, which is equal to the rate constant for the bond-forming reaction divided by the rate constant for the bond-breaking, can dictate the equilibrium between the bound and unbound forms and therefore the connectivity of the system.[42] Generally, the exchange of these dynamic covalent bonds within the cross-linked polymer networks can proceed through two pathways: dissociative and associative process.[43] For the dissociative one, the cleavage and reformation of the bonding happen independently, leading to the decrease of K and thus the detention of the crosslink density after processing (**Figure 2.1 (A)**); while associative process is able to retain the crosslink density ($K = 1$) during the exchange process due to the bond-breaking and bond-forming occur in a single substitution reaction with the equal exchange reaction rates (**Figure 2.1 (B)**)[44]. Leibler initially coined the term "vitrimers" for the associative species due to their similar viscosity-temperature relationship to that of vitreous silica.[45] Dissociated exchange chemistries are represented by Diels-Alder reactions,[22, 46] alkoxyamines,[47, 48] urethane dissociations,[30] disulfides[49] and thiol-Michael addition,[50] while the associative processes are exemplified by

5

transesterifications,[51, 52] boronic ester,[53-55] olefin metathesis,[24, 56] transamination of vinylogous urethanes[57, 58] as well as thiol-thioester reactions.[59]
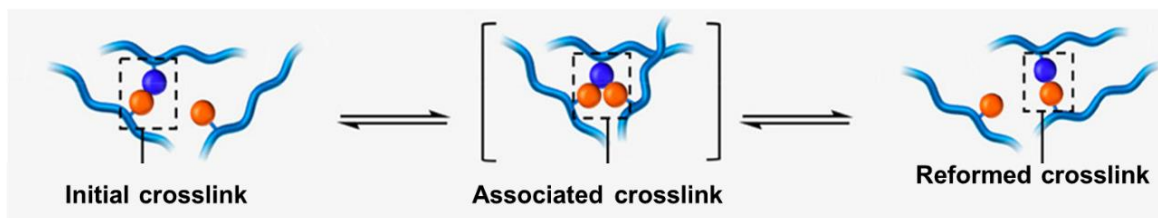
Figure 2.1. The general mechanism of dissociative (A) and associative (B) bond exchange pathways. Reprinted with permission from Ref. [44], copyright (2019) American Chemical Society.

Dynamic covalent bonds are capable of reversibly breaking and reforming in response to external stimuli such as light, temperature and pH, and when incorporated into polymer networks, they can endow the as-fabricated polymer networks with unprecedented properties, such as self-healing, malleability, shape-memory, adaptability and responsiveness, among which, self-healing ability and malleability have been the primary motivations for exploiting dynamic covalent polymer networks.[42, 60]

2.2 Self-healing polymers

Self-healing polymers are defined as a typical class of materials that exhibit the capability of recovering their physical damages thus obtaining enhanced lifespan and reliability.[61-63] In fact, self-healing polymers have received intensive attentions due to their potential in mimicking biological organisms that exhibit built-in self-repaired nature. Prior to the wide-discovered self-healing methodologies, polymers equipped with self-healing abilities were normally approached by the so called encapsulation method, wherein the

monomer and catalyst are dispersed within capsules imbed into a polymer matrix.[5, 64, 65] Upon damage, the ruptured nano- or microcapsules at the damage site will release the reactive components inside, driving the self-repairing process to proceed under certain chemical reactions. (**Figure 2.2 (A)**) The main drawback of this method lies in the fact that the self-healing process only occurs once, and repeated self-repairing behavior fails to happen due to the lack of monomer. A second developed vascular-based methodology somehow solved this problem, in which reactive chemicals are filled into hollow fibers constructed with cardiovascular architectures, as shown in **Figure 2.2 (B)**.[66-68] The abundance of reagents allows for multi-times self-healing reactions at the same damaged site. Since these two methods totally rely on external chemical reagents to accomplish the self-healing process, capsule- and vascular-based polymers are categorized as extrinsic self-healing polymers.[3]

(A) Encapsulation

(B) Cardiovascular network
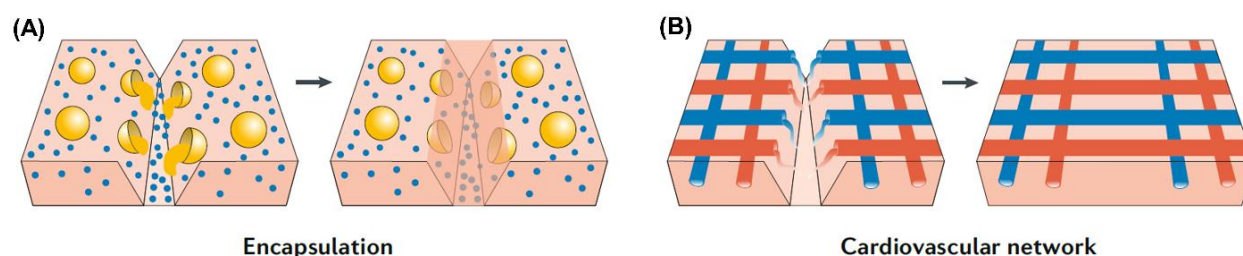
Figure 2.2. Self-healing mechanisms of extrinsic self-healing polymers, including capsule-based (A) and vascular-based (B) polymers. Reprinted by permission from Ref.[61], copyright (2020) Springer Nature.

Intrinsic self-healing polymers are the latest developed generation and they are based on internal molecular interactions. Generally, polymers could also be endowed with intrinsic self-healing character through the incorporation of a series of reversible bonds, including dynamic covalent as well as supramolecular bonds. The transient nature of these reversible bonds drives their cleavages and reformations to happen spontaneously or under some stimuli (i.e. heat, pH or light) at the damage site, thus intrinsically repairing the structural cracks multi-times.[61, 69]

Supramolecular chemistry is featured with reversibility, directionality and sensitivity, thus making itself particularly attractive when it comes to self-healing polymers. Compared to covalent bonding, supramolecular cross-linking is relatively weak and easily to be broken, therefore, supramolecular networks could be remodeled rapidly and reversibly from fluid-like, low density, high free volume states to solid-like, lower free volume, and elastic states.[3, 7] Self-healing polymers cross-linked by supramolecular bonds are

usually soft materials, and have been widely explored for injectable and printable hydrogels,[70-72] as well as artificial e-skins.[73-75]

Supramolecular bonds, as previously mentioned, are essentially a group of noncovalent and physical bonding, represented by hydrophobic interaction, electrostatic interaction, host-guest interaction, metal-ligand coordination as well as hydrogen bonding, as illustrated in **Figure 2.3.** Self-healing polymers based on hydrophobic interaction can be achieved via so called "micellar polymerization", wherein a hydrophobic monomer was first solubilized within sulfate micelles and then directly copolymerized with another hydrophilic monomer in surfactant aqueous emulsion. Reversible physical cross-links were formed through dynamic hydrophobic associations between the surfactant micelles and hydrophobic segments of the polymer chains.[76, 77] Oppositely charged ions can deliver electrostatic interaction when combined with each other, which can be used for preparing though polyampholyte hydrogels with a fast self-healing property.[78, 79] Host-guest interaction is generally achieved by selective molecular recognition between a "host" moiety (e.g. cyclodextrin) and a "guest" moiety (e.g. adamantane, azobenzene, ferrocene), wherein the hydrophobic interior cavity of the host molecules can accommodate the hydrophobic guest molecules with high selectivity.[80-82] Coordinating bonds are usually formed by metal-ligand complexations whose strength varies between different metal ions and their chelating ligands, which could be employed to design self-healing polymers with matched mechanical strength for practical applications.[83, 84] Hydrogen bonding normally exists between hydrogen atoms (H) and highly electronegative nitrogen (N) and oxygen atoms (O). For instance, 2-ureido-4-pyrimidone (UPy) is able to generate self-complementary quadruple hydrogel bonding through intermolecular N⋯H and O⋯H interactions, and has been customarily decorated on the polymer side chains to construct self-healing hydrogels and malleable thermosets.[70, 85]

Dynamic covalent bonds, as mentioned above, are based on dynamic covalent chemistry, and predominately utilized to synthesize self-healing polymers with mechanical toughness due to their high bonding strength, among which, Diels-Alder (DA) reactions, disulfide bonds, oxime bod, imine bonds, acylhydrazone and boronic ester bonds (**Figure 2.3**) have been intensively explored to deliver covalent self-healing systems. Diels-Alder (DA) reactions are thermo-reversible and self-healing only occurs by heating the damage sites to elevated temperatures (normally above 75 °C).[86-88] The dynamic nature of disulfide bonds is based on reversible exchange reaction between thiol and disulfide, which is pH- and redox- sensitive.[89-91] Imine bonds, also named as Schiff base, are easily formed through the reactions between amine and aldehyde groups which are reversible under neutral conditions. Since imine bonds are sensitive to pH, temperature and

enzymes, they are largely employed to fabricate self-healing hydrogels with multiple responsiveness for biomedical applications.[92-94] Acylhydrazone bonds belongs to the class of imine bonds, and are generated from the reactions between aldehydes and acylhydrazides with improved hydrolytic stability, and have been widely incorporated with other dynamic bonds in one cross-linked system to accomplish multifunctional hydrogels.[93, 95, 96] Dynamic boronic ester bonds are formed through complexation between boronic acids and diol groups, and their dissociation and association process could automatously take place in both aqueous and organic solvent media, therefore they are commonly used to fabricate polymers with self-healing property at ambient conditions.[39, 97] Since the work in this thesis is mainly targeting at dynamic cross-linked systems based on reversible boronic ester bonds, they will be introduced specifically in the following section.
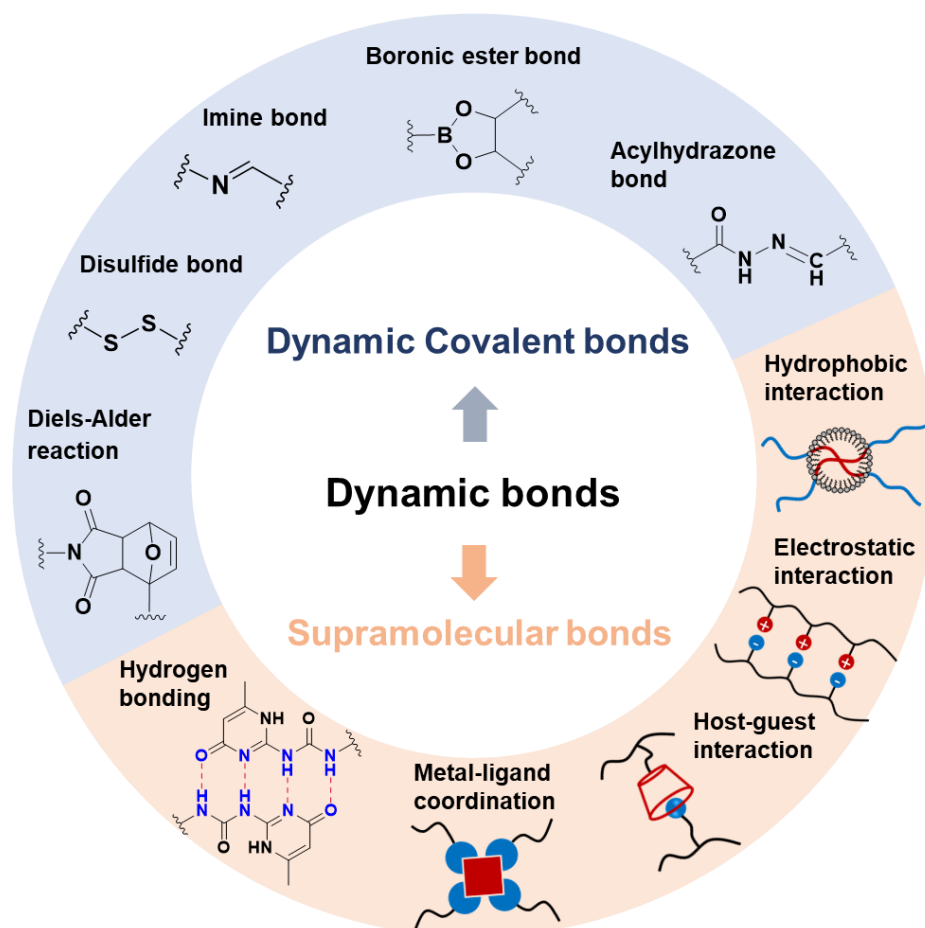
Figure 2.3. The represented dynamic bonds used to fabricate intrinsically self-healing polymers, including dynamic covalent bonds and supramolecular bonds.

2.3 Boronic acid chemistry

Structurally, boronic acids are trivalent boron-containing organic compounds that consist of one alkyl substituent and two hydroxyl groups on the boron atom. Boron exhibits six covalent electrons, i.e. it is deficient in two electrons, and hence the boron atom is sp^2 hybridized with a vacant p-orbital and adopts as planar trigonal configuration.[98] Boronic acids can't be found in nature and are usually synthesized through sequential oxidation of boranes. The first oxidation step results in a borinic acid product, which is more stable than a borane but can be transformed to a boronic acid via the second oxidation process. The further oxidation of boronic acids yields boric acids, which are known as environmentally friendly compounds with relatively low-toxicity, thus broadly utilized in household products.[99] Boronic acids usually exist as oligomeric anhydrides in their solid state, particularly as trimeric anhydride boroxine. Boronic esters are obtained by substitution of the hydroxyl groups with alkoxy or aryloxy groups, as shown in **Scheme 2.4.**
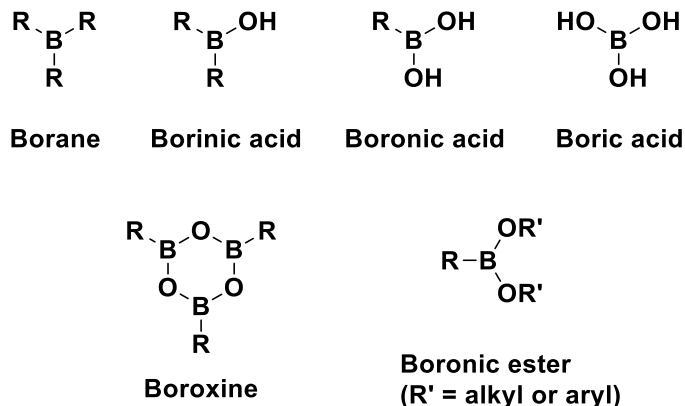
Scheme 2.4. The structures of various organoboron compounds.

Boronic acids act primarily as mild Lewis acids due to the vacant p-orbital on the boron atom, and their stability and facile handling make them a promising class of synthetic intermediates, especially in Suzuki-Miyaura cross-coupling reactions.[100] Boronic acids can also act as catalysts for activating hydroxyl-containing reagents such as carboxylic acids and alcohols in a mild and selective manner.[101] Besides, the reversible complexes between boronic acids and Lewis bases or diols have versatile applications in analytical and biological chemistry, such as saccharides and glucose detecting systems, antimicrobial agents and enzyme inhibitors, as well as the labelling of proteins and cell surface.[102-105]

2.4 Boronic esters as dynamic covalent cross-links

Boronic esters are generally formed through the condensation reactions between boronic acids and *cis*- 1,2 or 1,3 diols, which could be accomplished in both aqueous media and anhydrous organic solvents at ambient temperature in the absence of a catalyst, as shown in **Scheme 2.5**.[98] Essentially, the reversible association / disassociation rearrangements of boronic ester bonds are in chemical equilibrium, which depends heavily on external environment (such as pH and temperature). When incorporated into polymer networks, boronic ester moieties are capable of serving as the dynamic covalent linkages. By spontaneously breaking and reforming the dynamic bond adapts to external stimuli (such as pH, temperature and mechanical loading), polymer networks are endowed with distinctive stimuli-responsive, malleable and self-healing properties.[36, 39, 41] Therefore, boronic esters as cross-linking motif have been widely utilized in the design of dynamic covalent polymer networks, both in hydrogel systems and bulk network polymers.[40, 106]
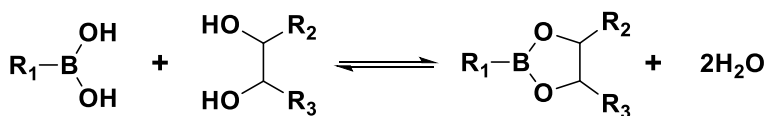
Scheme 2.5. The formation of boronic esters by the condensation reactions

2.4.1 Dynamic boronic ester bonds in aqueous solutions

The reversible complexations between boronic acids and polyols in aqueous media was first recognized by the seminal work of Lorand and Edwards in 1958.[107] In aqueous solution, a series of thermodynamic equilibriums exist between the neutral and anionic forms of boronic acids with *cis*- 1,2 or 1,3 diols. As illustrated in **Scheme 2.6**, neutral boronic acids are organic Lewis acids with trigonal planar configurations, which act as electron-accepting species due to the vacant p-orbital on the center of sp^2-hybridized boron atoms. Under basic conditions, the electron-deficient boron atoms tend to be attacked by Lewis base hydroxide anions, thus generating the tetrahedral boronate anions with sp^3-hybridrized boron atoms. While under acidic conditions, the equilibrium will shift to the side of neutral boronic acids. As for further esterification reactions, diols groups can complex with both of neutral boronic acids and boronate anions, thus producing corresponding boronic esters and boronate esters, respectively. Since boronate esters with

tetrahedral structures are more hydrolytically stable than trigonal planar boronic esters, the equilibrium tends to shift from neutral boronic esters to anionic boronate esters ($K_{tet} > K_{trig}$).[36, 108, 109]
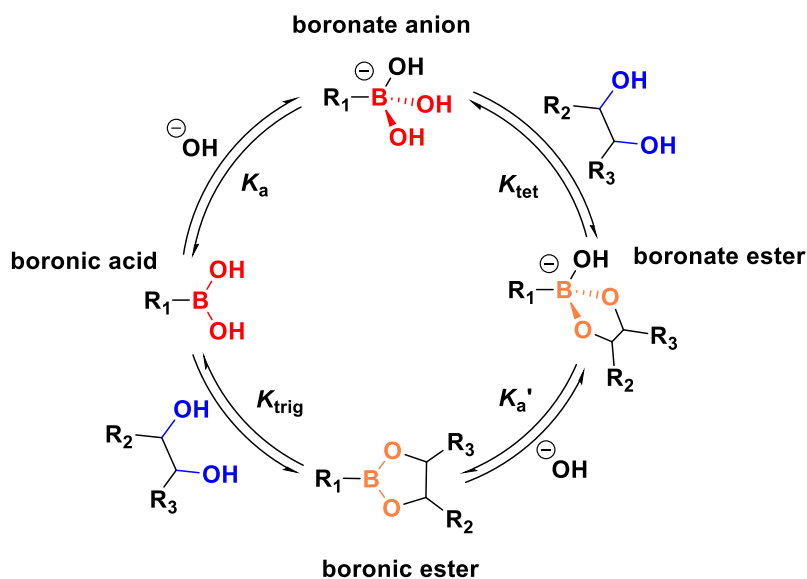
Scheme 2.6. Thermodynamic equilibriums of boronic esters with *cis-* 1,2 or 1,3 diols in aqueous solution, wherein, K_a and K_a' are the ionization constants of boronic acid and boronic ester, respectively; K_{trig} and K_{tet} are the equilibrium constants for the pathways between the trigonal neutral and tetrahedral anionic forms, respectively.

Generally, the stability of boronate esters is affected by pH, and the formation of boronate esters are more favored when the solution pH is larger than the pK_a of the boronic acid, where pK_a is defined as the pH value at which half of neutral species transform to their anionic forms. However, most of boronic acids exhibit higher pK_a values than physiological conditions (pH ~ 7.4), leading to their limited applications in biological fields. Recently, some guidelines were proposed to modify the boronic acids to reach to a lower pK_a. Generally, phenylboronic acids exhibit a lower pK_a value than alkylboronic acids, and the introduction of electron-withdrawing groups on the phenyl rings can further lower the pK_a value through inductive effects. [36, 99, 110] For example, the pK_a of phenylboronic acids (pK_a = 8.8) is much lower than that of methylboronic acids (pK_a = 10.4), while it is relatively higher than that of 4-(methylcarbamoyl) phenylboronic acid (pK_a = 7.8) due to the electron-withdrawing effect on the substituent. Wulff-type boronic acids with a nitrogen center adjacent to the boron atom, such as 2-dimethylaminomethyl phenylboronic acid results in relatively

lower pK_a ~ 5.2 due to the formation of an intermolecular B-N dative bond, which allows for the formation of stable boronate esters with a sp^3 hybridization.[111] Additionally, 2-hydroxymethylphenyl boronic acid (also known as benzobroxole or benzoxaborole) also exhibits relatively low pK_a ~ 7.2 due to the release of ring strain during the transition from sp^2 to sp^3-hybridrized forms, which has been widely explored to form biological hydrogels at physiological pH.[112-114] The structures of various boronic acids, as well as their corresponding pK_a values, are listed in **Table 2.1.**

Table 2.1. The structures of commonly used boronic acids, as well as their corresponding ionization equilibriums in aqueous solution and pK_a values.[36]

Name	Structure	Ionization equilibrium	pK_a
Boronic acid			9.2
Methylboronic acid			10.4
Phenylboronic acid			8.8
4-(Methylcarbamoyl) Phenylboronic acid			7.9
2-Dimethylaminomethyl phenylboronic acid			5.2
2-Hydroxymethylphenyl boronic acid			7.2

13

Theoretically, small molecules and polymers containing *cis-* 1,2 or 1,3 diols can complex with boronic acids in aqueous solution, however, their binding affinities should be taken into considerations when designing cross-linked hydrogel networks. Taking phenylboronic acid (PBA) as an example, researchers have found that catechol and Alizarin Red S (ARS) (**Scheme 2.7**), both featuring coplanar vicinal *cis*-diols, present the highest binding affinities with PBA compared to other diols-containing groups..[107, 110] Indeed, dopamine-based polymers with pendent catechol groups were intensively explored to fabricate self-healable and tissue-adhesive hydrogels by complexing with functional polymers decorated with pedant PBA.[115, 116] While, ARS has been widely applied as a general fluorescent indicator for determining the binding constants between a variety of *cis*-diols and boronic acids.[110, 117]

Additionally, fructose exhibits a much higher binding constant with PBA compared to other monosaccharides,[118] therefore, it was commonly utilized to construct bio-based hydrogels combing with PBA-grafted hyaluronic acid.[119] Recent studies by Auzély-Velty and coworkers revealed that the choice of boronic acid / saccharide pairs has a great effect on the viscoelastic properties of the boronate ester cross-linked hyaluronic acid (HA) hydrogels, and strong hydrogel networks with slow relaxation times and relatively high dynamic moduli were achieved at physiological pH between 3-aminophenyboronic acid (3-AMPBA) / fructose pairs grafted on HA due to their outstanding binding affinity.[120]

Besides, poly (vinyl alcohol) (PVA) is also a good binding candidate for PBA due to its rich-diol groups along the polymer chain, as well as excellent biocompatibility.[97] PBA-decorated polymers have been widely used to cross-link with PVA to form multi-functional hydrogels from acidic to basic aqueous conditions.[121, 122]
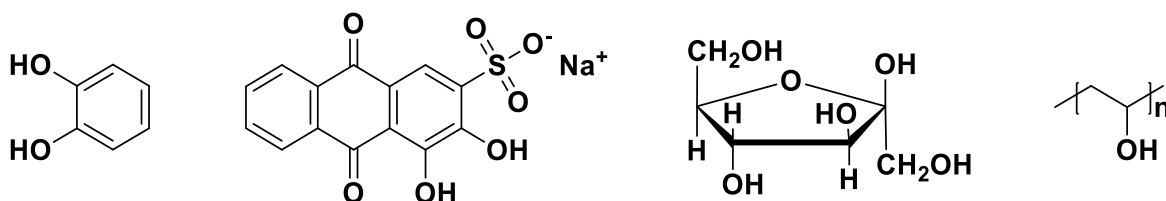
Scheme 2.7. Diol-containing functional groups or polymers which exhibit good binding affinity with phenylboronic acids (PBA), from left to right, catechol, Alizarin Red S. (ARS), fructose and poly (vinyl alcohol) (PVA), respectively.

2.4.2 Dynamic boronic ester bonds in bulk network polymers

Except for aqueous solution based cross-linking systems, boronic esters with trigonal planar structures could also be formed in bulk network polymers or in anhydrous organic solvents, and their thermodynamic behavior between association and dissociation can be accessed through different pathways, which include direct metathesis of dioxaborolane and reversible transesterification, as illustrated in **Scheme 2.8.** Dioxaborolane metathesis reaction relies on reversible exchange of network fragments linked by dynamic boronic esters, and this reaction was proven to spontaneously take place at moderate temperature in the absence of impurities without a catalyst.[53, 123, 124] In the transesterification process, boronic esters could either react with *cis*-diols arising from boronic ester hydrolysis, or externally added moieties containing *cis*-diol groups.[39, 125]
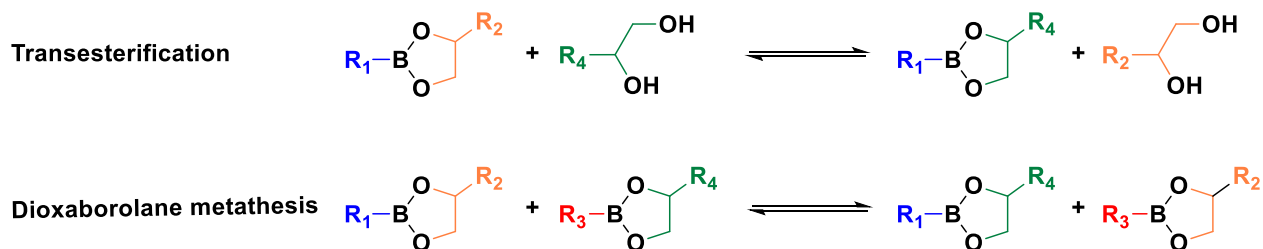
Scheme 2.8. Thermodynamic equilibriums of boronic ester bonds in bulk polymers, including transesterification and dioxaborolane metathesis process, respectively.

Generally, boronic ester bonds can be integrated in networks through multiple approaches: (1) by directly crosslinking boronic ester molecules with other small molecules via photo-initiated thiol-ene click reactions;[126, 127] (2) by crosslinking functional copolymers bearing boronic ester bonds or diol groups with bis-dioxaborolane;[53, 128, 129] or (3) by crosslinking polymers drafted with double bonds with thiol-modified boronic ester molecules via hot-press treatments.[112] So far, boronic ester bonds have been broadly incorporated in cross-linked networks in order to design healable, malleable and reprocessable bulk polymer networks, especially for so called covalent adaptable networks (CANs) or vitrimers.[39, 54, 130]

15

2.5 Applications of polymer networks with dynamic boronic esters

2.5.1 Self-healable hydrogels with multi-functional properties

As discussed before, the transient complexations between boronic acids and *cis*-diols could undergo fracture and regeneration process upon damage, thus endowing the hydrogels with intrinsically self-healing properties without any external stimuli under ambient atmosphere. Besides, the association and disassociation process is essentially a chemical equilibrium, which could be modulated by solution pH, temperature, solution composition and external diol's competition, thus imparting the as-fabricated hydrogels with multi-responsive behavior.[106] Therefore, boronic ester bonds are commonly incorporated into cross-linked polymer networks to accomplish self-healing hydrogels with a plethora of functionalities.[99, 131, 132]

Due to the inherent dynamic nature, boronate ester bonds have been widely explored to prepare pH- and saccharide-responsive hydrogels with an intrinsic self-repair ability. Yangjun et al.[133] reported a self-healable and pH / sugar dual-responsive hydrogel based on dynamic boronate ester bonding. As shown in **Figure 2.4 (A)**, by mixing zwitterionic polymers with dynamic benzoxaborole-catechol complexation in PBS solution, cross-linked hydrogels can be obtained at physiological pH due to the relatively low pK_a = 7.2 value of benzoxaborole. The as-fabricated hydrogel exhibited pH / sugar dual-responsive due to the dynamic nature of boronate ester bonds. As shown in **Figure 2.4 (B)**, the hydrogel network could undergo gel-sol-gel transformation upon consecutive addition of 0.1 M HCl and 0.1 M NaOH inducing the dissociation/recombination of boronate ester bonds under acidic and neutral conditions. Besides, the hydrogels can also be decomposed in fructose solution within 24 h. Since benzoxaborole / fructose exhibited much stronger bonding affinity compared to benzoxaborole / catechol, alternative benzoxaborole-fructose complexations induce the fracture of cross-links and finally result in a network decomposition. Additionally, the pH / sugar dual-responsive behavior of boronate ester bonds can also endow the as-fabricated hydrogels with shape memory properties. Chen and co-workers proposed a pH- and sugar-induced shape memory hydrogels by cross-linking sodium alginate modified with 3-aminophenylboronic acid and PVA, followed by being immersed into calcium chloride solution. The hydrogel could be temporary deformed at pH = 6.0 attributed to the unstable boronate ester bonds at low pH, and fix its temporary shape at pH = 10.6; while shape recovery could occur by soaking either in a monosaccharide solution or in a reduced pH solution (i.e. pH = 6.0).[134]
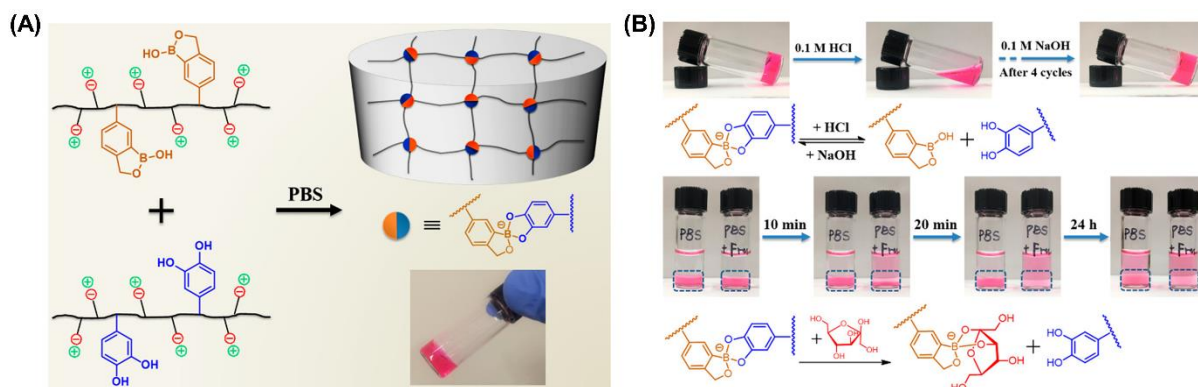
Figure 2.4. (A) Illustration of the fabrication of self-healable and pH / sugar dual-responsive hydrogels; (B) Photographs showing the pH and sugar dual-responsive behaviors of the hydrogels. Reprinted with permission from Ref.[133], copyright (2018) American Chemical Society.

Furthermore, the mechanical properties of the hydrogels based on boronate esters could be tuned by the choice of boronic acid / diol couples.[120] Therefore, injectable hydrogels with autonomous self-healing ability and stimuli-responsive properties could be attained when the boronic acid / diol couples were deliberately chosen, which in turn have also gained enormous research interest in clinical fields, especially alginate, poly(ethylene glycol) (PEG) and hyaluronic acid (HA) based biomaterials.[106] Meng et al. prepared an injectable PEG hydrogel by simply mixing dopamine functionalized 4-armed PEG and phenylboronic acid modified 4-armed PEG, wherein the corresponding reversible phenylboronic acid / catechol complexation endowed the hydrogel with pH, glucose and dopamine responsive properties, in addition to an instinctive self-healing ability.[115] Tamiris et al. proposed an injectable self-healing hydrogel based on dynamic boronate ester bonding, which was formed between benzoxaborin modified hyaluronic acid and saccharides decorated hyaluronic acid at physiological pH. Dynamic strain sweep rheology demonstrated its self-healing property and the as-fabricated hydrogel could be injected through a 1 mL plastic syringe with a 27 G needle at a flow rate of 1 mm/min, corresponding to the required injection force of only around 10 N.[135]

Except for stimuli-responsive properties, self-healable hydrogels with intrinsic conductivity have also received considerable research interest due to their promising application potential in bio-electronic and artificial e-skins. Indeed, by integrating with conductive fillers, borax / poly (vinyl alcohol) (PVA) gelation systems have provided a facile and straightforward way to obtain healable and conductive hydrogels.[136-139] Commercially available borax ($Na_2B_4O_7 \cdot 10H_2O$) could spontaneously dissociate into boric acid $B(OH)_3$ and

monoborate anion B(OH$_4^-$) at low concentration in aqueous solution. PVA was able to complex with B(OH$_4^-$) with 1:1 and 2:1 stoichiometry, and the corresponding 2:1 complexation facilitated the formation of hydrogel networks.[140] For example, Meihong et al. proposed a mussel-inspired conductive and healable hybrid hydrogel network. As illustrated in **Figure 2.5 (A)**, hybrid hydrogel could be easily obtained by simply mixing conductive functionalized single wall carbon nanotubes (FSWCNTs), polydopamine (PDA), PVA and sodium borate together. Among the cross-linked system, dynamic boronate ester bonds formed from the complexation between PVA and tetragonal borate anions, thus endowed the presenting hydrogel with a self-healing ability, while FSWCTs facilitated the construction of a conductive network at the same time. The hydrogel was connected to a circuit with a LED indicator, and its self-healing ability was proven by the transform from light-off state to light-on state during cut-and-healed tests, and the corresponding electrical signals demonstrated that the as-fabricated hybrid hydrogel exhibited high electrical self-healing efficiency of 99% within 2s.[139] Except for PVA / borax systems, functional polymers decorated with boronic acids derivatives have been also commonly used to combine with PVA for constructing ionic or electrical conductive and self-healable hydrogels.[141, 142]
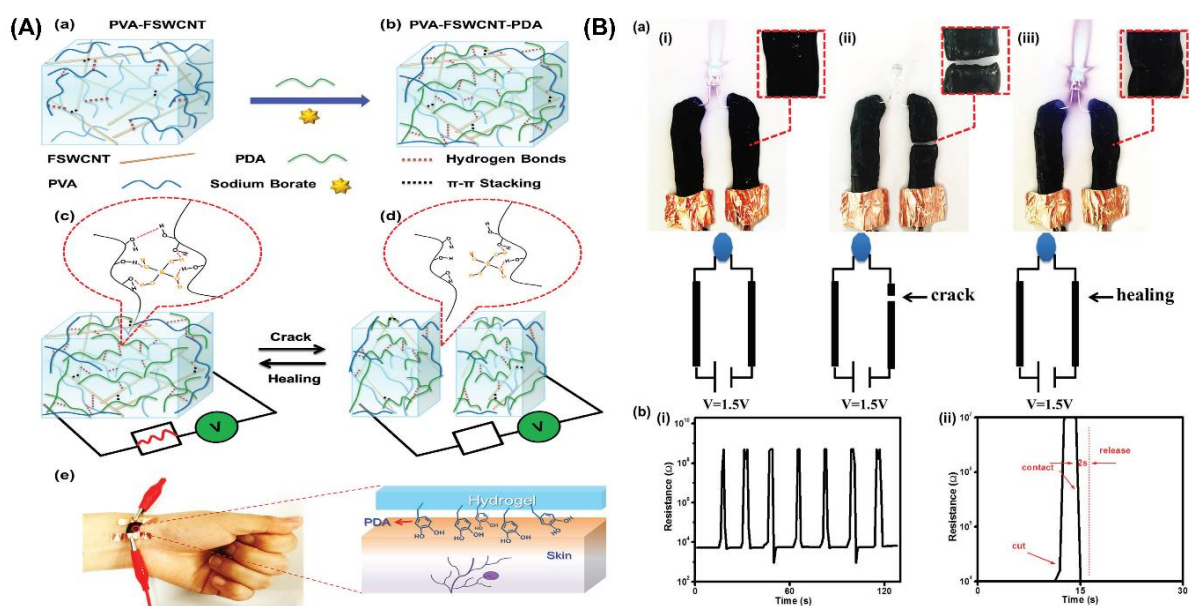
Figure 2.5. (A) Schematic illustration of the fabrication of the conductive and self-healable hybrid hydrogel. (B) Photographs showing the self-healing behavior of the hydrogel and corresponding electrical signals during serials of cut-and-healed process. Reprinted with permission from Ref.[139], copyright (2017) John Wiley and Sons.

2.5.2   Bulk network polymers with healable and reprocessable properties

Bulk polymer networks have been widely utilized in our daily life, especially for thermosets. In principle, conventional thermosets crosslinked with covalent bonds feature a thermal stability, chemical resistance and high mechanical strength, but are usually lacking of a malleability and recyclability because they can't be melt and flow at high temperature as thermoplastics. Recently, this problem was addressed by introducing dynamic covalent bonds into the polymer networks, which were defined as covalent adaptable networks (CANs).[143, 144] Boronic ester bonds, as one of the most intensively explored dynamic covalent bonds, have gained considerate interest for the design of self-healable and malleable thermosets.[39, 53, 126, 128]

Sumerlin and coworkers were among the first one who proposed a 3D bulk polymer network covalently crosslinked by dynamic boronic ester bonds via photoinitiated thiol-ene reaction,[126] as illustrated in **Figure 2.6 (A)**. The boronic ester bonds existed in thermodynamic equilibrium between the decomposition (to boronic acids and diol moieties) and recombination, which could be altered and shifted to the decomposition upon exposure to water Therefore, the resulting materials were able to be self-repaired at ambient temperature via sequential surface hydrolysis and re-esterification process, which was further qualitatively proven by cut-and-contact tests on disk-shaped samples, and in that case, the damage sites were found to disappear almost within 4 days, as shown in **Figure 2.6 (B)**.
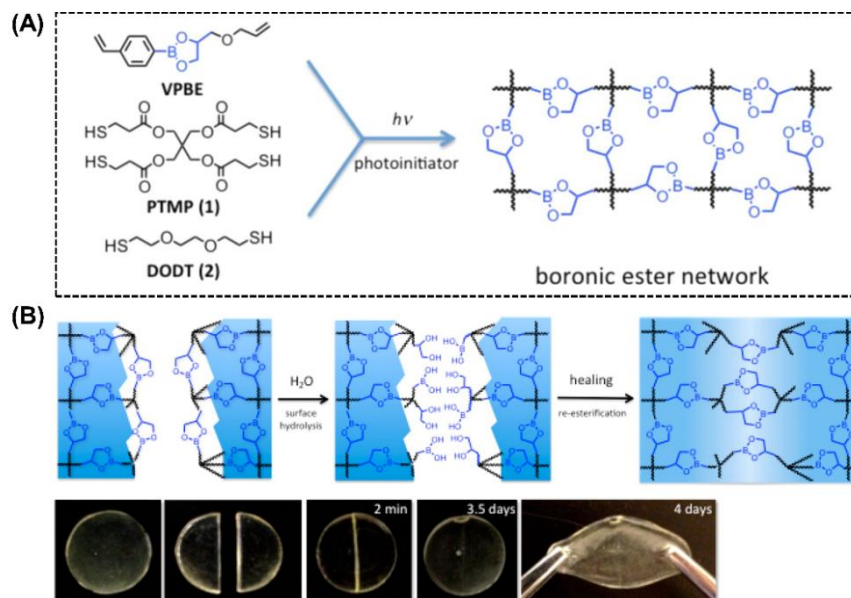
Figure 2.6. (A) Schematic illustration of the synthesis of the boronic ester network via photoinitiated thiol-ene reaction. (B) Photographs showing the self-healing mechanism and behavior of polymeric network. Reprinted with permission from Ref.[126], copyright (2015) American Chemical Society.

Leibler and coworkers reported in a pioneering study on the direct metathesis of boronic esters, wherein two different dioxaborolanes could directly undergo an exchange of fragments in the absence of solvent and catalyst, thus forming two new boronic esters without the detection of water or diols (**Figure 2.7 (A)**).[53] First, functional copolymers containing pendent boronic esters were synthesized via radical copolymerization of vinyl monomer bearing dioxaborolane units and styrene or MMA, or by reactive mixing for grafting dioxaborolanes onto commercial thermoplastics. Afterwards, malleable thermosets or vitrimers were prepared by crosslinking these functional copolymers containing pendent boronic esters with a bis-dioxaborolane in solution or by reactive melt extrusion based on dioxaborolane metathesis (**Figure 2.7 (B)**). Compared to their thermoplastic counterparts, the achieved vitrimers exhibited improved melt strength, dimensional stability at high temperature as well as solvent and environmental stress-cracking resistance. Additionally, they also featured with a self-repaired ability, reprocessability and recyclability.
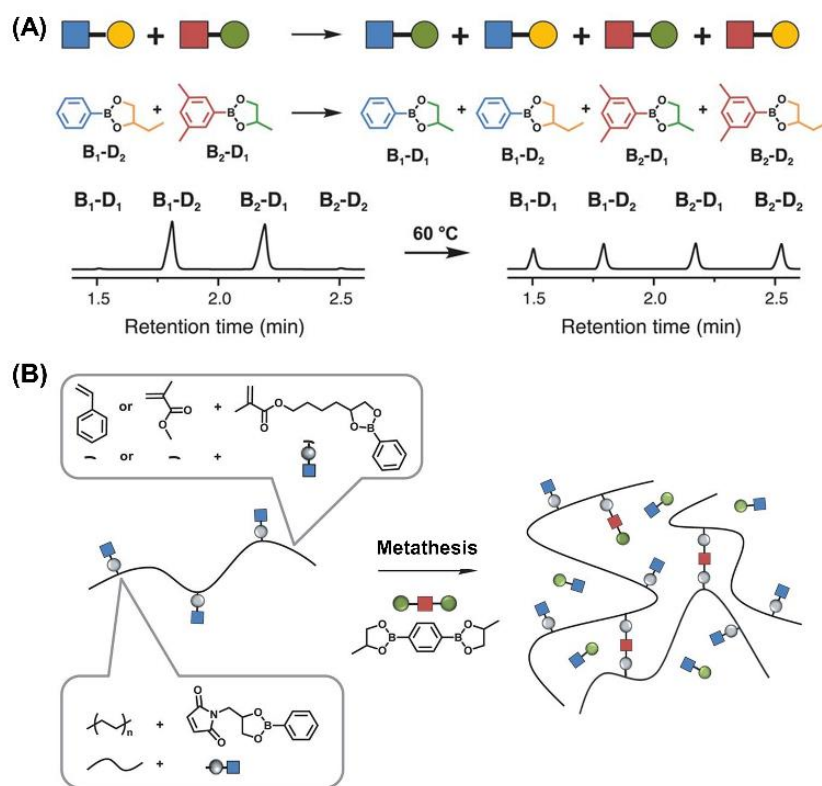
Figure 2.7. (A) Schematic illustration of the direct metathesis of the boronic esters. (B) The synthesis of vitrimers by crosslinking of functional copolymers bearing pendent boronic esters with a bis-dioxaborolane. Reprinted with permission from Ref.[53], copyright (2017) AAAS.

2.6 Radical polymerization

Radical polymerization is the predominately utilized technique for preparing chain growth polymers with high molecular weight, which is suitable for numerous vinyl monomers under mild conditions in the absence of oxygen. Additionally, radical copolymerization of two or more monomers can be easily performed, leading to various copolymers with properties determined by the proportions of the commoners.[145] Conventional radical polymerization refers to free radical polymerization (FRP), which usually exhibits poor control of macromolecular structures, such as dispersity, degree of polymerization and chain architectures. During the recent two decades, reversible deactivation radical polymerization (RDRP), also named as controlled / living radical polymerization, was proposed to solve the above-mentioned problems, as it allows for precious synthesis of well-defined and functional polymers with narrow dispersity and defined architecture.[145-147] In the following section, conventional free racial polymerization (FRP) and three typical reversible deactivation radical polymerization (RDRP) techniques, including nitroxide mediated polymerization (NMP), atom transfer radical polymerization (ATRP) and reversible addition-fragmentation chain-transfer (RAFT) polymerization, will be introduced in detail.

2.6.1 Free radical polymerization (FRP)

Free radical polymerization (FRP) is the most versatile technique for preparing macromolecules both in lab and industrial scale. FRP can be applied for a large number of monomers and easily accomplished in bulk, suspension, solution and emulsion. A typical FRP consist of initiation, propagation, chain transfer and termination processes, as illustrated in **Scheme 2.9**. FRP starts from the initiation process, which includes the formation of initiator radicals and their consecutive addition to monomers. The formed monomer radicals will propagate by rapid and successive addition to other monomers, leading to oligomer and polymer radicals, which will continue propagation. During the propagation process, some new radicals will be formed through transferring radicals to monomer or solvent molecules. Eventually, termination will take place via the coupling or disproportionation reactions.[148] FRP can be initiated by heat, UV-light, electricity and redox reagents, among which, azobisisobutyronitrile (AIBN) and benzoyl peroxide (BPO) are the most commonly utilized thermo- and photo- initiators, respectively.

| Initiation | I_2 | $\longrightarrow$ | $2I^{\cdot}$ |
| | $I^{\cdot}$ + M | $\longrightarrow$ | $P_1^{\cdot}$ |

Initiation I_2 $\longrightarrow$ $2I^{\cdot}$

$I^{\cdot}$ + M $\longrightarrow$ $P_1^{\cdot}$

Propagation $P_1^{\cdot}$ + M $\longrightarrow$ $P_m^{\cdot}$

Chain transfer $P_m^{\cdot}$ + T $\longrightarrow$ P_m + $T^{\cdot}$

Termination $P_m^{\cdot}$ + $P_n^{\cdot}$ $\longrightarrow$ P_{m+n} Coupling

$P_m^{\cdot}$ + $P_n^{\cdot}$ $\longrightarrow$ P_m + P_n Disproportionation
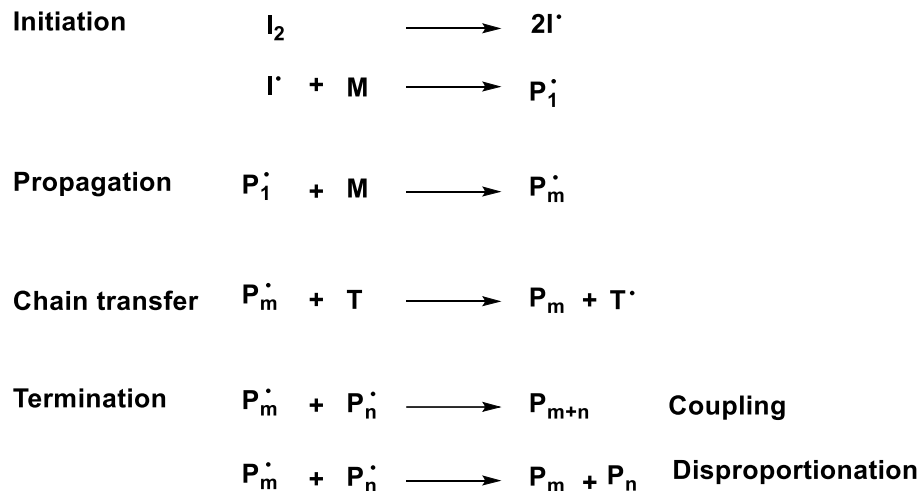
Scheme 2.9. The mechanism of conventional free radical polymerization (FRP).

Despite that FRP has been widely explored to synthesize functional polymers and manufacture commercial products in industry, it still has some obvious disadvantages when it comes to precious polymerizations with low dispersity and complex structures. Therefore, reversible deactivation radical polymerization (RDRP) was proposed and has been playing an important role in polymer chemistry, which will be discussed in the following sections.

2.6.2   Reversible deactivation radical polymerization (RDRP)

2.6.2.1   Nitroxide Mediated Polymerization (NMP)

Nitroxide mediated polymerization (NMP) is based on the reversible combination between propagating polymeric radicals and stable nitroxide free radicals, which yield (macro-) alkoxyamines acting as dormant species to avoid the termination between two macro-radicals, as depicted in **Scheme 2.10.** The dormant species tend to decompose into propagating radicals and nitroxide upon increased temperature until an activation-deactivation equilibrium is established between the dormant and radical species. The equilibrium favors the dormant species due to the relatively higher deactivation rate (K_{deact}) as compared to the activation rate (K_{act}), thus enabling the propagating radicals to be "living" without terminations. Though NMP has been intensively explored for preparing the well-defined polymers, its versatility is still limited by the choice

of monomers. Generally, NMP is suitable for styrene and its derivatives, acrylamides, acrylates, while it loses control with methacrylic esters, vinyl esters and vinyl chlorides.[149, 150]

Alkoxyamines   **Nitroxide radicals**

$$P_n-O-N \overset{R}{\underset{R'}{<}} \quad \underset{k_{deact}}{\overset{k_{act}}{\rightleftarrows}} \quad P_n^{\cdot} \quad + \quad {}^{\cdot}O-N \overset{R}{\underset{R'}{<}}$$

$$k_p \; (M) \quad P_m^{\cdot} \\ k_t$$
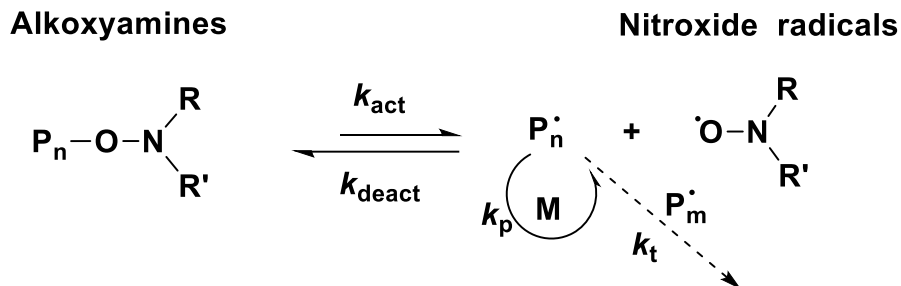
Scheme 2.10. The mechanism of Nitroxide Mediated Polymerization (NMP).

2.6.2.2   Atom Transfer Radical Polymerization (ATRP)

Atom transfer radical polymerization (ATRP) was independently reported by Prof. Matyjaszewski[151] and Prof. Sawamoto[152] in 1995 for the first time. Essentially, it is based on a reversible redox process catalyzed by a transition metal complex, wherein a halogen atom X transfers from the dormant species (PX) to the metal-ligand complex (M_t^n / L) in a lower oxidation state, thus generating the active radicals and the corresponding oxidized metal-ligand complex (X-M_t^{n+1} / L) (as shown in **Scheme 2.11**). Polymer chains grows through the addition of monomers to the propagating radicals in similar manner to the conventional radical polymerization. The oxidized complex (X-M_t^{n+1} / L) acting as the deactivator reduces the concentration of growing radicals, thus minimizing the likelihood of irreversible termination by coupling or disproportionation.[146, 153, 154]

$$P_nX \; + \; M_t^n/L \quad \underset{k_{deact}}{\overset{k_{act}}{\rightleftarrows}} \quad P_n^{\cdot} \quad + \quad X\text{-}M_t^{n+1}/L$$

$$k_p \; (M) \quad P_m^{\cdot} \\ k_t$$
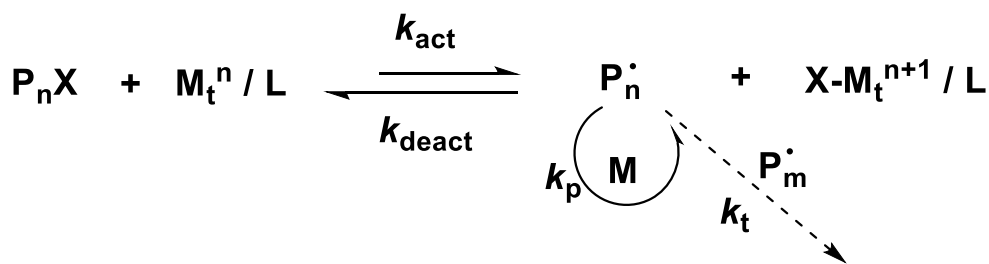
Scheme 2.11. The general mechanism of Atom Transfer Radical Polymerization (ATRP).

Generally, alkyl halides are used as initiators; especially alkyl bromide and chlorine are preferred since they could accomplish fast initiation, rapid and selective migration between the propagating chains and the metal-ligand complex. Theoretically, transition metal / ligand complex, which are capable of performing an electron transfer reaction by the abstraction of a halogen atom, and also rapidly deactivating the growing polymer chains at their oxidized state, could be utilized as the catalyst for ATRP. Copper-based catalyst systems are more superior than their counterparts in terms of versatility and cost.[153] Besides, in regard to the ligands employed in copper-mediated ATRP, nitrogen ligands have been proven to be the most effective and suitable counterparts, whose steric and electronic characters have a great effect on the catalytic activity.[155] Examples of some commonly used *N*-based ligands are listed in **Scheme 2.12**. So far, the controlled polymerizations of various monomers have been successfully accomplished by ATRP, such as styrenes, (meth)acrylamides, (meth)acrylates, and acrylonitrile.[156]

Bpy   **PMDETA**   **HMTETA**

Me₆TREN   **TPMA**
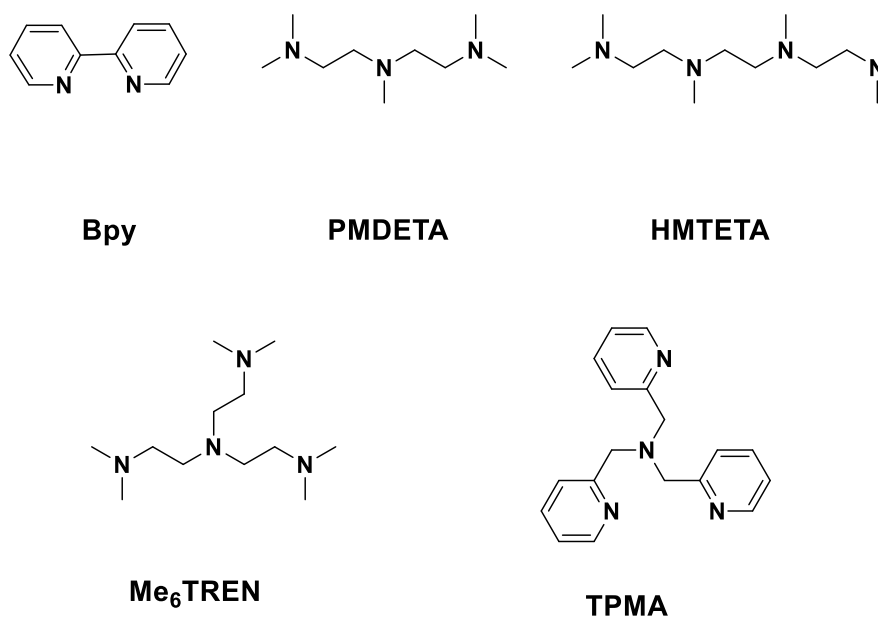
Scheme 2.12. Examples of N-based ligands used for copper-mediated ATRP: 2,2'-Bipyridine (Bpy), *N,N,N',N'*-pentamethyldiethylenetriamine (PMDETA), 1,1,4,7,10,10-hexamethyltriethylenetetramine (HMTETA), tris[2-(dimethylamino)ethyl]amine (Me₆TREN) and tris[(2-pyridyl)methyl]amine (TPMA).

2.6.2.3 Reversible addition-fragmentation chain-transfer polymerization (RAFT)

Reversible addition-fragmentation chain-transfer (RAFT) polymerization was first reported together by Prof. San Thang, Dr. Ezio Rizzardo and Prof. Graeme Moad in 1998.[157] The RAFT protocol makes use of thiocarbonylthio compounds acting as the reversible chain transfer agents (CTAs) to accomplish the controlled synthesis of well-defined functional polymers. In a typical RAFT polymerization, there are normally multi-step reactions between the components as illustrated in **Scheme 2.13**. First, polymeric radicals are generated using conventional thermal or photochemical initiator, such as azobisisobutyronitrile (AIBN) or benzoyl peroxide (BPO); then, the growing polymer chain is captured by the CTAs to deliver a regenerative radical through consecutive addition and fragmentation process; the regenerative racial continues with reinitiation process through consequent addition to the monomers. Afterwards, the new growing polymer chain undergoes another reversible addition and fragmentation reactions through the addition to the CTAs, thus retaining the growing polymeric radicals at the constant low concentration to reduce the likelihood of terminations. In a well-controlled RAFT polymerization, the concentration of initiator should be kept relatively lower than the concentration of CAT, and higher $[CTA]_0$ / $[initiator]_0$ benefits a better control of the polymerization.[158]
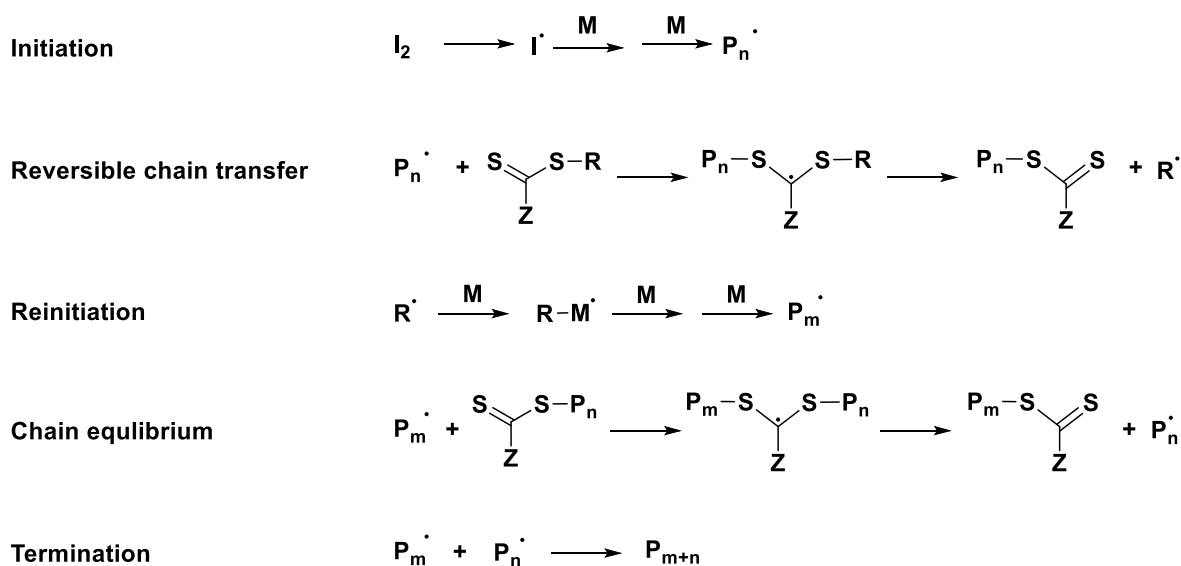
Scheme 2.13. The general mechanism of atom Reversible addition-fragmentation chain-transfer (RAFT) polymerization.

RAFT agents typically consist of thiocarbonylthio groups (S=C-S) with R and Z substituents, wherein R represents the leaving group, which should easily fragment, and the as-formed radical R· should be also active enough to reinitiate the polymerization. Z represents the functional group which promotes the addition of radicals to the C=S bonds, as well as stabilizes the as-formed intermediate radicals. Generally, the efficiency of RAFT agents is determined by the monomer being polymerized, free-radical leaving group R and stabilizing group Z. CTAs with higher stabilizing Z group (such as phenyl group) are more suitable for activated monomers, such as styrenes, acrylates and methacrylates, while CTAs with less stabilizing Z group are more suitable for polymerization of less activated monomers, e.g. vinyl acetate and *N*-vinylpyrrolidone.[158] Furthermore, the synthesized polymer by RAFT polymerization contain a thiocarbonylthio end group, which can be easily transformed into thiol groups by reacting with primary or secondary amines.[159] The end group modification can not only be applied for constructing block and graft copolymers via thiol-based "click" reactions, but also help to eliminate the polymers' color originating from thiocarbonylthio group.[160, 161] The representative RAFT agents and guidelines for selection of RAFT agents for various polymerizations are listed in **Figure 2.8**[160].
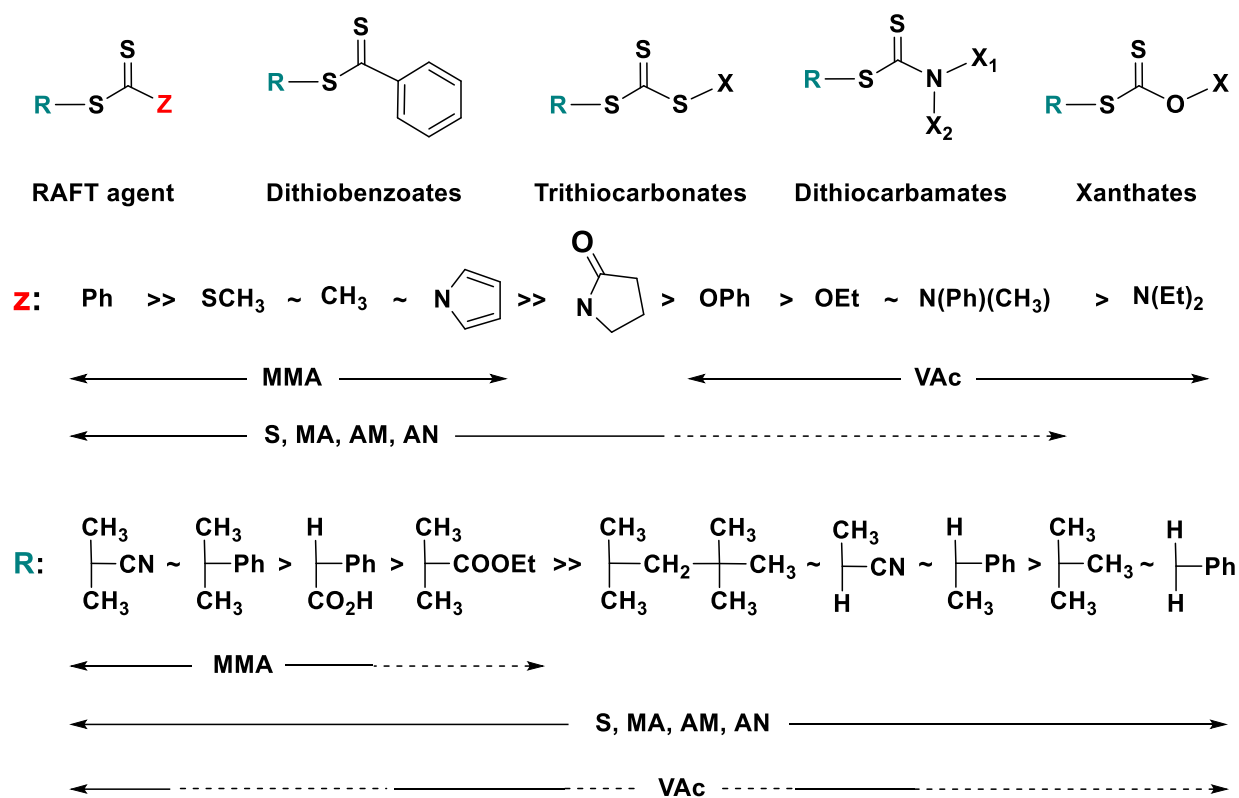
Figure 2.8. The representative RAFT agents and the guidelines for selection of CTAs for various polymerization. For monomer abbreviations see the abbreviations part in the text.[160]

26

2.7 Post-polymerization modification (PPM)

Controlled / living radical polymerizations manifests as alternative methods to allow precise synthesis of functional polymers with well-defined molecular weight and architectures, and broadens the monomer being able to be polymerized at the same time as compared to traditional living cationic and anionic polymerization. However, there are still limitations when it comes to side-chain functionalities which can't be accomplished by utilizing controlled polymerization. Such functional groups may either participate in side reactions or affect the equilibrium between the active and dormant species, leading to poor control of the overall polymerization.[162] Post-polymerization modification (PPM), also coined as *polymer analogous modification* by Staudinger[163] who is the pioneer of polymer science, has paved an alternative avenue to prepare functional polymers bearing versatile functional groups to overcome the limited functional group tolerance using currently available controlled polymerizations.[164] The basic route of PPM with comparison to direct polymerization of functional monomer is schematically illustrated in **Figure 2.9**.[165]
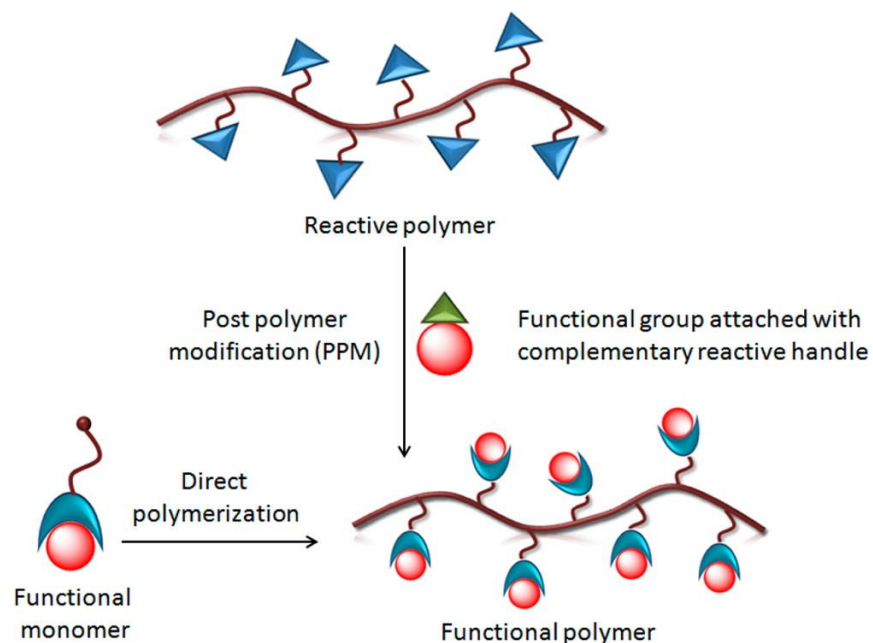
Figure 2.9. Schematic illustration of the synthesis of functional polymer via post-polymerization modification and direct polymerization of functional monomer. Reprinted with permission from Ref.[165], copyright (2016) American Chemical Society.

In a typical PPM, polymerization of a single reactive monomer, which is tolerant towards the polymerization conditions, is first conducted to prepare reactive polymer precursors. Afterwards, the reactive groups decorated on the polymer precursors can be further modified quantitatively and selectively to yield other desirable groups under mild conditions. In comparison, direct polymerization of the functionalized monomers requires the mandatory synthesis of corresponding monomers, which usually suffer from tedious synthetic protocols as well as the limitations in diversity in respect to the monomeric structures. Until now, a plethora of modification methods has been successfully developed for PPM, such as active esters modifications,[165] ketones and aldehydes modifications,[166] copper catalyzed azide-alkyne cycloaddition (CuAAC) [167, 168] as well as thiol-based 'click' reactions,[169, 170] as summarized in **Figure 2.10**. Since active esters modifications and thiol-based 'click' reactions, especially thiol-Michael addition and *para*-fluoro-thiol ligation, are applied for synthesizing functional polymers in this thesis, they will be the focus in the following section.
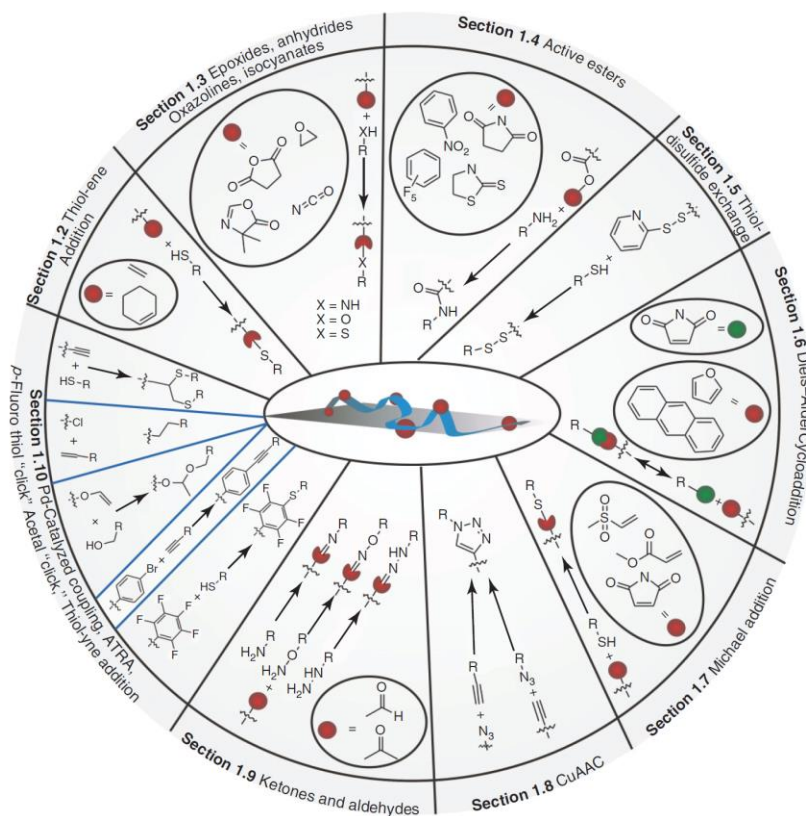

Figure 2.10. The classes of reactions which have been successfully developed for the preparation of functional polymers by the post-polymerization modification (PPM) method. Reprinted with permission from Ref.[164], copyright (2013) John Wiley and Sons.

2.7.1   Active esters post-polymerization modifications

The concept of post-polymerization modification based on active esters was first introduced by Ringsdorf[171]and Ferruti[172] in 1970s. Since then, reactive polymeric precursors obtained from various monomers under mild conditions was continuously proposed using the currently available polymerization techniques. One classic type of active esters is the *N*-hydroxysuccinimide (NHS) esters. However, the main drawback of corresponding polyNAS or polyNMAS is their poor solubility in organic solvents except for dimethylformamide (DMF) and dimethylsulfoxide (DMSO), a problem that can only be addressed by copolymerization NHS with other monomers to enhance their solubility in other organic solvents.[173]

Reactive polymers featuring with active pentafluorophenyl (PFP) ester groups has emerged as attractive alternatives to NHS based polymers due to their better hydrolytic stability, higher reactivity and improved solubility in a wide range of organic solvents.[174] Poly(pentafluorophenyl (methyl) acrylate) (PolyPFP(M)A) with high molecular weight can be easily obtained through homopolymerization of PFP ester monomers using free radical polymerization[175] or RAFT polymerization[176], the latter was also proved to successfully prepare functional polymers with controlled molecular weight and narrow dispersity. Additionally, functional random copolymers and block copolymers containing PFP ester groups are also proposed and widely applied for constructing multi-stimuli responsive polymers,[177, 178] self-assembly nanoparticles,[179, 180] and functionalized surfaces[181, 182] via sequential modification procedures.

Generally, the post-polymerization modification of PFP esters containing polymers can be achieved through two methods, nucleophilic amine substitution and transesterification (**Figure 2.11**). Nucleophilic amine substitution of PFP esters is the most widely investigated route, and the substitution ratio is affected by the type of amine derivatives and PFP monomers. Normally, primary amines show better affinity to PFP esters than secondary ones, and aromatic amines show the lowest substitutional ability. Noteworthy, the reactivity of PolyPFPA towards amines is also superior to that of PolyPFPMA.[165] Besides, the fidelity and versatility of transesterification strategy was exemplified by Das and Théato in 2015, where diverse functional alcohols (primary, second and phenolic) featuring functional groups like alkene, alkyne or acrylate, were successfully anchored to the PFP sits by substitution, and further enabled sequential functionalization using click reactions.[183] The transesterification is catalyzed by Lewis base, such as 4-dimethyllaminopyridine (DMAP) in nucleophilic solvent DMF, and mechanistic investigation clearly suggested that both DMAP and DMF were involved as catalysts in the reaction.
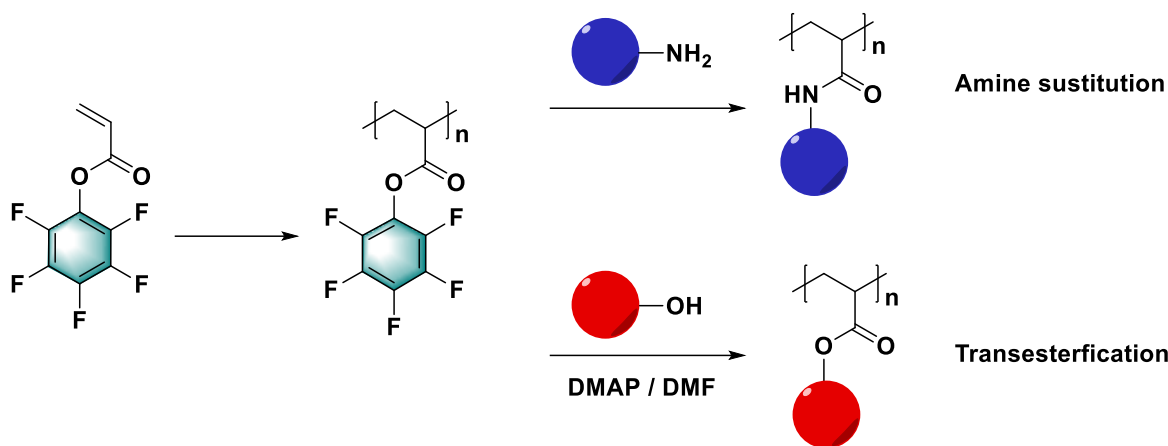
Figure 2.11. General route of post-polymerization modification on reactive polymers bearing PFP esters through nucleophilic amine substitution and transesterification.

2.7.2 Thiol-ene click reaction

The thiol-ene click reaction was first discovered by Posner in 1905,[184] and it is essentially a hydrothiolation reaction between a thiol and an olefin to yield an alkyl sulfide. Thiol-ene click reactions have gained enormous research interest due to their distinct merits of mild reaction conditions, versatile thiol and ene precursors, tolerance to oxygen and water, as well as high conversions and reaction rates.[185, 186] Depending on the mechanism, thiol-ene click reaction can be classified into two types, radical-mediated and base / nucleophile-initiated thiol-ene reactions

The thiol-ene radical reaction is usually thermochemically or photochemically induced, which involves typical chain initiation, propagation, transfer and termination process, as depicted in **Scheme 2.14 (A)**.[187, 188] The thiyl radical was first generated though the reaction of a thiol with a radical initiator, and then it continues to propagate by direct addition to the C=C bond, yielding an intermediate carbon-centered radical. The chain transfer reaction further occurs between the intermediate radical and another thiol, releasing the final thiol-ene product with anti-Markovinikov orientation as well as a new thiyl radical by abstraction of a hydrogen radical from thiol. Possible termination happens between two thiyl radicals via typical coupling reaction.
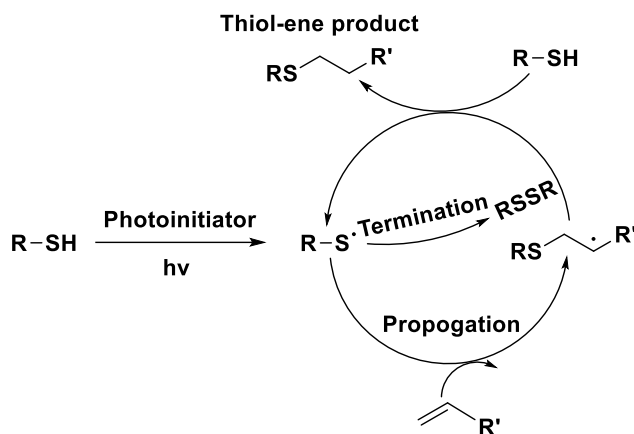
Scheme 2.14. The general mechanistic pathway for radical-mediated thiol-ene reactions.

Base/nucleophile-initiated thiol-ene reaction, which can also be defined as thiol-Michael or conjugate addition reaction, is another method to accomplish hydrothiolation. Wherein, thiolate anion is first generated through the deprotonation of a thiol in the presence of mild base (like trimethylamine) or nucleophile (like dimethylphenylphosphine) catalytic condition. The thiolate, acting as a powerful nucleophile, attacks the activated C=C bond at the electrophilic β-carbon site producing an intermediate carbon-centered anion, which further yields the anti-Markovinikov thiol-ene product through the abstraction of a proton from the reaction media (**Scheme 2.15**)[188, 189].
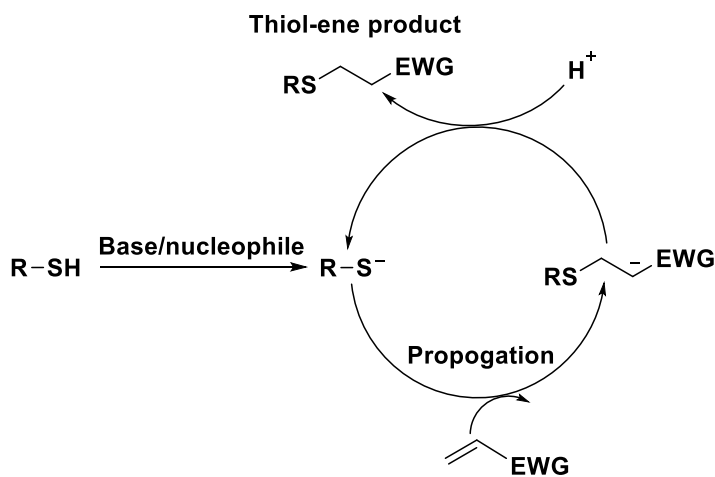
Scheme 2.15. The general mechanistic pathway for thiol-Michael addition reactions.

Normally, electron-withdrawing groups (EWGs), such as esters, amides and nitriles, can activate the C=C double bonds when being adjacent to them, making the double bonds easier attacked by the thiolate anions. Besides, compared to radical-based thiol-ene reaction, termination via anionic coupling process wouldn't take place, thus enabling the thiol-Michael addition reaction to quantitatively proceed at mild conditions. Generally, primary and secondary amines, or nucleophilic alkyl phosphine have been widely utilized as catalysts for efficient thiol-Michael addition reaction between electron-deficient enes and several types of thiols without detectable by-products.[189]

2.7.3 *Para*-fluoro-thiol reaction (PFTR)

The *Para*-fluoro-thiol reaction (PFTR) emerging as a new thiol-based reaction, has obtained great research interest in click chemistry as it paves a facile approach to achieve post-polymerization modification.[170] Essentially, PFTR attributes to a kind of nucleophilic substitution reactions, where the thiol group is first deprotonated by a base, such as 1,8-diazabicyclo [5.4.0] undec-7-ene (DBU) or trimethylamine (TEA), to release a corresponding thiolate, and the thiolate acting as a nucleophile will subsequently attack the para-fluorine of a pentafluoro benzyl (PFB) group. PFTR usually takes place in aprotic polar solvents, like *N,N*-dimethylacetamine (DMAc), *N,N*-dimethylformamide (DMF) and tetrahydrofuran (THF) and proceeds relatively fast at temperatures ranging from ambient to 70 °C. The general mechanism for PFTR is illustrated in **Scheme 2.16**. PFTR was proved to feature high efficiency and significant regioselectivity under mild conditions, leading that only para substituted products are detectable after reaction.[190, 191] Additionally, the substitution ratio can be easily determined by ^{19}F-NMR spectra.[192]
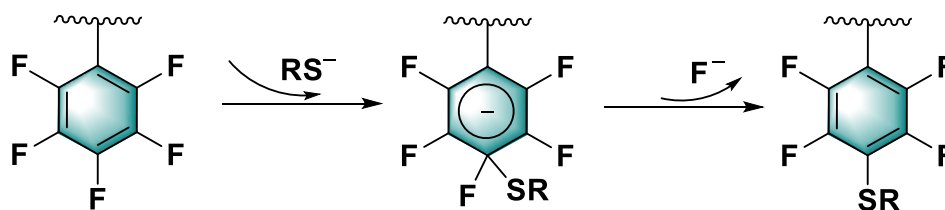
Scheme 2.16. The general mechanism for para-fluoro-thiol reaction (PFTR).

3. Scope and Objectives

Based on the above-mentioned theoretical background, the motivations of this thesis are mainly aiming at designing dynamic functional polymer networks with self-healable character by using a series of reversible bonds, with the emphasize on the organoboron species with dynamic covalent boronic ester bonds. To achieve these goals, three related projects regarding both hydrogel systems as well as bulk polymer networks, are proposed in the following chapters.

Chapter 4 discusses the preparation of conductive hydrogels composites with intrinsic self-healing properties, starting from dynamic noncovalent cross-linked systems based on host-guest and electrostatic interactions, followed by alternative dynamic covalent network incorporated with boronate ester bonds. Their electrical conductivity originating from imbedded single wall carbon nanotubes (SWCNTs) is characterized, and their self-healing ability, involving physical and electrically conductive properties, is further in-depth investigated. This work paves the road for their potential applications in hydrogel-based electronic fields, especially in self-repairing circuit and soft sensors.

The frontiers of boronic ester chemistry in dynamical hydrogel systems are further investigated in Chapter 5. By designing functional copolymers decorated with pendent acrylate and 1,2-diol groups, as well as thiol-functionalized amphiphilic Pluronic F-127 (PF-127) as macro cross-linker, thus hydrogel with two distinctive dynamic cross-linking can be easily obtained through borax catalyzed thiol-acrylate Michael addition reaction and borax-diol chemistry. The mechanical properties of the as-fabricated hydrogel, including anti-fatigue, compressibility and stretchability, as well as its self-healing efficiency, are further investigated and evaluated. This work significantly broadens the application of borax-catalyzed chemistry within the field of self-healable hydrogel networks.

The emphasize of Chapter 6 moves from hydrogel systems to bulk polymeric networks. In detail, a dynamically cross-linked network constructed with reversible boronic ester bonds is synthesized via *para*-fluoro-thiol click reaction (PFTR). Prior to the polymeric network construction, a model reaction is conducted to gain insight into the PFTR ligation chemistry under different catalytic superbases, while avoiding the analytical challenges originating from the insolubility of the networks. The optimized reaction conditions will then be transferred to the formation of dynamic covalent networks. The thermodynamic behavior of the polymeric network, as well as its malleability and self-healing ability are investigated in

depth. This work is envisioned to be a new platform for the development of dynamic materials by the use of the unique chemistry of PFTR ligation.

Conductive hydrogel composites with autonomous self-healing properties[*]
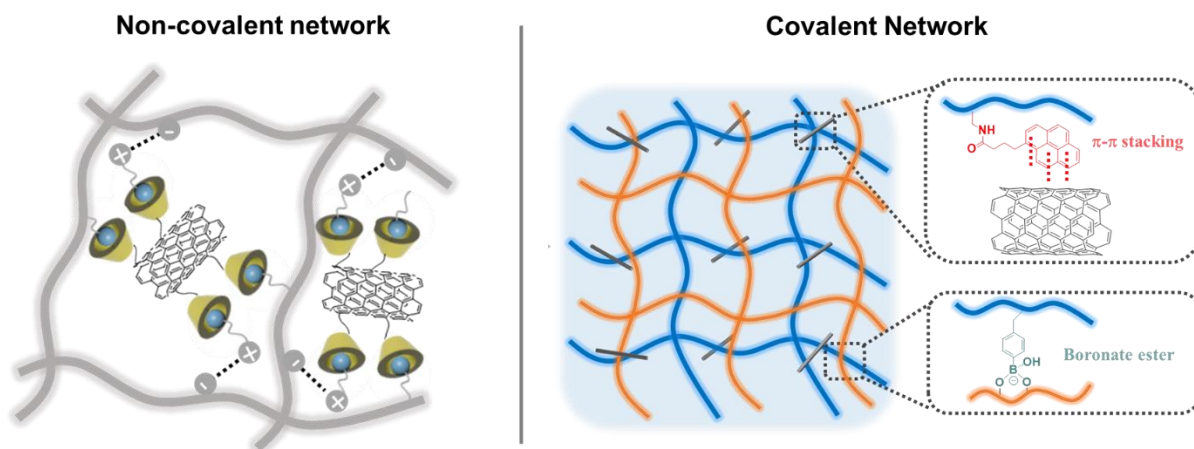
Hydrogels are wet and soft materials with a three-dimensional structure, where hydrophilic polymers chains are physically or chemically crosslinked with each other, leaving large space (50-90%) for water content. Thus, hydrogels have emerged as well-suitable materials in biomedical fields because of their distinctive feature, including good biocompatibility, adjustable stiffness and porous structure.[194-196] Conductive hydrogels, merging the merits of electrically conductive materials and human tissues-like nature of hydrogels, have gained enormous research interest in bioelectronic fields during the past decades, such as biosensors,[197, 198] bio-actuator[199, 200] and artificial e-skins.[201, 202] Generally, conductive hydrogels can be directly prepared by incorporating some conductive fillers, such as metallic nanoparticles,[203] single and multi-wall carbon nanotubes (CNTs),[204] as well as graphene nanosheets,[205] into the cross-linked hydrogel networks. However, the main drawback of this method is that aggregation usually occurs during the gelation process, leading to an undermined conductivity and inhomogeneous mechanical properties at the same time.[206-208] Therefore, a chemical modification of conductive fillers to render them well-dispersible in aqueous solution is necessary prior to the fabrication of the conductive hydrogels.

For CNTs, their limited solubility attributes to the high aspect ratios and strong van der Walls interactions, therefore several common approaches have been proposed to tackle this problem. One method is to manipulate covalent modifications on the surface, which involves functionalization and direct attachment of chemical moieties like carbenes, nitrenes and thiolethers, onto the sidewalls of CNTs. These covalent modifications can efficiently endow CNTs with improved solubility and high dispersion stability, while the π-conjugation of CNTs is disrupted during a chemical process, which results inevitably in affecting their electronic properties.[209] Alternatively, noncovalent functionalizations on CNTs was proposed to circumvent the disadvantages of covalent modifications. This can be easily approached by physical adsorption of functional moieties on CNTs surface through π-π stacking, hydrophobic, electrostatic or van-der-Waals forces.[210] Among the diversity of functional groups, pyrene moieties, either as small molecules or polymer derivatives, are intensively explored to facilitate dispersion of CNTs in both organic solvents and aqueous solution due to their strong interaction with CNTs sidewalls through π-π stacking.[211] Yet, conventional conductive hydrogels couldn't be compared to human skin despite being imparted with an electric conductivity, particularly because of their lack of a self-healing ability. Thus, it still remains a challenge to prepare dual-functional hydrogels with both electrical conductivity and intrinsic self-healing ability to create more suitable and durable materials for biomedical applications.

In this chapter, it was aimed to construct a SWCNTs based conductive hydrogel composite with autonomous self-healing properties by incorporating dynamic bonds. To achieve this, two different cross-linking systems were designed. In **Chapter 4.1**, a first trial to build in hydrogel composites based on host-guest interaction and electrostatic interaction will be introduced. In **Chapter 4.2**, alternative hydrogel networks based on dynamic boronate ester bonds will be introduced and in-depth characterized. In both cross-linking systems, pyrene moieties were introduced to facilitate the homogenous dispersion of SWCNTs in aqueous media, thus alleviating SWCNT aggregations, and endowing the hydrogels with electrical conductive properties. The SWCNTs dispersion in water, as well as the electrically conductive and self-recovery ability of the formed hydrogels will be comprehensively discussed in the following section.

4.1 Conductive hydrogel composites based on host-guest and electrostatic interactions[†]

4.1.1 Synthetic strategy for the preparations of hydrogel composites
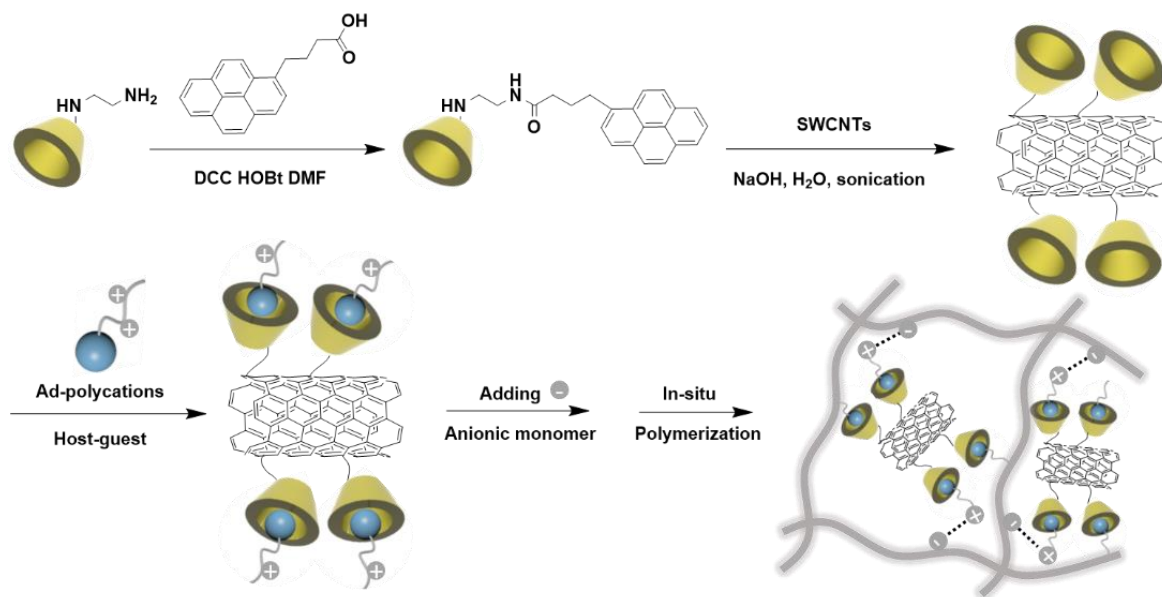
Figure 4.1.1. The schematic illustration of the route for preparations of hydrogel composites based on host-guest and electrostatic interactions.

The schematic illustration of the route for the hydrogel preparation is depicted in **Figure 4.1.1**. Briefly, *β*-CD decorated with pyrene groups (i.e. Py-*β*-CD) was first synthesized though sequential substitution reactions (**Chapter 8.3.1-8.3.3**). Since pyrene moieties can improve the solubility of SWCNTs in aqueous solution by physical π-π stacking interactions, evenly dispersion of SWCNTs could be easily achieved upon the modification. Additionally, pyrene-modified SWCNTs were capable of accommodating with adamantane (Ad)-decorated polymer matrix via host-guest interactions. Polycations with adamantane moieties as end-chain functional groups were prepared by atom transfer radical polymerization (ATRP), wherein an adamantane derivative served as the ATRP initiator. After incorporating the anionic monomer into the mixed aqueous solution of pyrene-modified SWCNTs and as-synthesized polycations, hydrogel composites could be easily obtained by *in-situ* redox polymerization.

4.1.2 Characterization of Py-*β*-CD/SWCNTs hybrids
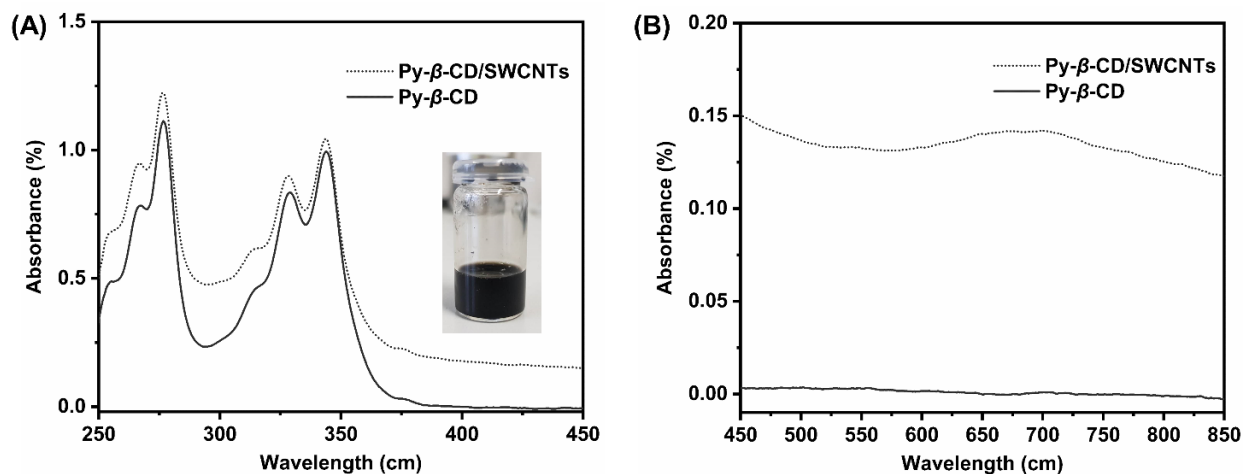
Figure 4.1.2. The characterization of Py-*β*-CD/SWCTs hybrids. (A) The UV-vis spectrum of Py-*β*-CD/SWCTs (short dot line) and Py-*β*-CD (solid line) in the region of 250 - 450 nm in 0.1 M NaOH aqueous solution. Insert image, the photograph showing the stable Py-*β*-CD/SWCTs suspension in aqueous solution. (B) The UV-Vis spectrum of Py-*β*-CD/SWCTs (short dot line) and Py-*β*-CD (solid line) in the region of 250 - 450 nm.

First, UV-vis analysis was performed to characterize the Py-*β*-CD/SWCNTs hybrids, as shown in **Figure 4.1.2 (A)**. Both Py-*β*-CD/SWCNTs hybrids and Py-*β*-CD showed the characteristic pyrene absorption bands

in the region from 250 to 450 nm, while the pyrene absorption peaks of Py-β-CD/SWCNTs hybrids were slightly blue-shifted compared to that of Py-β-CD, attributed to the π-π stacking interactions between the pyrene groups of Py-β-CD and SWCNTs. Additionally, in comparison to the absorption spectrum in the region from 450 to 850 nm as illustrated in **Figure 4.1.2 (B)**, Py-β-CD/SWCNTs hybrids displayed distinctive peaks at the range of 500-800 nm associated with interband transitions between the mirror spikes in the density of states of individualized SWCNTs,[212, 213] further manifesting the well-dispersed SWCNTs in aqueous solution as visually evidenced by the inserted photograph in **Figure 4.1.2 (A)**.

4.1.3   Characterization of Py-β-CD/Adamantane inclusion complexes

In order to evidence the intramolecular interactions between AD and β-CD moieties, a 2D NMR NOESY spectrum was recorded between the Py-β-CD and adamantane derivative, as shown in **Figure 4.1.3**. As expected, cross-resonances (i.e. NOE) at 2.2, 2.1 and 1.6 ppm (green circles in **Figure 4.1.3**) were observed, which in turn, could be assigned to the anticipated interaction between the protons from the cavity of β-CD and the protons from adamantane moieties, thus revealing the successful formation of the stable inclusion complexes.
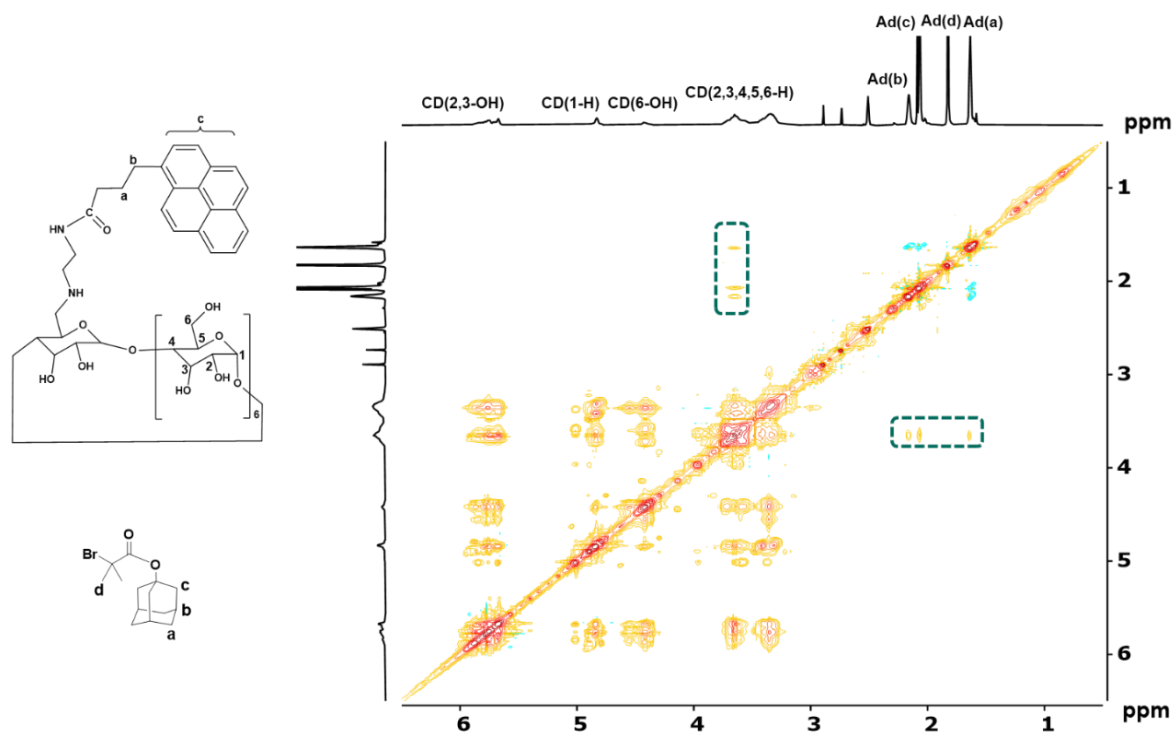
Figure 4.1.3. ^{1}H-^{1}H NOESY spectrum (600 MHz, in DMSO-d_6) of the inclusion complexes between the Py-β-CD and adamantane derivative utilized as the initiator for the ATRP polymerization.

4.1.4 Fabrication and characterizations of conductive hydrogel composites

Prior to the fabrication of hydrogel composites, the polycation poly((3-acrylamidopropyl) trimethylammonium chloride) (PAMPT) was synthesized with adamantane as the end-chain functional group via ATRP polymerization (**Chapter 8.3.4 and Chapter 8.3.8**). The synthesized polycations were then mixed with Py-*β*-CD in aqueous solution to form inclusion complexed though host and guest interactions. Afterwards, hydrogel composites were obtained by adding anionic monomer sodium 4-vinylbenzenesulfonate (NaSS) into the polycation/SWCNTs aqueous solution, followed by *in-situ* polymerization under the initiation of ammonium persulfate (APS) and accelerator *N,N,N′,N′*-tetramethylethylenediamine (TMEDA), as depicted in **Figure 4.1.4 (A)**. Within the hydrogel composites, reversible electrostatic interactions between the polycation (PAMPT) and polyanion (PNaSS) served as the dynamic cross-links to facilitate the gelation process, and endowed the hydrogel with a self-healing ability, while the evenly dispersed SWCNTs built the conductive channel and concomitantly imparted the hydrogel with electrically conductive character.
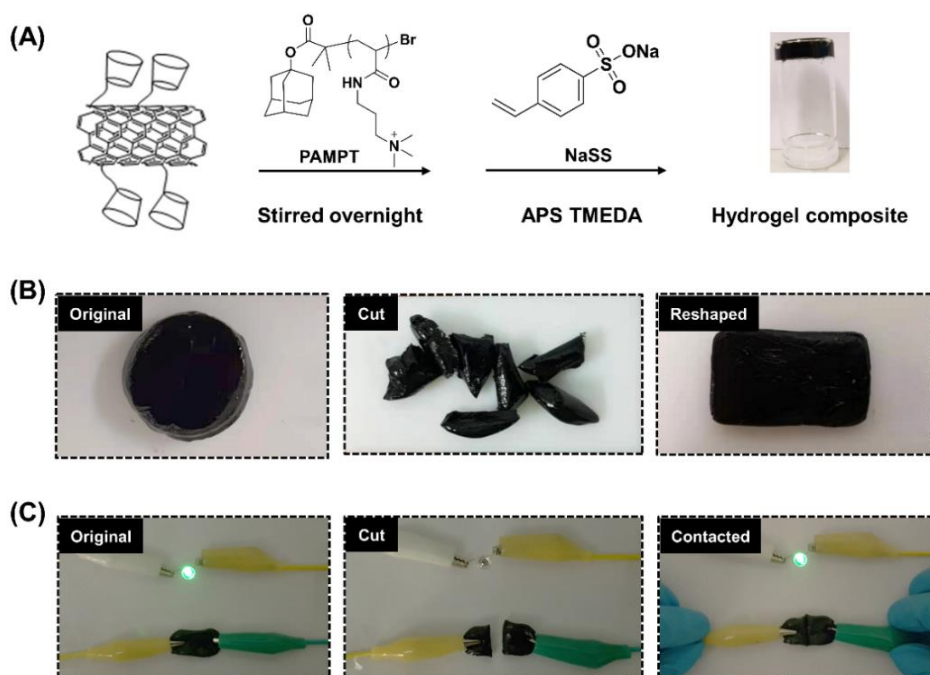
Figure 4.1.4. (A) Schematic illustration of the formation of conductive and self-healing hydrogels. (B) Photographs showing the physical self-recovery process of the hydrogel sample. (C) Photographs showing the recovery process of electrical conductivity.

To qualitatively characterize its conductive and self-healable properties, a series of cut-and-contact tests on the hydrogel samples were performed as illustrated in **Figure 4.1.4 (B).** The disk-shaped hydrogel was first cut into small pieces and then transferred to a PTFE model. After being compressed for 5 minutes at ambient temperature, the fractured pieces were totally integrated and reshaped into a rectangle sample, revealing its fast physically assisted self-healing ability. Additionally, its electrically self-healing character was further investigated by connecting the hydrogel sample into a circuit with a LED light as the indicator, as shown in **Figure 4.1.4 (C)**. The LED was first successfully lighted by an external voltage (5 V) with the original hydrogel sample as a conductor, demonstrating its electrically conductive property. Instead, once the hydrogel was cut into two pieces, the LED indicator was immediately switched-off in the open-circuit state. When the fractured pieces were placed into contact, the dynamic linkages on the damaged interfaces re-associated spontaneously, thus restoring the circuit to illuminate the LED again, revealing the success recovery in the electrical conductivity of the hydrogel sample.

While the conductive and self-healable hydrogel based on electrostatic and host-guest interactions was successfully prepared and characterized, nevertheless, the tedious synthesis protocols starting from small molecules to subsequent ATRP polymerizations could limit its practical applications. Besides, physically cross-linked networks that held together with non-covalent bonds, i.e. electrostatic and host-guest interactions, are often unstable to small environmental perturbations and lack robustness.[36] Accordingly, recent research has shifted its focus on dynamic covalent networks, wherein the reversible covalent bonds are incorporated into the cross-linked systems in order to endow the networks with higher stability and robustness.[20, 60] Therefore, a new and relatively facile method to fabricate SWCNTs based conductive hydrogel composite with self-healing properties is further proposed, which is based on dynamic covalent boronate ester bond. This method makes use of post-modification polymerization, thus avoiding complex synthesis route while maintaining the important role of pyrene moieties. The fabrication of the new hydrogel composite and its characterization will be discussed in details in the following content.

4.2 Conductive composites based on dynamic boronate ester bonds[‡]

In this project, a new SWCNTs based conductive hydrogel composite with intrinsically self-healing properties is proposed. To achieve this, a functional copolymer decorated with pendent pyrene and phenylboronic acid moieties was synthesized via reversible addition-fragmentation chain transfer (RAFT) polymerization and sequential post-polymerization modification. Essentially, pyrene moieties were included to facilitate the homogenous dispersion of SWCNTs in aqueous media, thus alleviating SWCNT aggregations, and endowing the hydrogels with electrical conductive properties. Furthermore, phenylboronic acid moieties were able to provide dynamic boronate ester linkages with diol groups of PVA chains. Respectively, the reversible association/dissociation process between boronic acid and diol groups is expected to contribute to the self-healing ability upon damage. Last but not at least, the conductivity and self-recovery ability in electric conductivity is investigated.

4.2.1 Synthesis and characterization of the functional copolymer
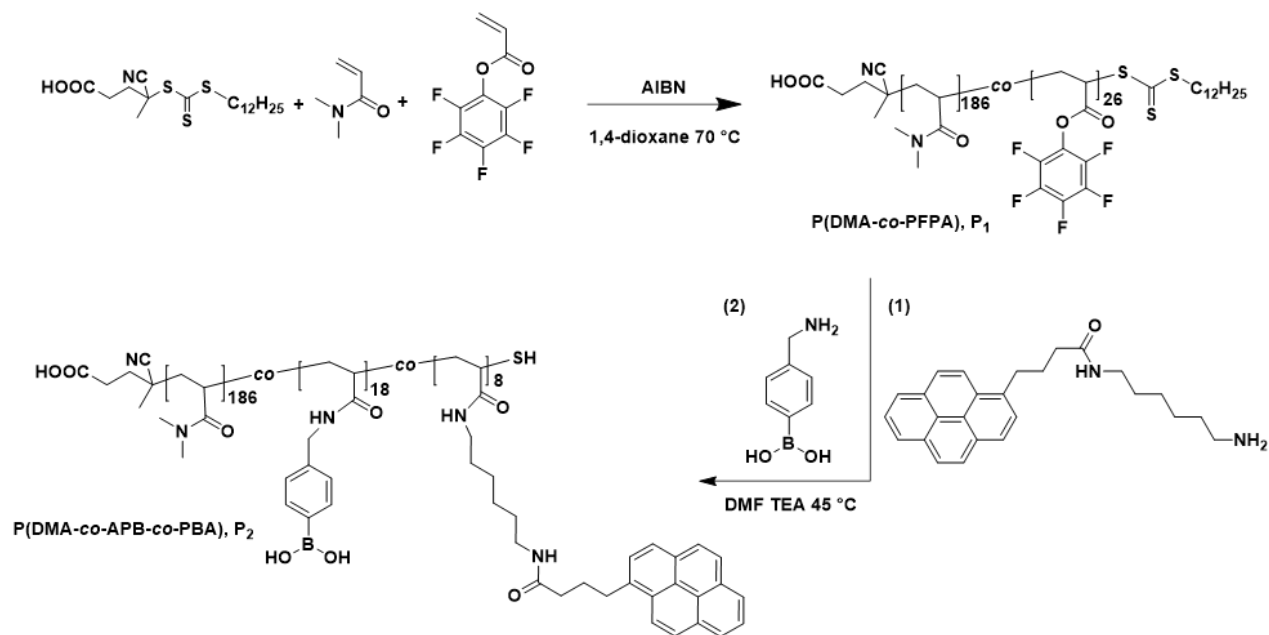
Scheme 4.2.1. The synthetic route towards functional copolymer P(DMA-*co*-APB-*co*-PBA), P2. First copolymer P(DMA-*co*-PFPA), P1, was synthesized via RAFT polymerization, and subsequent nucleophilic post-polymerization modification was performed to deliver copolymer P2.

The functional copolymer P(DMA-*co*-APB-*co*-PBA) (P2) decorated with pendent pyrene and phenylboronic acid moieties was prepared via a RAFT polymerization and sequential post-polymerization modification, as depicted in **Scheme 4.2.1**. To accomplish the amine substitution modification, amine end-functionalized pyrene, i.e. *N*-(6-aminohexyl)-4-(pyren-1-yl) butanamide (APB), was synthesized in a sequential two step procedures, and characterized with ^{1}H-NMR, ^{19}F-NMR and FT-IR spectroscopy to demonstrate the purity of the compound (**Chapter 8.3.6 and 8.3.7**). Subsequently, a linear random precursor copolymer, i.e. P(DMA-*co*-PFPA) (P1), featuring reactive pentafluorophenyl ester groups was synthesized by RAFT polymerization.

As shown in **Figure 4.2.1 (A)**, the ^{1}H-NMR spectrum of P(DMA-*co*-PFPA) facilitated to estimate the composition of P1 by comparing the integrals of signals (e+d) at 2.76-3.18 ppm and signals (b) at 2.54-2.75 ppm with the end methyl groups at 0.88 ppm from the chain transfer agent (CTA). Accordingly, P1 consisted of 186 DMA and 26 PFPA repeating units, respectively. The corresponding ratio of PPFPA repeating units was calculated to be 12.2 mol%, which was in close proximity with the feeding molar ratio (i.e. 10 mol%). Besides, the number average molecular weight of P1 was 2.32×10^4 g mol^{-1} as determined by gel permeation chromatography (GPC) in DMAc as eluent, which was in accordance with the theoretical value (2.53×10^4 g mol^{-1}), thus suggesting a well-controlled copolymerization. Note, the hydrophilic DMA monomer was the comonomer of choice, since it imparted P1 with good solubility in water.

In a next step, copolymer P(DMA-*co*-APB-*co*-PBA) (P2) was obtained by substituting sequentially the pentafluoropheyl esters parts of P1 with amine nucleophiles, e.g. *N*-(6-aminohexyl)-4-(pyren-1-yl) butanamide (APB) moiety, and then with a slight excess of (4-aminomethylphenyl) boronic acid (PBA). Compared to P1, the ^{1}H-NMR spectrum of P2 (**Figure 4.2.1 (B)**) showed additional signals (k) at 8.30–7.86 ppm, which were assigned to pyrene groups from *N*-(6-aminohexyl)-4-(pyren-1-yl) butanamide (APB), as well as distinctive peaks (j) at 7.85–7.67 ppm, (i) at 7.28–7.18 ppm and (h) at 3.37–3.21 ppm, which attributed to the aromatic and methylene proton signals from (4-aminomethylphenyl) boronic acid (PBA) groups, responsively. Besides, the integrals of protons from k and j were calculated, and apparently were in agreement with the theoretical feeding molar ratio of APB: PBA as 30: 70, therefore demonstrating the well-controlled post-modification process of P1 in order to deliver P2. (**Figure B1, Appendix**)
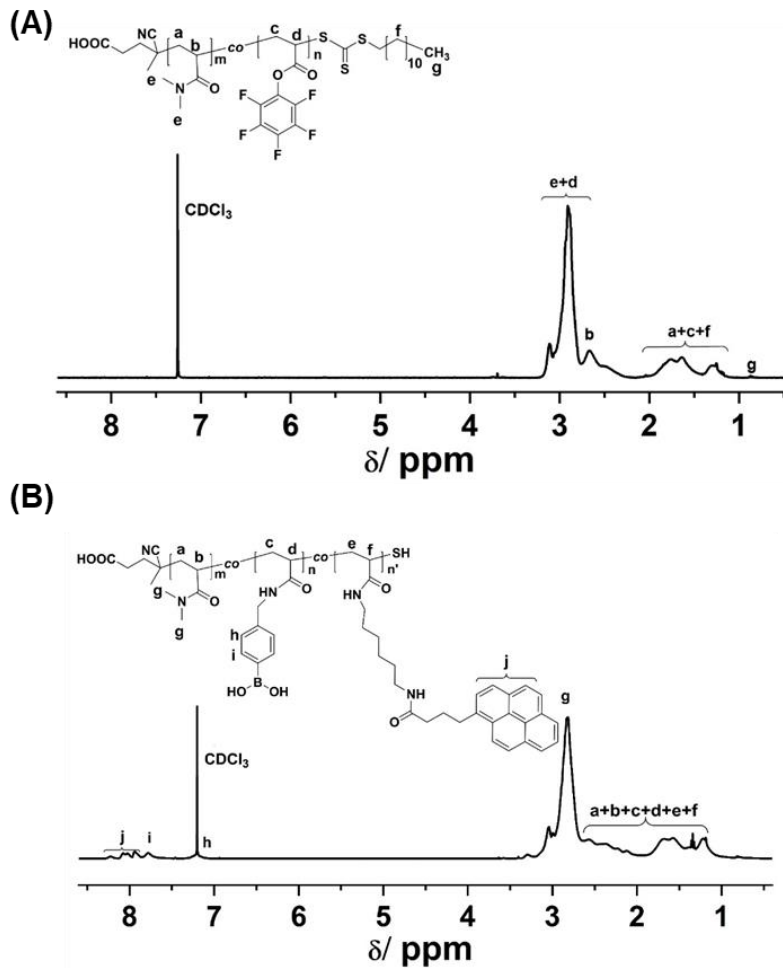
Figure 4.2.1. ^{1}H-NMR (400 MHz, in CDCl$_3$) spectra of (A) P(DMA-*co*-PFPA) and (B) P(DMA-*co*-APB-*co*-PBA), respectively P1 and P2.

The nucleophilic amine substitution process was monitored via ^{19}F-NMR and FT-IR. As shown in **Figure 4.2.2 (A)**, the complete disappearance of characteristic signals from PFP ester at (δ) -152.54, -157.44, -162.05 ppm in the ^{19}F-NMR spectrum revealed the thorough and successful modification results. In similar manner, the disappearance of indicative pentafluorophenyl ester bands at 1780 cm^{-1} (C=O ester stretching bond), 1517 cm^{-1} (aromatic -C$_6$F$_5$ stretching bond), and 998 cm^{-1} (C-F stretching bond) in the FT-IR spectra confirmed the successful modification results. Moreover, a broad band at 3433 cm^{-1} attributed to -OH groups of phenylboronic acid, as well as a new ester band at 1720 cm^{-1} attributed to C=O stretching vibration from pyrene moieties, further demonstrated the success of the nucleophilic substitution.
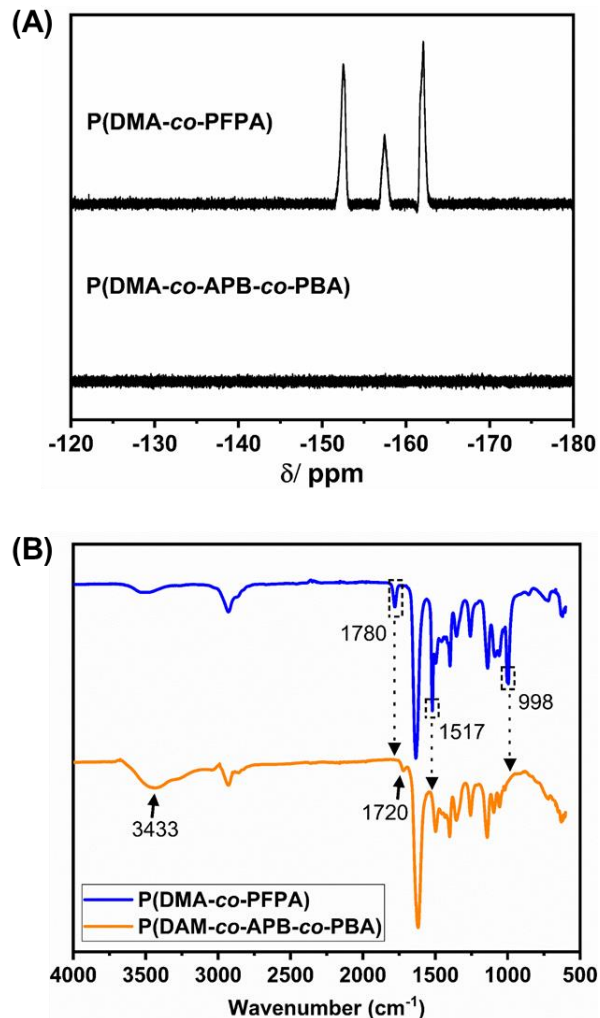
Figure 4.2.2. (A) ^{19}F-NMR (377 MHz) spectra of P(DMA-*co*-PFPA), P1 and P(DMA-*co*-APB-*co*-PBA), P2; (B) FT-IR spectra of P(DMA-*co*-PFPA), P1 (blue line) and P(DMA-*co*-APB-*co*-PBA), P2 (yellow line).

4.2.2 Characterization of SWCNTs suspension in water

The interaction between pyrene moieties and SWCNTs as well as the stability of SWCNTs suspension were characterized by UV-Vis analysis. As shown in **Figure 4.2.3 (A)**, compared to the characteristic absorption peaks of P2 at 317, 331, and 347 nm originating from pyrene moieties, the corresponding absorbance peaks of P2/SWCNTs were slightly shifted to 316, 330 and 346 nm, indicating the formation of π-π stacking hybrid between pyrene groups and SWCNTs.[214] Additionally, compared to absorbance spectrum of P2 within the range of 400-1000 nm, P2/SWCNTs displayed distinctive peaks at the range of 550-900 nm arise

from interband transitions between the mirror spikes in the density of states of individualized SWCNTs,[213] further demonstrating the well dispersion of SWCNTs, as shown in **Figure 4.2.3 (B)**.
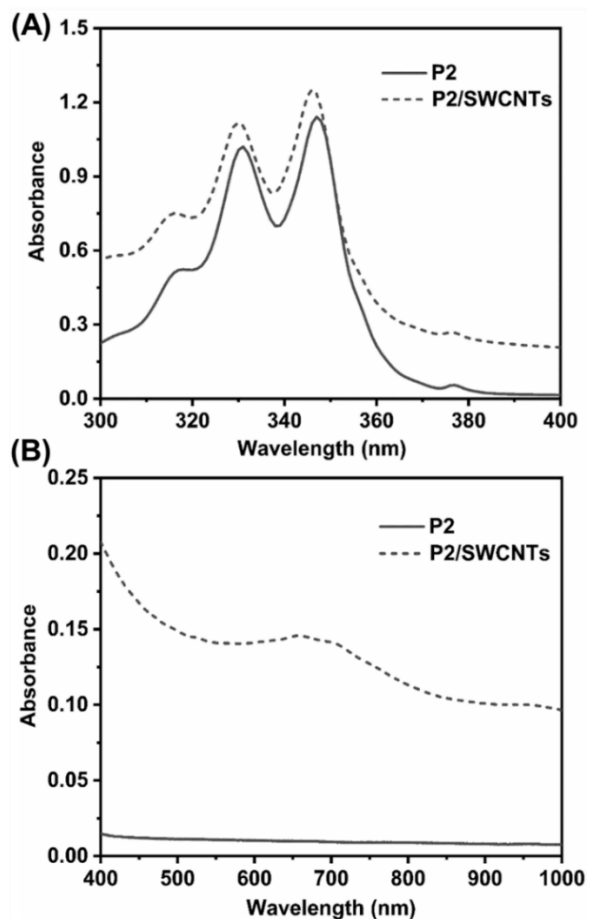
Figure 4.2.3. UV-vis absorbance spectra of P2 and P2/SWCNTs dispersion in aqueous solution within the range of 300-400 nm (A) and 400-1000 nm (B).

Besides, the stability of the standing dispersion without (sample A) and with P2 (sample B) was evaluated by monitoring their transmittance at 632 nm. As shown in **Figure 4.2.4 (A)**, immediate precipitation was observed for sample A in the absence of P2 during the first day and the transmittance reached up to 90% after the first two days, indicating that SWCNTs without P2 modification sedimentated rapidly in aqueous solution. While, the transmittance of the SWCNTs/P2 dispersion only slightly increased to 1.2 % in the first day and then kept stable at around 2% during the following days, revealing its good stability. The visualized

photographs of sample A and B in the inset of **Figure 4.2.4 (A)** after one-week storage could further prove the effect of P2 on the stability of SWCNTs dispersions. Since pyrene group could exfoliate SWCNTs from their bundles state through π-π stacking effect, the hydrophilic copolymer P2 was clearly capable of alleviating the aggregation of SWCNTs in aqueous media, thus forming stable dispersions even over one month, as demonstrated visually in **Figure 4.2.4 (B)**.
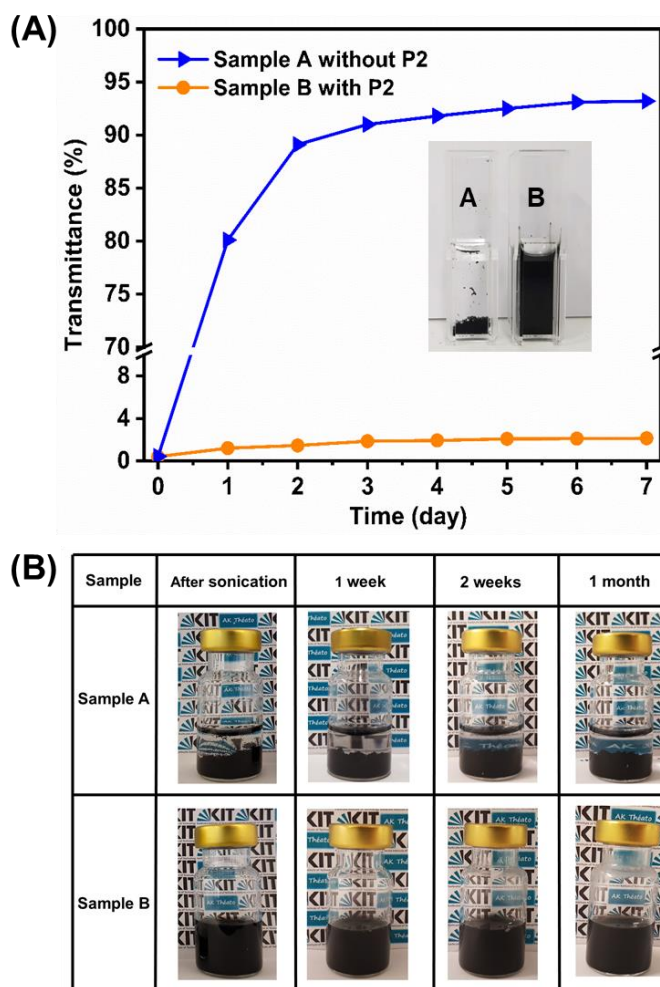
Figure 4.2.4. (A) UV-vis transmittances at 632 nm of SWCNTs aqueous suspension without and with P2, respectively sample A and B. The content of SWCNTs is 0.02 wt%. Inset: photographs of the dispersed sample A and B after one week. (B) Photographs of SWCNTs aqueous suspension without and with P2, respectively sample A and B, after sonication 20 min, one week, two weeks and one month.

4.2.3 Fabrication and characterization of hydrogel composites

The conductive and self-healed hydrogel composites were prepared via dynamic cross-linking of P(DMA-co-APB-co-PBA) (P2), PVA and SWCNTs at neutral pH 7.0 in aqueous solution, as schematically illustrated in **Figure 4.2.5**. For this, P2 and SWCNTs were mixed together in ultra-purified water to form well-dispersed suspension, afterwards, PVA solution (10 wt%) was added into the suspension and the whole mixture was vigorously stirred at room temperature until gelation occurred. It should be noted that although the optimum pH for the complexations between the phenylboronic acids and diol groups is above 8.8 (the pK_a of phenylboronic acid is around 8.8),[110] the formation of boronate ester bonds still could happen under neutral pH due to some sufficient amount of ionisable boronic acid groups as well as the rich *cis*-diols along the PVA chains.[121, 215] Within the cross-linked system, evenly dispersed SWCNTs built the conducting channels for the network, while tetrahedral boronate ester bonds were formed through reversible complexation between the phenylboronic acids and adjacent diol groups along PVA chains, serving as the dynamic cross-linking sits for the hydrogel composites, as well as imparting the hydrogels with autonomous self-healing ability without any external stimuli.
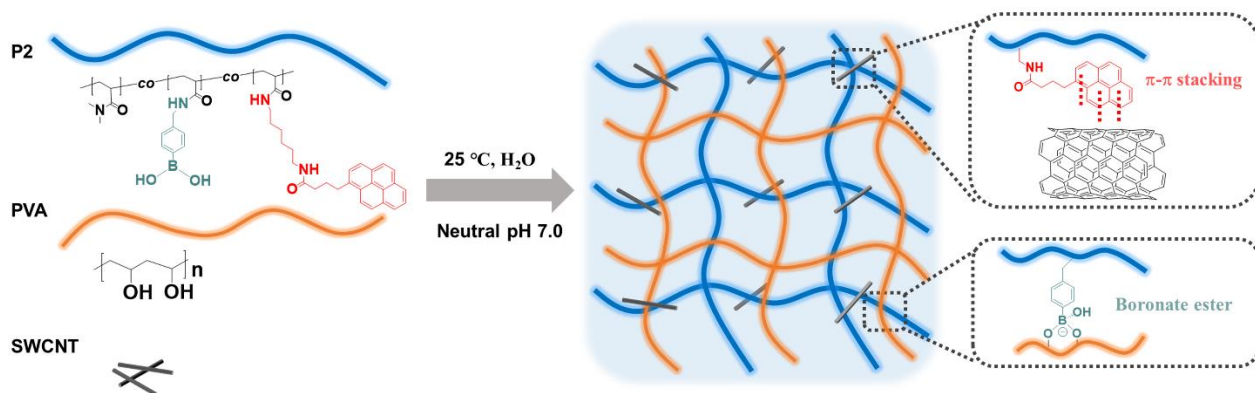
Figure 4.2.5. Schematic illustration of the formation of conductive and self-healing hydrogels by dynamic cross-linking of P(DMA-*co*-APB-*co*-PBA) (P2), PVA and SWCNTs at neutral pH.

The as-fabricated of hydrogel composites were shown in **Figure 4.2.6 (A)**. In order to demonstrate their homogeneous internal networks, hydrogel samples were first freeze-dried and then their morphology was recorded via SEM characterization. The obtained images under magnification of 2 µm and 1 µm were illustrated in **Figure 4.2.6 (B) and (C),** respectively. The freeze-dried hydrogel samples clearly demonstrated the three dimensional interconnected network with uniformly porous microstructures, suggesting that SWNCNTs were well distributed and evenly incorporated into hydrogels. Besides, some intertwined micro-fibrils could also be observed in the cross-liked network due to the supramolecular interaction between the PVA and P2, as shown in **Figure B3** in the appendix.
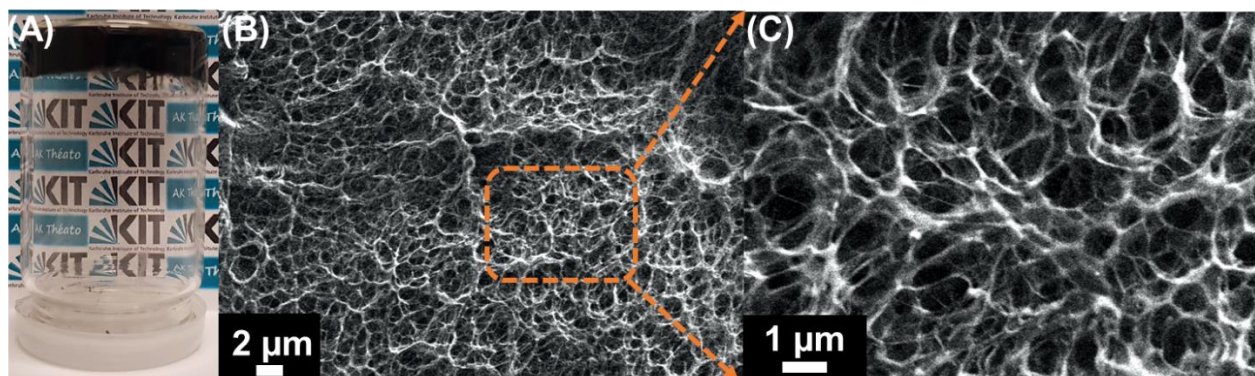
Figure 4.2.6. (A) Photography showing the as-fabricated hydrogel composite. (B) and (C) SEM images of the freeze-dried hydrogel samples under different magnification (2 µm and 1 µm, respectively).

The self-healing ability of the hydrogels was tested by dynamic rheology. Oscillation strain-sweep measurements were carried out first to determine the linear viscoelastic region, as well as the critical gel-sol transition point. As shown in **Figure 4.2.7 (A)**, the G' and G'' values were practically constant under the strain region from 1% to 10%. On the contrary, when the strain kept increasing to 100%, G' tend to decrease while G'' began to increase gradually, until a crossover occurred at strain $\gamma = 70\%$, therefore clearly indicating the critical point where the gel network was significantly disrupted and transformed into the sol. Complementary, alternate strain-sweep measurement was performed to measure the self-healing ability under the cyclic change from small strain ($\gamma = 1\%$) to large strain ($\gamma = 100\%$). As shown in **Figure 4.2.7 (B)**, when the strain was kept constant at 1 %, G' was larger than G'', demonstrating the gel state; on the contrary,

once the sample was treated with large strain of 100%, G' decreased dramatically from 13500 Pa to 1550 Pa because of the disruption of the hydrogel network. Ultimately, when the strain was recovered back to 1%, the G' practically recovered to its original value. Furthermore, cyclic tests were repeated three times and exhibited the similar phenomenon, demonstrating the efficient and reversible self-healing ability of the hydrogels.
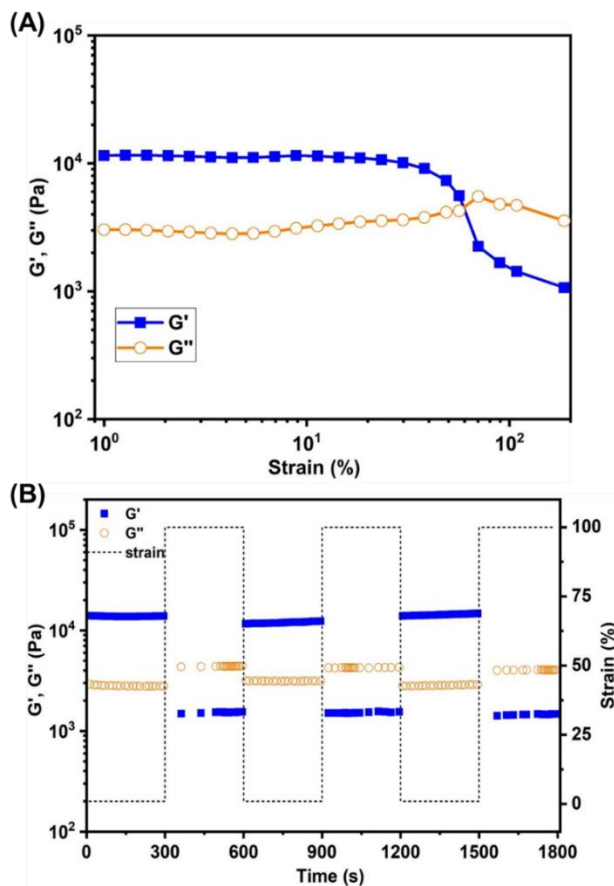
Figure 4.2.7. Dynamic rheology tests on hydrogel samples with 4 mg/mL SWCNTs. (A) Oscillation strain-sweep measurement over the strain region from 1% to 200%. (B) Cyclic strain step sweep tests from small strain ($\gamma = 1\%$) to large strain ($\gamma = 100\%$).

Aadditionally, cut-and-heal tests were conducted on the hydrogel samples to visually demonstrate its self-healing characteristics. As depicted in **Figure 4.2.8 (A)**, the as-formed hydrogel disk was cut into two pieces

and then placed into contact. These two hydrogel fragments were capable of supporting their weight after healing for 5 seconds at room temperature, and further integrated into one piece after 15 min, as it was evidenced by disappearance of damaged sits in the photography of **Figure 4.2.8 (A)**. Besides, the optical micro-images of the two hydrogel fragments were recorded after a 5 s and 5 min self-healing time, as listed in **Figure 4.2.8 (B).** Similarly, the damaged sites almost vanished after 5 min, further proving the fast self-repairing behavior of the hydrogel composites. Essentially, dynamic boronate ester bonds exposed at the damage interface could undergo decomposition to free boronic acid and diol groups, and the recombination of these two components drives the integration of the two separated fragments into one piece, which occurs spontaneously at room temperature in the absence of a catalyst.
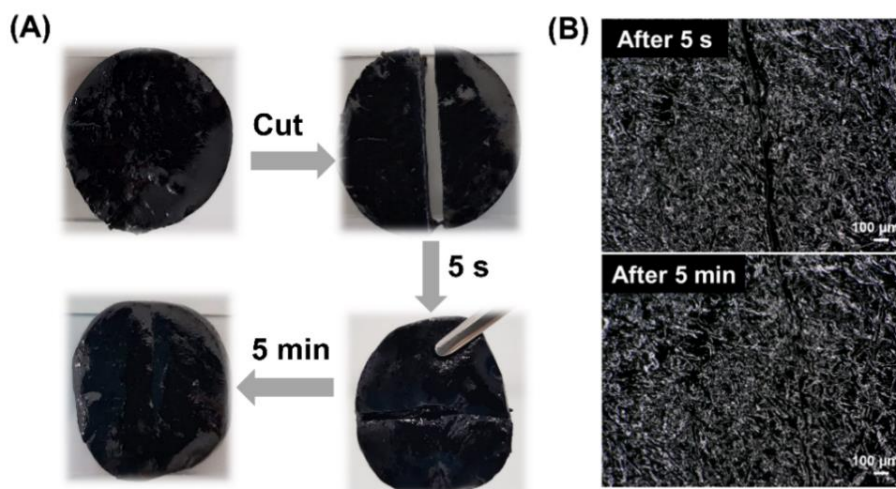
Figure 4.2.8. (A) Photographs showing the self-recovery process of the hydrogel sample. Briefly, the disk-shaped hydrogel. (B) The optical micro-images of the two hydrogel fragments were recorded after a 5 s and 5 min self-healing time.

4.2.4 Electrically conductive characterization of the hydrogel composites

Electrical conductivity of hydrogels with different concentration of SWCNTs was measured via four-point probe method (**Chapter 8.2.6**) and corresponding results were plotted in **Figure 4.2.9**. Pristine hydrogels,

i.e. no SWCNTs, exhibited a very low conductivity of 0.04 S/m, as a result of the conductive ions present in the system. Whereas, adding SWCNTs and gradually varying its concentration from 2 to 4, 6 and 8 mg/mL, was corresponding to an increase in conductivity from 0.30 to 0.65, 0.83 and 1.27 S/m, respectively, indicating the strengthened effect of SWCNTs on the hydrogels' conductivity.
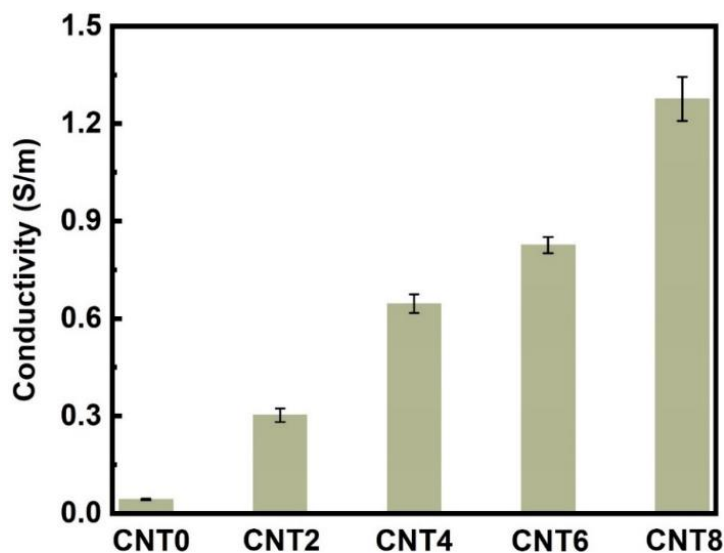
Figure 4.2.9. Electrical conductivity of different hydrogel samples with SWCNTs concentration of 0, 2, 4, 6, 8 mg/mL**.**

Except for the structural self-healing behavior as shown in Figure 4.2.8 (A), electrically self-healable ability of the conductive hydrogel composites shares the equal importance in regard to their practical application in biological electronics. To reveal the electrical self-healing behavior of the conductive hydrogels, another additional cut-and-heal test was conducted. As displayed in **Figure 4.2.10 (A),** the hydrogel sample was connected into a circuit as a conductor in series with a green LED indicator. Consequently, the LED was successfully lighted by an external voltage. On the contrary, once the hydrogel was cut into two pieces, the LED indicator was immediately switched-off in the open-circuit state (**Figure 4.2.10 (B)**). When the split pieces were connected together, the dynamic linkages on the damaged interfaces re-associated spontaneously, thus restoring the circuit to illuminate the LED again (**Figure 4.2.10 (C)**), revealing the success recovery in the electrical conductivity of the hydrogel sample.

Figure 4.2.10. Photographs showing the recovery process of electrical conductivity: (A) hydrogel sample was connected into a circuit powered by an external voltage; (B) hydrogel sample was cut into two separate pieces; (C) the two split pieces was put into contact.

Additionally, real-time electrical self-healing measurement was conducted based on the resistance change during the successive cut-and-heal process at the same cut site (procedure is shown in **Chapter 8.2.6**). As shown in **Figure 4.2.11 (A),** the electrical resistance exhibited relatively repetitive changes from stable values in a connected circuit to infinity under open-circuit state in ten cycles. Furthermore, the electrical self-healing efficiencies defined as the ratio between the recovered conductivity to the original conductivity were calculated, and the corresponding values are listed in **Figure 4.2.11 (B).** The average efficiency of the ten cyclic cut-and-heal process was 95% within about 10 seconds, revealing that the as-fabricated hydrogels possess repeatable and well efficient electrical self-healing characteristics.
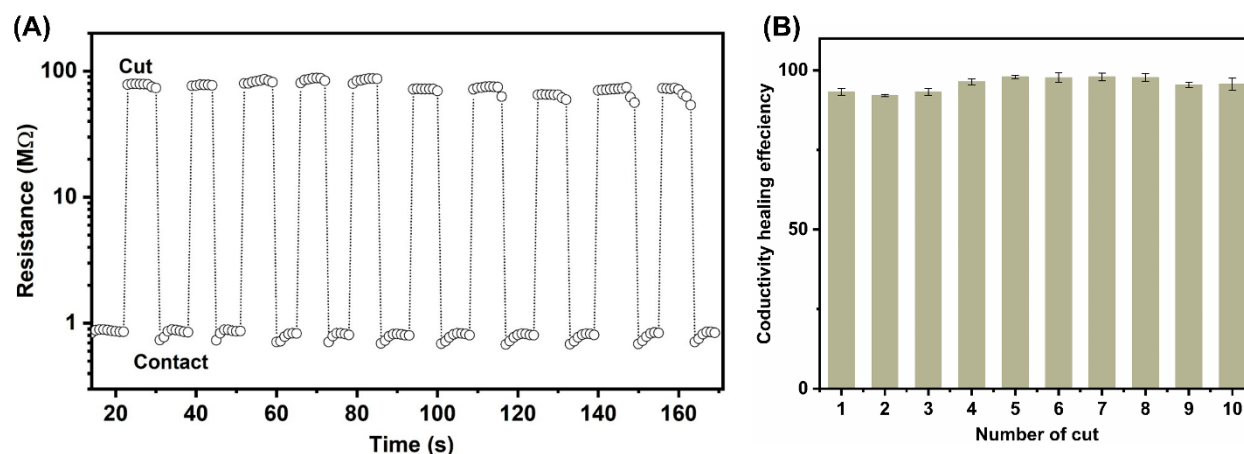
Figure 4.2.11. (A) Real-time electrical self-healing measurement in ten cut-and-heal cycles. (B) The corresponding electrical conductivity healing efficiency within ten cut-and heal cycles.

4.3 Summary

In summary, the fabrication of conductive and self-healable hydrogel composites was demonstrated, starting from a non-covalently cross-linked network based on host-guest and electrostatic interactions, and subsequently, transferring to a covalent network associated with boronate ester bonds. For noncovalent hydrogel, the π-π stacking interactions between pyrene groups and SWCNTs, as well as the host-guest interactions among cyclodextrin and adamantane moieties were first analyzed by UV-vis and 2D NOESY spectroscopy, respectively. Its physical and electrical self-healing abilities were further illustrated through a series of cut-and-heal tests. Subsequently, covalent cross-linked hydrogel was achieved based on SWCNTs, PVA and a functional copolymer P(DMA-*co*-APB-*co*-PBA) bearing pendant pyrene and phenylboronic acids derivatives. The SWCNTs were capable of evenly dispersing in aqueous solution via π-π stacking with pyrene groups of P2, and constructing the conductive channels for the hydrogels at the same time, while dynamic boronate ester bonds formed between the phenylboronic acids groups and PVA endowed the hydrogels with autonomous self-recovery ability without any external stimuli as determined by dynamic rheology tests. Besides, the covalent hydrogel also exhibited fast and repeatable electrical self-healing property (within 10 seconds) and a high recovery efficiency of 95 %. These conductive and self-healable hydrogels were envisioned to pave the road for potential applications in hydrogel-based biomedical fields, especially in tissue engineering, wound healing and electronic skins.

Dual-faced borax mediated synthesis towards self-healable hydrogels merging dynamic covalent bonding and micellization[§]
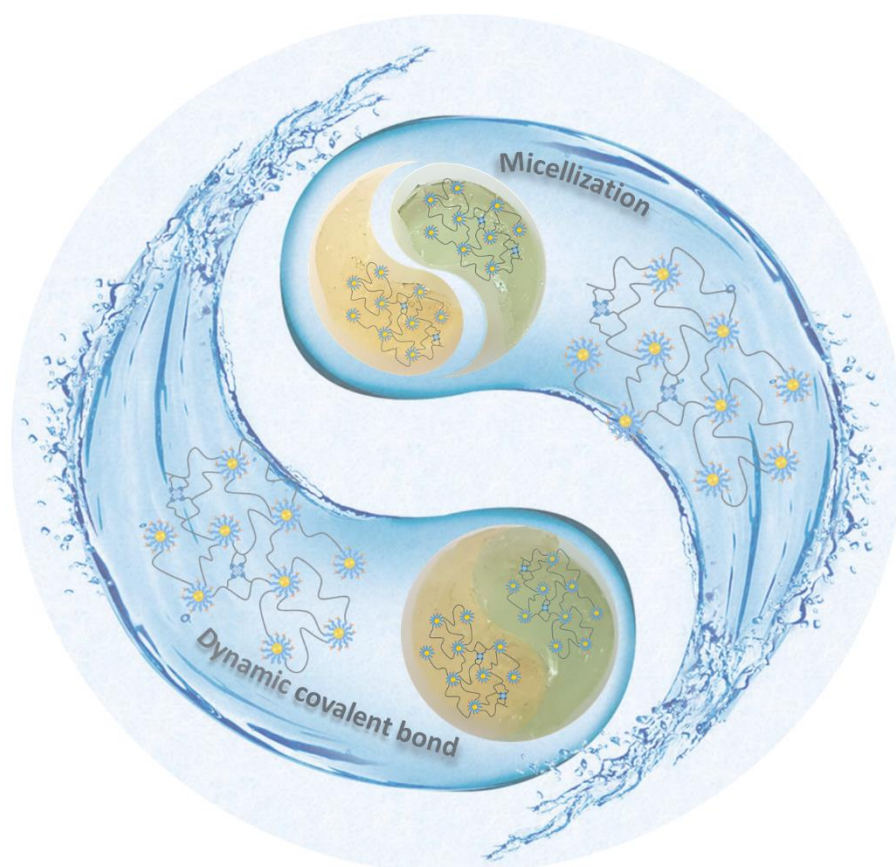
As previously mentioned, hydrogels are cross-linked soft materials consisting of physically or chemically cross-linked hydrophilic polymers that are swollen but not dissolved in large content of water.[204] In the regard of preparing the desirable hydrogels, thiol-ene click reactions,[185] including radical- and nucleophile-based click reactions and nucleophile/base catalyzed thiol-Michael addition reactions, are commonly utilized due to their distinctive merits, such as abundant ene- and thiol- related precursors, mild reaction conditions, tolerance to oxygen/water, and high yield and efficiency with minimal by-products when optimized.[186, 189] Initially, Hubbell and coworkers proposed a degradable hydrogel based on acrylate-functionalized and thiol-terminated polyethylene glycol (PEG) by the utilization of Michael-type addition reaction, and employed them as well-suitable biomaterials for controlled protein delivery.[217] Bowman and coworkers further engineered thiol-maleimide based hydrogels with pendent maleimide moieties as Diels-Alder reacting sites to control the release of peptide sequences.[218] Recently, a pioneering approach to prepare PEG-based hydrogels via a one-pot borax-catalyzed thiol-acrylate Michael polyaddition was developed. Borax, acting as the catalyst for polyaddition reaction between PEG diacrylate and dithiothreitol (DTT), was proved to exhibit an efficient catalytic ability comparable to phosphate buffer solution (PBS) at ambient temperature. Meanwhile, the dynamic boronate ester bonds formed spontaneously in reversible manner attributed to the complexation between borax and diol groups along DTT, imparting the final hydrogels with a self-healing ability and dual-responsiveness to temperature and pH.[219]

As already mentioned, hydrogels featuring an autonomous self-healing ability have gained considerable attention during the recent years due to their promising potentials in mimicking human skin which bear inherent self-healable nature. In general, hydrogels could be equipped with a self-healing ability by introducing dynamic and reversible bonds into the cross-linked systems. Nevertheless, it is still ongoing a challenge to fabricate self-healing hydrogels with excellent mechanical properties. Recently, this problem was addressed by integrating two or more physical and chemical dynamic bonds into one hydrogel system. For instance, Jeon and coworker designed an extremely stretchable hydrogel with rapid self-healing character via integrating multiple hydrogen bonds originating from 2-ureido-4-pyrimidone (UPy) dimers, hydrophobic association and encapsulation from sodium dodecyl sulfate (SDS) micelles, respectively. The as-fabricated hydrogels were capable of elongating up to 100 times of their original length and complete self-healing within 30 s.[220] By simply mixing aldehyde-functionalized Pluronic F127 with a three-armed acylhydrazine-terminated PEG, Wang and co-authors prepared an ultrastrechable and self-healing hydrogel based on dynamic acylhydrazone bonds in addition to dynamic micelle cross-linking. Their hydrogel could

be stretched up to 117 times of its initial length and displayed self-healing up to 85% of its original strength within 24 h.[221] While self-healing hydrogels based on dynamic boronate ester bonds have been intensively developed in recent years, the combination of dynamic boronate ester bonds with other dynamic physical bonds in one hydrogel system has been rarely investigated.

Accordingly, inspired by this work, this project was aimed at further exploring the possibility of fabricating self-healing hydrogels with two distinctive dynamic cross-link systems through one-pot borax catalyzed thiol-acrylate Michael addition reaction and borax-diol chemistry. To achieve this, a functional copolymer decorated with pendent acrylate and 1,2-diol groups was first synthesized through sequential reversible addition-fragmentation chain transfer (RAFT) polymerization and transesterification modification, followed by acidic hydrolysis of the protected 1,2-diols. Subsequently, borax catalyzed not only the thiol-ene reactions between the acrylate moieties and thiol functionalized Pluronic F-127 (PF127-SH), but also facilitated the formation of boronate ester bonds by complexing with 1,2-diols. An amphiphilic Pluronic F-127 (PF-127) was chosen as macro cross-linker due to its distinctive ability of self-assembling into micelles in aqueous solutions;[222, 223] and covalent polymerization of PF-127 micelles into hydrogel system has been proved to be a facile way to strengthen hydrogels' tensile and compressive properties.[224-226] Through this way, boronate ester bonds and PF127 micelles act as two kinds of dynamic cross-linking within one hydrogel system. The as-fabricated hydrogels are further investigated by evaluating the mechanical properties and self-healing ability.

5.1   Synthesis and characterization of functional copolymer

A functional random copolymer P(DMA-*co*-EDA-*co*-DHA) (P3) with pendent acrylate and 1,2-diol groups was synthesized via a combination of reversible additional-fragmentation chain transfer (RAFT) polymerization and sequential trans-esterification modification, followed by acidic deprotection, as illustrated in **Scheme 5.1**. First, a reactive parent copolymer P(DMA-*co*-PFPA) (P1) was prepared by copolymerization of *N*,*N*-dimethyl acrylamide (DMA) with pentafluorophenyl acrylate through RAFT copolymerization. DMA as a hydrophilic monomer is the major constituent part and hence endows P(DMA-*co*-PFPA) (P1) with good solubility in aqueous media.
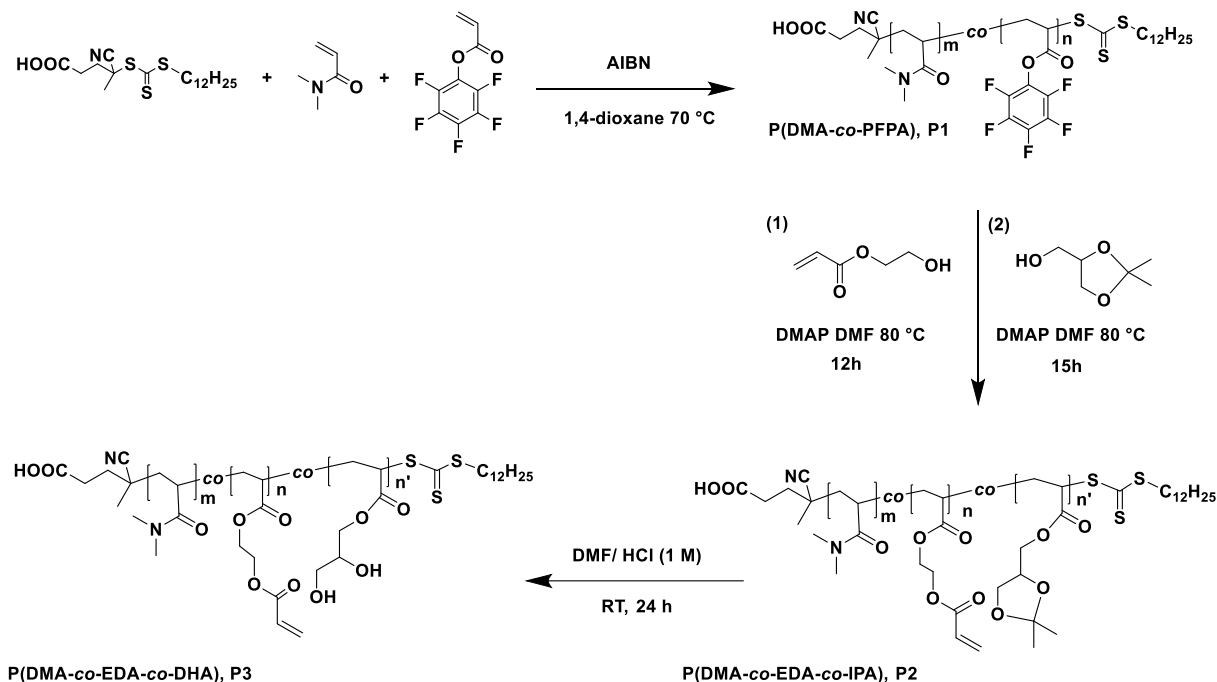
Scheme 5.1. The synthetic routes towards functional copolymer P(DMA-*co*-EDA-*co*-DHA), P3. First, P(DMA-*co*-PFPA), P1, was synthesized via RAFT polymerization, followed by a sequential trans-esterification modification to yield P(DMA-*co*-EDA-*co*-IPA), P2, and acidic deprotection thereof.

The ^{1}H-NMR and ^{19}F-NMR spectrum of P(DMA-*co*-PFPA) (P1) are shown in **Figure 5.1 (A)** and **Figure 5.2 (A)**, respectively. The ^{1}H-NMR spectrum displays the distinctive signals at 3.18–2.76 ppm originating from PDMA and PPFPA and the broad proton resonance signals at 2.0-1.0 ppm assigned to the backbone of the copolymer P(DMA-*co*-PFPA) (P1), while the ^{19}F-NMR spectrum shows the characteristic peaks at –152.54 ppm, –157.44 ppm, and –162.05 ppm attributed to PPFPA, thus demonstrating the successful synthesis of the desired precursor copolymer P(DMA-*co*-PFPA) (P1).

According to our previous reports, poly(pentafluorophenyl acrylate) featuring reactive pentafluorophenyl (PFP) ester groups is an effective handle to anchor primary alcohols to polyacrylate derivatives via 4-(dimethylamino) pyridine (DMAP) catalyzed trans-esterification modification.[227] Thus, P(DMA-*co*-EDA-*co*-IPA) (P2) was prepared by sequential substitution of PFP ester groups with 2-hydroxyethyl acrylate and isopropylideneglycerol, respectively. As determined by ^{1}H-NMR spectroscopy (**Figure 5.1 (B)**), the proton resonance signals of P(DMA-*co*-EDA-*co*-IPA) (P2) at 6.5–5.5 ppm were attributed to unsaturated

CH$_2$=CH– protons, while new broad peaks at 4.8–3.5 ppm corresponded to the solketal protons of isopropylideneglycerol and –O–CH$_2$–CH$_2$–O– protons of 2-hydroxyethyl acrylate. Besides, the integrals of proton signals at 5.85-5.75 ppm (k) and 4.68-3.50 ppm (l+l'+m+n+i) were calculated to determine the molar ratio of EDA and IPA of the obtained P(DMA-*co*-EDA-*co*-IPA) (P2), which was almost in agreement with the designated molar feeding ratio (**Figure C1 and Table C1, Appendix**), revealing the successful and well-controlled post-polymerization modification of P1 to yield P2. Furthermore, acetal protecting groups in isopropylideneglycerol could be easily removed via acidic hydrolysis, leaving pendent 1,2-diol groups along P(DMA-*co*-EDA-*co*-DHA) (P3) polymer chains, which was verified by the complete disappearance of methyl proton signals originating from isopropylideneglycerol at 1.32 ppm and 1.39 ppm in the ^{1}H-NMR spectra of P(DMA-*co*-EDA-*co*-DHA) (P3) (**Figure 5.1 (C)**).
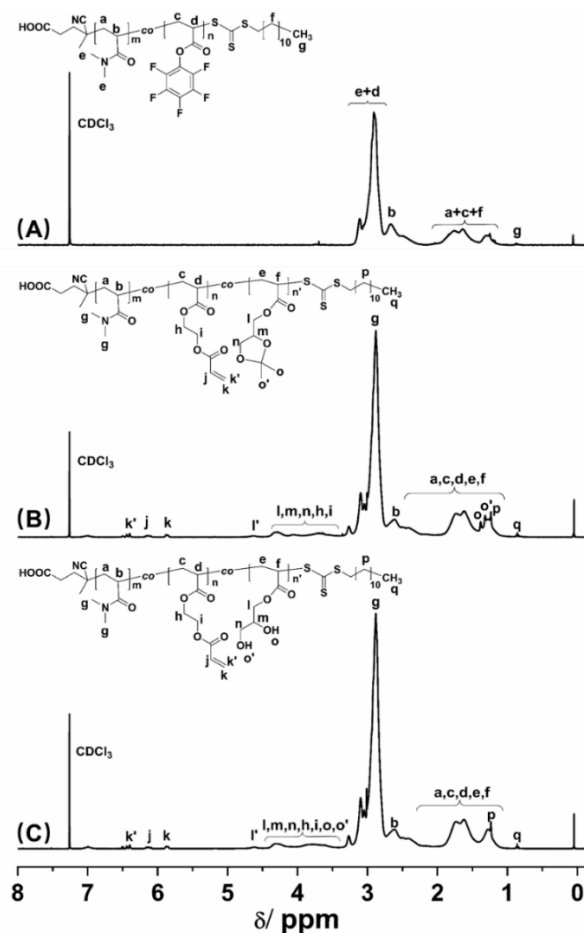
Figure 5.1. (A) ^{1}H-NMR spectra (400 MHz) of P(DMA-*co*-PFPA), P1; (B) P(DMA-*co*-EDA-*co*-IPA), P2; (C) P(DMA-*co*-EDA-*co*-DHA), P3; all spectra were recorded in CDCl$_3$ at ambient temperature.

The nucleophilic substitution process was also monitored by ^{19}F-NMR and FT-IR spectroscopy. As depicted in the ^{19}F-NMR spectrum of P(DMA-*co*-EDA-*co*-DHA) (P3) in **Figure 5.2 (A)**, compared to P(DMA-*co*-PFPA) (P1), the indicative pentafluorophenyl ester signals at (δ) –152.54 (*ortho*), –157.44 (*para*), –162.05 (*meta*) ppm completely disappeared after the trans-esterification process, revealing the successful modification. Besides, in the FT-IR spectrum (**Figure 5.2 (B)**) the characteristic pentafluorophenyl ester bands from PPFPA at 1780 cm^{-1} (C=O stretching vibration), 1520 cm^{-1} (aromatic –C$_6$F$_5$ stretching vibration), and 990 cm^{-1} (C-F stretching bond) also disappeared after the substitution process. Furthermore, a new C=O stretching vibration band at 1720 cm^{-1} and a broader band at 3433 cm^{-1} were clearly identified, which were attributed to the new formed ester C=O and 1, 2-diol groups, further demonstrating the success of ester exchange.
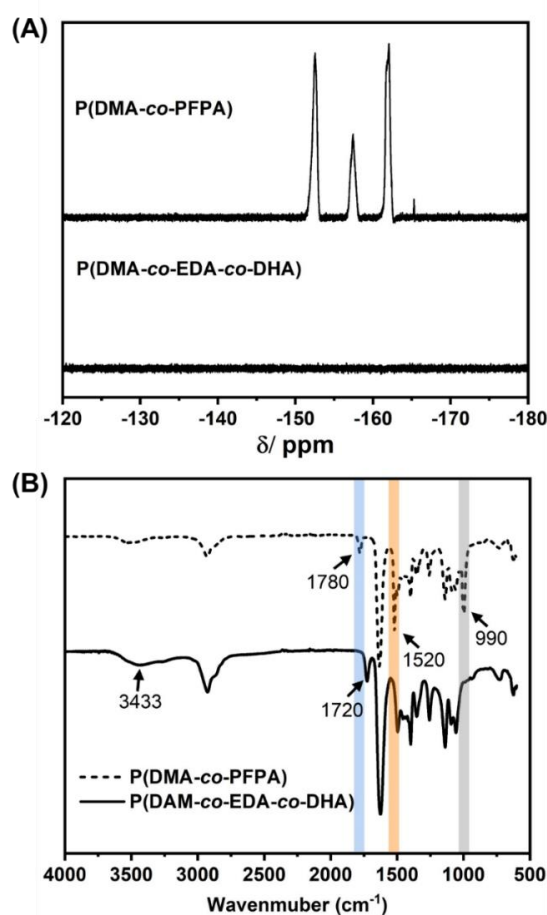
Figure 5.2. (A) ^{19}F-NMR spectra (376 MHz) of P(DMA-*co*-PFPA), P1 and P(DMA-*co*-EDA-*co*-DHA), P3 in CDCl$_3$; (B) FT-IR spectra of P(DMA-*co*-PFPA), P1 and P(DMA-*co*-EDA-*co*-DHA), P3.

5.2 Characterization of dual-faced borax mediated synthesis

As the thiol-based precursor for click reaction, thiol-terminated Pluronic F127 (PF127-SH) was first synthesized through esterification reaction, and adequately characterized by ^{1}H-NMR and FT-IR spectroscopy (**Chapter 8.3.13, Figure C2 and C3 in Appendix**). By affirming the integrals ratio of methyl protons at 1.08 ppm originating from poly(propylene oxide) (PPO) moieties to the characteristic signals of 3-mercaptopropionic acid at 2.62 ppm, the ratio of thiol functionality was estimated to be around 86%.
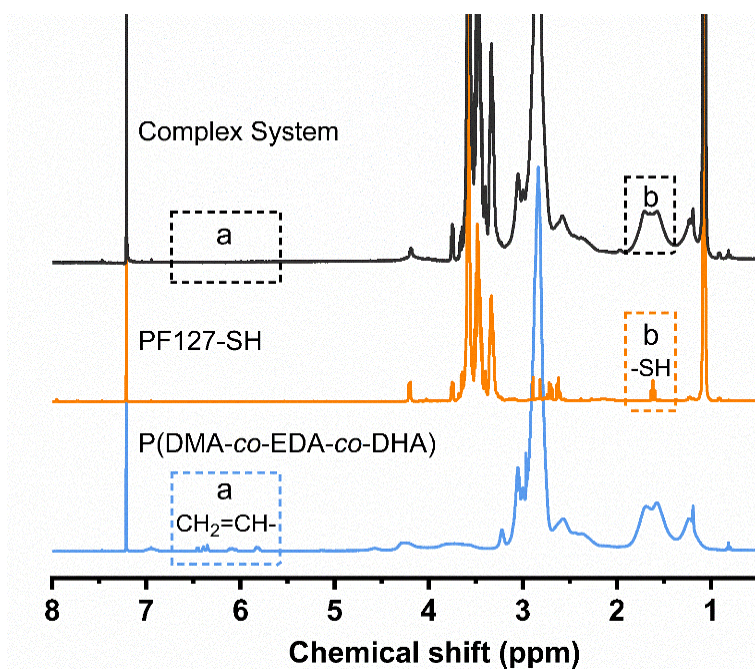
Figure 5.3. ^{1}H-NMR (400 MHz) of P(DMA-*co*-EDA-*co*-DHA) (P3, bottom blue line), PF127-SH (middle yellow line), and the mixture of P(DMA-*co*-EDA-*co*-DHA) (P3), PF127-SH and borax solution in CDCl$_3$ (upper black line).

Noteworthy, borax is known to be an efficient catalyst for thiol-acrylate Michael addition reaction,[219] as well as being a reagent to form dynamic boronate ester bonds with *cis*-diols (either 1,2- or 1,3-).[228] First, prior to any hydrogel formation, a reaction of P(DMA-*co*-EDA-*co*-DHA) (P3) with PF127-SH in dilute solution was conducted resulting in presumably highly branched but soluble polymers, which allowed a subsequent characterization. The catalytic effect of borax on the thiol-ene reaction between P(DMA-*co*-EDA-*co*-DHA) (P3) and PF127-SH was confirmed by ^{1}H-NMR spectroscopy. As shown in **Figure 5.3**,

multiple proton resonance signals at 6.5-5.5 ppm assigned to $CH_2=CH-$ of pendent acrylate groups, as well as the peak at 1.67 ppm attributed to thiol groups from PF127-SH, completely disappeared in the highly branched polymer after 30 minutes of reaction time, demonstrating that borax was indeed an effective catalyst for the thiol-acrylate Michael addition reaction.

Meanwhile, ^{11}B-NMR spectra of P(DMA-*co*-EDA-*co*-DHA) (P3) / borax mixture in deuterated water at different pH values of pH = 3 and pH = 9, respectively, were recorded to further indicate the diol/borax complexation involved in the reaction. As illustrated in **Figure 5.4**, ^{11}B-NMR spectra at pH 9 exhibited a broad and predominated peak at 16.9 ppm arising from the monoborate $B(OH)_4^-$ species, as well as a shoulder peak at around 13.2-6.9 ppm, which was attributed to 2:1 complex between the pendent diols group and tetrahedral boron center. When the pH value was adjusted to 3 by the addition of HCl solution, the above mentioned peaks totally disappeared and a new boron resonance signal at 19.5 ppm appeared with higher intensity, demonstrating that the complexation structures completely disassembled and borax consequently existed in free $B(OH)_3$ form under the specified acidic conditions.
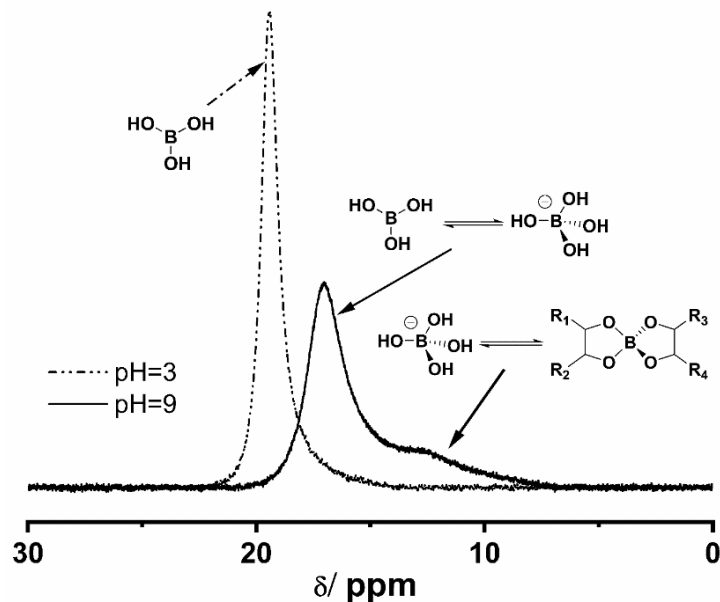
Figure 5.4. ^{11}B-NMR (128 MHz) spectra of the mixture of P(DMA-co-EDA-co-DHA), P3 with borax solution under pH=3 (dash dotted line) and pH=9 (solid line) in D_2O (polymer concentration: 50 mg/mL, molar ratio of borax/diol= 1:4).

5.3   Fabrication and characterization of the hydrogels
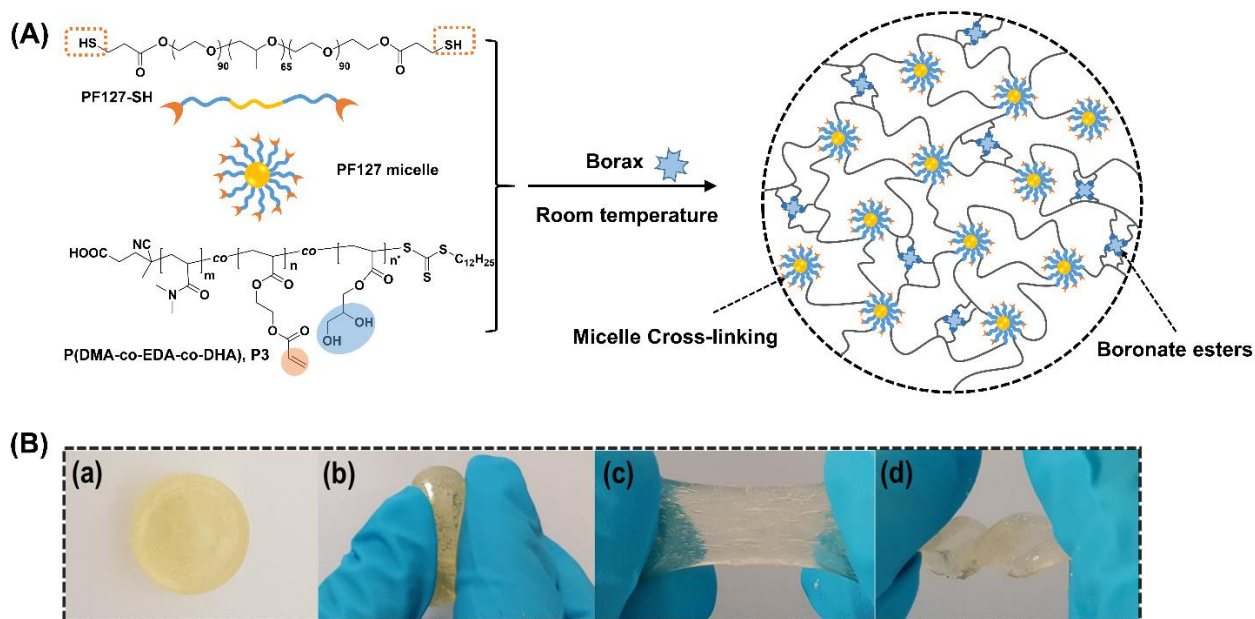
Figure 5.5. (A) Schematic illustration depicting the formation of the hydrogels by mixing as-synthesized P(DMA-*co*-EDA-*co*-DHA) (P3), PF127-SH and borax solution at ambient temperature; (B) Photographs showing the hydrogel under different deformations: original (a), compressed (b), stretched (c) and twisted (d).

By simply mixing P(DMA-*co*-EDA-*co*-DHA) (P3), PF127-SH with borax solution, a hydrogel formation was observed within several minutes, and the detailed procedure, formulations and gelation time were listed in **Chapter 8.4.5** and **Table C1-C2 in Appendix.** The gelation mechanism involving the two reactions is illustrated in **Figure 5.5 (A)**. Briefly, driven by the hydrophobic PPO block, thiol-terminated amphiphilic triblock copolymers Pluronic F127 (PEO$_{99}$-PPO$_{65}$-PEO$_{99}$, PF127) self-assembled into micelles in water, which in turn served as macro cross-linkers to connect the flexible P(DMA-*co*-EDA-*co*-DHA) (P3) chains during the gelation process. Once borax was added to the mixed solution of P(DMA-*co*-EDA-*co*-DHA) (P3) and Pluronic F127-SH, thiolether bonds and tetrahedral boronate ester bonds were formed simultaneously via the thiol-acrylate Michael addition reactions and borax-diol complexations, respectively, thus merging two distinguishable systems, i.e. dynamic micelles cross-linking and dynamic boronate ester bonds, in the

same hydrogel system. It has to be noted that the as-fabricated hydrogel could be compressed, stretched and twisted without any fracture as shown in **Figure 5.5 (B)**. Since higher concentration of diol groups was critical for designing self-healable hydrogels, the characterizations of hydrogel specimens containing P(DMA-*co*-EDA-*co*-DHA) (P3) with designated molar ratio of EDA / DHA =30 : 70 was focused, which was a suitable ratio for gelation while bearing the maximum content of diol groups (**Table C2, Appendix**). Unless otherwise stated, the following measurements were performed with these specific specimens.
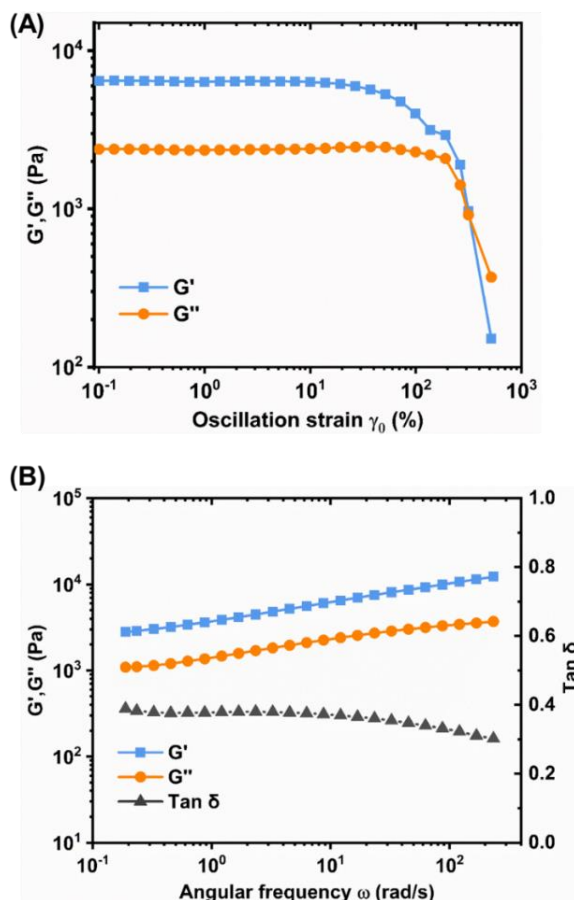
Figure 5.6. (A) Oscillation strain-sweep measurement over the strain region from $\gamma_0 = 0.1\%$ to 500%; (B) Frequency sweep measurements of hydrogels over the region from 0.1 to 300 rad/s.

To further analyze the mechanical properties of the formed hydrogel, a cylindrical sample with diameter of 28 mm and thickness of 4 mm was prepared, and tested on a ARES-G2 rheometer. First, oscillation amplitude sweeps were performed with strain range from $\gamma_0 = 0.1\%$ to 500% to determine the linear viscoelastic region of the hydrogel at ambient temperature. As shown in **Figure 5.6 (A)**, the storage modulus

(i.e. elastic moduli G') and loss modulus (i.e. viscous moduli G'') remained constant as the strain varied from $\gamma_0 = 0.1\%$ to 80 %, indicating that the hydrogel could endure the deformation at ambient temperature. While the strain continued to increase, both G' and G'' tend to decrease until a crossover point occurred at $\gamma_0 = 320\%$ strain, where the hydrogel network was disrupted entering the nonlinear regime. Next, frequency sweeps were conducted under constant $\gamma_0 = 0.1\%$ strain, as shown in **Figure 5.6 (B)**, and both storage modulus G' and loss modulus G'' showed a weak frequency-dependent behavior as the characteristic response for viscoelastic materials increasing from 3 kPa to 10 kPa and 1 kPa to 3 kPa, respectively. The storage modulus G' remained larger than the loss modulus G'' over the entire frequency region, demonstrating its free-standing dominated elastic state. Besides, the corresponding loss tangent tan δ = G''/G', which was used to quantify the extent of viscous contributions in the material, displayed a value between 0.4 and 0.3, thus further demonstrating the stable gel-like state.
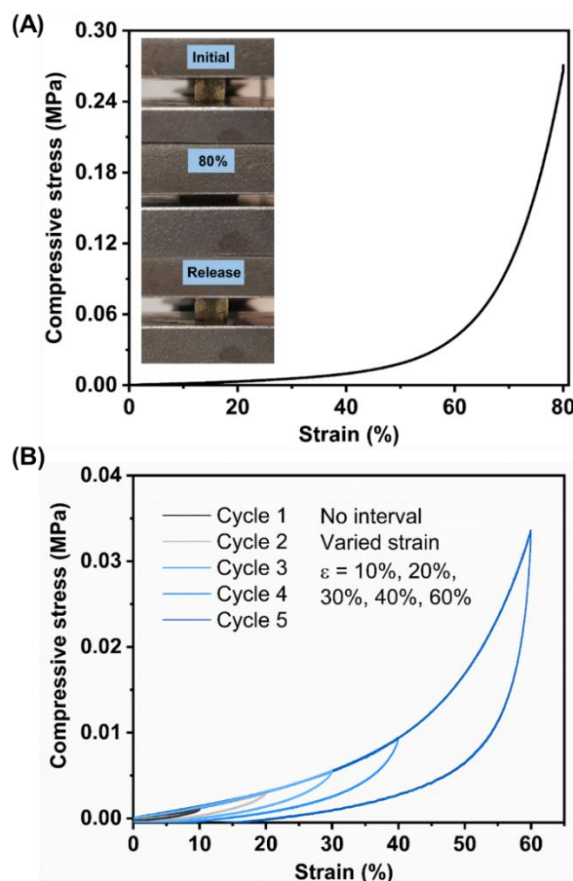
Figure 5.7. Compression tests of the prepared hydrogel. (A) Compressive stress-strain curves; (B) Sequential loading-unloading tests without interval under varied strain of 10%, 20%, 30%, 40% and 60%, respectively.

Compressive and tensile tests were consecutively performed to characterize the fracture resistance of the as-fabricated hydrogel. As shown in **Figure 5.7 (A)**, the hydrogel could endure a uniaxial compression up to 80 % strain without breaking and recover to its original shape after releasing the load, indicating a good self-recovery property. Besides, cyclic loading-unloading tests under varied compression strains of 10%, 20%, 30%, 40% and 60%, respectively, were performed without intervals to investigate the hydrogel's energy dissipation behavior. Generally, energy dissipation is illustrated as hysteresis loops in the consecutive loading-unloading cycles, and the corresponding area of a hysteresis loop was used to measure the dissipated energy per unit volume.[229] As shown in **Figure 5.7 (B)**, the hysteresis loop areas increased with intensified compress strain and pronounced hysteresis loops are displayed once the compressive strain exceeded 30%, demonstrating the efficient energy dissipation during large strain deformation.
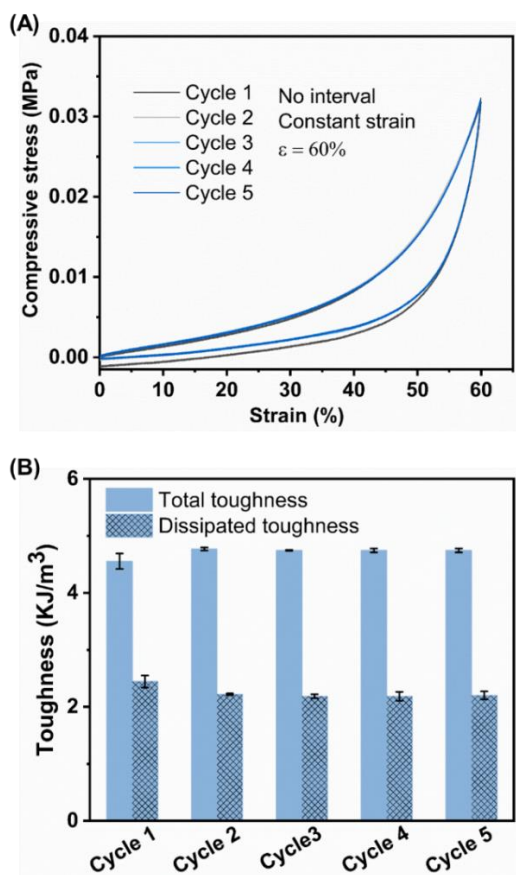
Figure 5.8. Compression tests of the prepared hydrogel. (A) Consecutive loading-unloading tests without interval under a constant strain of 60%; (B) Corresponding total and dissipated toughness calculated from graph (A).

Besides, anti-fatigue character of the hydrogel was further investigated through another five cyclic loading-unloading tests under a constant strain of 60% without any interval, thus the corresponding total and dissipated toughness were listed in Figure 5.8. As shown in **Figure 5.8 (A)**, essentially all cyclic curves overlapped with each other and the toughness strength exhibited minimal changes during the last four cycles. The dissipated energy decreased only slightly from first cycle to second cycle, and then remained practically constant for the last four cycles, indicating an outstanding fatigue resistance property (**Figure 5.8 (B)**). Furthermore, the hydrogel could be stretched up to 340% and the elongated sample could almost recover its original length after 30 minutes after unloading (**Figure 5.10 and Figure C4 in Appendix**). Generally, to dissipate energy upon loading the dynamic character of PF127 micelles could undergo chains slides and disentanglements. The corresponding rearrangements and recombination of the polymer chains under unloading drove also the recovery of deformation. Therefore, the covalent incorporation of PF127 micelles into the hydrogel endowed it with a stretchability, and outstanding and fatigue resistance characteristic.

To illustrate the self-healing behavior of the hydrogel, first qualitative cut-and-heal tests were conducted. As shown in **Figure 5.9**, disk-shaped hydrogel samples were prepared and one sample was colored with dye to facilitate an optical contrast in the self-healing experiments. The samples were cut with a razor blade into pieces and then placed back together with the cut surfaces of opposite colored hydrogel samples to allow for a self-recovering process at ambient temperature. The cut vanished and nearly became invisible after 24 h, and the hydrogel can be stretched (**Figure 5.9 (a)-(d)**), revealing its self-healing ability.
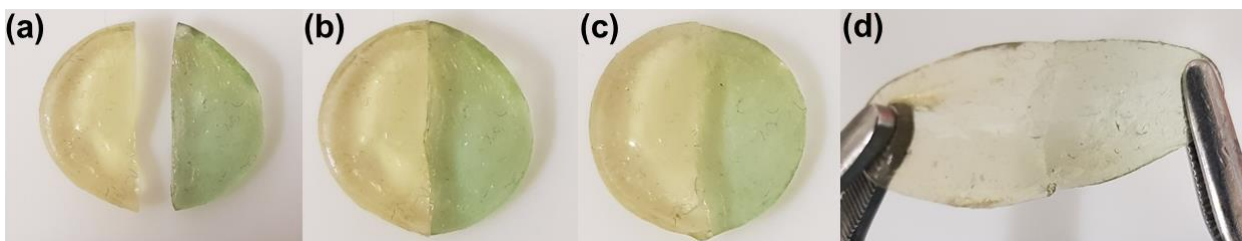
Figure 5.9. Photographs showing the cut-and-heal tests of the hydrogel: (a) disk-shaped samples with and without dye were prepared and cut into pieces; (b) two pieces were put into contact; (c) self-healing for 24 h; (d) stretching after 24 h.

Furthermore, the self-healing efficiency of the hydrogels was quantitatively determined by tensile tests. As depicted in **Figure 5.10**, compared to the original sample, the healed sample exhibited a slightly larger stress at the beginning of deformation due to the inevitable water evaporation after self-healing for 24 h, but gradually showed lower stress with the increase of elongation, and finally fractured with approximately 20.8 KPa stress at 320% strain. Compared to the fracture stress of the original sample, which occurred at 23.1 KPa, the self-healing efficiency, defined as ratio of the fracture stress between the healed and original samples, was estimated to be 90% after a 24 h self-healing time. In comparison, the self-healing efficiency of as-fabricated hydrogel was comparable to dynamic acylhydrazone cross-linked poly(ethylene oxide)/PF127 hydrogel (87% within 24 h)[221] and was relatively higher than the complexation systems between boric acid and random copolymer bearing hydroxyl groups (~70% within 24 h)[230]. Additionally, similar cut-and-heal tests were performed on P2-based hydrogels and the two fragments failed to integrate into one piece after 24 h (**Figure C5, Appendix**). Therefore, the self-healing behavior of the hydrogel was mainly attributed to the reversible covalent boronate ester bonding between borax and 1,2-diol groups, which could reform at the damaged interface to repair the separated network. Compared to PF127 micelles based single network (such as the P2-based hydrogel in our present work and other hydrogels in the reported literatures[224, 226]), the double dynamic network obviously united the merits of two distinguishable systems, i.e. dynamic boronate ester bonds and micellization to accomplish multifunctional hydrogels with excellent mechanical properties as well as good self-healing property.
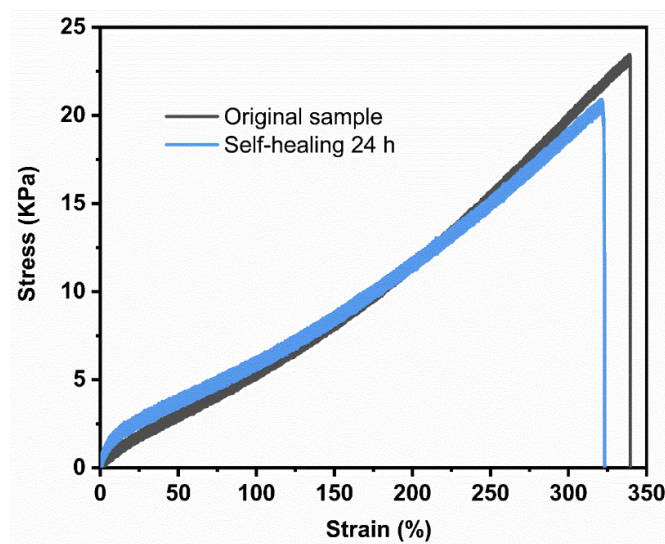
Figure 5.10. Tensile stress-strain curves of the original hydrogels and hydrogels after self-healing for 24 h.

5.4   Summary

To conclude, an autonomously self-healable hydrogel was proposed, which was based on a one-pot borax catalyzed thiol-acrylate Michael addition reaction and borax-diol chemistry. By simply mixing as-synthesized P(DMA-*co*-EDA-*co*-DHA) (P3), thiol-terminated PF127 and borax solution, two distinguishable systems, i.e. dynamic micelles cross-links and boronate ester bonds, were successfully incorporated into one hydrogel. The fracture and recombination of PF127-SH micelles upon loading-unloading process endowed the hydrogel with outstanding shape-recovery and fatigue resistance, as well as the moderate stretchability. Besides, the hydrogels were capable of self-healing up to 90% in 24 h due to the spontaneous association of dynamic boronate ester bonds at the damage interface. Generally, the results illustrated a facile way to fabricate self-healable hydrogels with excellent mechanical properties, and it is postulated that the present hydrogels might have versatile applications in biological tissue engineering fields, considering the superior biocompatibility of Pluronic F-127 as well as the low toxicity of catalyst borax.

Two in one: Fusion of dynamic boronic ester bonds via *para*-fluoro-thiol reaction towards malleable and self-healable heteroatom-rich covalent polymer networks[**]

In regard to the covalent dynamic motifs amenable to the manufacture of vitrimers, exchangeable boronic esters garnered considerable interest due to their unique thermodynamic stability and structural tunability as reported by the group of Guan.[128] Crucially, the addition of *N*-donor ligands (e.g. *ortho*-amino,[128] organic base triethylamine,[129] pyridine and imidazole derivatives[231]) accelerate the exchange the kinetics of dynamic B-O bonds due to the B-N dative interactions, while improving their hydrolytic stability in healable and reprocessable networks.[129, 232, 233]

Thus far, a plethora of dynamic polymeric networks based on boronic ester bonds has been described, while the majority of them involved the synthesis the functional (co)polymers bearing diol or boronic acids groups,[128, 234] with only one partial exception employing a photo-initiated thiol-ene reaction for the direct preparation of dynamic networks.[126, 127] Quite recently, the *para*-fluoro-thiol reaction (PFTR) as a thiol-based click reaction has received substantial research interest for post-polymerization modification, polymeric structure construction, surface functionalization, as well as cross-linked network fabrication.[170, 191, 192, 235] Organic superbases have found widespread use as organocatalysts in a variety of thiol-based organic syntheses by their virtue of high basicity and stability, low nucleophilicity and low toxicity.[236] Specifically, some nitrogen-containing amidine and guanidine bases, such as 1,8-diazabizyclo[5.4.0]undec-7-ene (DBU), 1,5,7-triaza-bicyclo-[4.4.0]dec-5-ene (TBD), and 1,5-diazabicyclo[4.3.0]non-5-ene (DBN), possess strong basic properties (pK_a values 24.3, 26.0 and 23.8 in acetonitrile,[237] respectively) and consequently can accelerate reactions with lower catalyst loading and reaction time. Accordingly, they were found to be a more efficient catalyst for PFTR than commonly utilized trimethylamine (TEA, pK_a value 18.8 in acetonitrile[237]).[238-240]

In this chapter, the *para*-fluoro-thiol reaction (PFTR) was exploited to pave a facile avenue to directly transform small organic molecules into a boronic ester based dynamic networks (**Scheme 1**). Prior to the polymeric network construction, a model reaction between a mono-functional pentafluorophenyl derivate and a dithiol-functionalized boronate ester was conducted to gain insight into the PFTR ligation chemistry under different catalytic superbases (e.g. DBU, TBD and DBN), while avoiding the analytical challenges originating from the insolubility of the networks. The optimized reaction conditions were then transferred to the formation of dynamic covalent networks. For this, a novel linker bearing three-armed pentafluorophenyl moieties (3PFB) was reacted with dithiol-functionalized boronate ester, yielding cross-linked networks with rich atomic elements (i.e. C, O, S, F, B and N) via PFTR ligation chemistry. Last but not least, the thermodynamic behaviour

of the polymeric network, as well as its malleability and self-healing ability were investigated in-detail.

6.1   The model reaction via PFTR
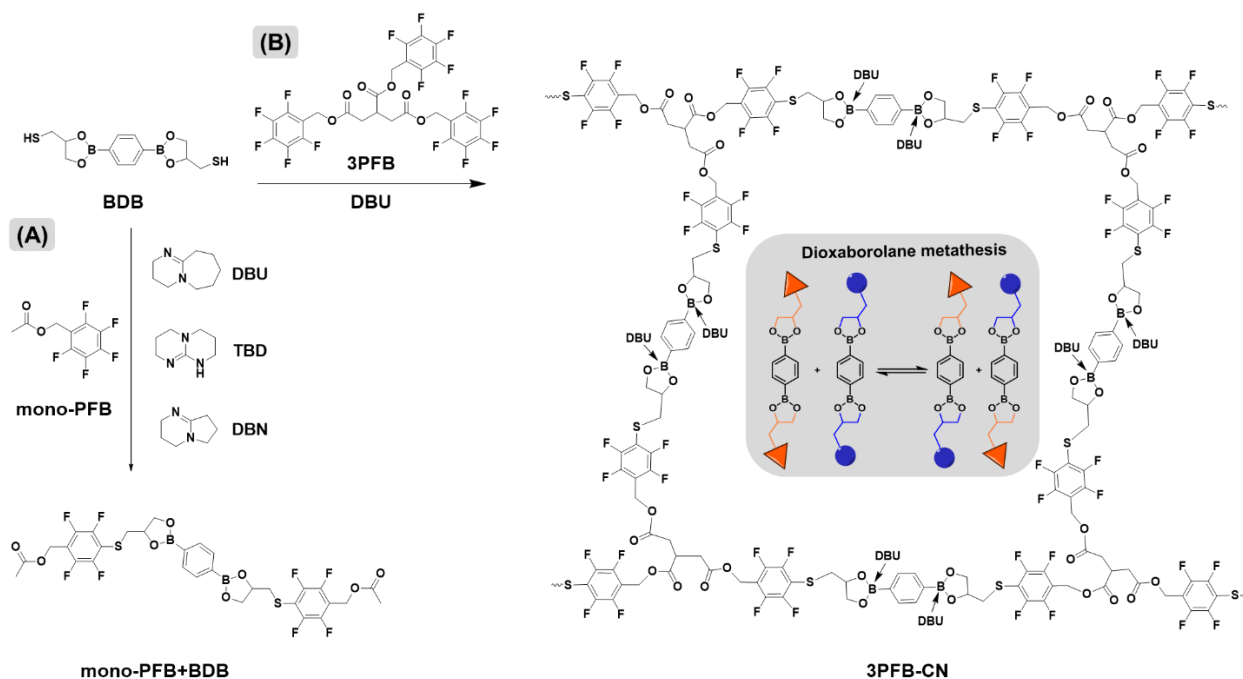
Scheme 6.1. (A) Model PFTR between a mono-functional pentafluorophenyl derivate (mono-PFB) and a dithiol-functionalized boronate ester (BDB) in the presence of different superbases (e.g. DBU, TBD and DBN). (B) Schematic illustration of the construction of polymer network by reacting a novel three-armed pentafluorophenyl derivate (3PFB) with BDB via DBU-catalyzed PFTR. In the inset, the illustration of dynamic exchange of boronic ester bonds, also called dioxaborolane metathesis, is depicted.

In order to avoid analytical challenges associated with the insolubility of polymer networks, a model reaction was first employed to mimic the covalent bonds of the targeted polymer network. As shown in **Scheme 6.1 (A)**, the model PFTR between a mono-functional pentafluorophenyl derivate (mono-

PFB) and a dithiol-functionalized boronate ester (BDB) in the presence of a superbase was investigated. With the goal of optimizing the PFTR to make it amenable for a polymer network formation, three superbases, i.e. 1, 8- diazabicyclo[5.4.0]undec-7-ene (DBU), 1,5,7-triaza-bicyclo-[4.4.0]dec-5-ene (TBD) and 1,5-diazabicyclo[4.3.0]non-5-ene (DBN), were exploited and their effect on the ligation chemistry was studied.

The model reaction was conducted first with DBU as the base due to its known catalytic efficiency in PFTR reactions.[238, 239] **Figure 6.1** shows the ^{19}F-NMR spectra of the unreacted mono-PFB and the product after reaction of mono-PFB with BDB for 20 min via DBU-catalyzed PFTR (molar ratio of thiol : PFB : DBU=1 : 1.1 : 1.1). The mono-PFB precursor exhibited the indicative signals at δ = -142 ppm, -153 ppm, and -162 ppm, which were assigned to the *ortho-*, *para-* and *meta-*fluorine atoms of PFB, respectively. The reaction of mono-PFB with BDB resulted in the decrease of *para-*fluorine signals at -153 ppm, while concomitantly the *ortho-* and *meta-*fluorine signals of the product were shifted to -137 ppm and -146 ppm, respectively. The corresponding substitution ratio was calculated to be 85%, which was close to its theoretical ratio of 90.9% (**Figure D1**, **Appendix**).
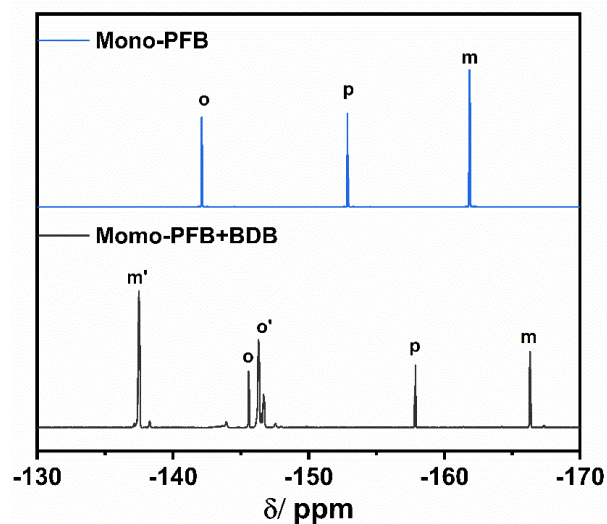
Figure 6.1. Comparative ^{19}F-NMR (377 MHz, in THF-d_8) of mono-PFB and the crude reaction mixture upon the reaction with (BDB) for 20 min in the presence of 34.3 mol-% DBU.

Consequently, the ^{19}F-NMR spectra could evidence that the DBU-catalyzed PFTR proceeded fast with high efficiency while involving only substitution of the *para-*fluorine atoms. Additionally, this nucleophilic

substitution was also monitored by FT-IR spectroscopy, with the results shown in **Figure 6.2**. After the PFTR took place, a more intensive band at 1645 cm^{-1} appeared attributed to the stretching of S=C bond in the typical resonance forms when aromatic ring directly connects to an electronic rich atom (i.e. S, O), and an obvious shift of the C=C aromatic vibration from $v(C_6F_5)$ =1500 cm^{-1} to $v(C_6F_4S)$ =1470 cm^{-1} was also detectable, which was in accordance with the change of the aromatic substitution pattern,[241] both demonstrating the successful ligation.
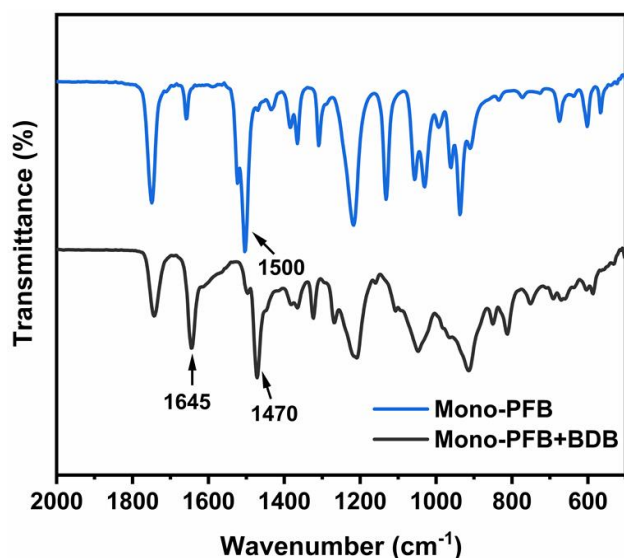
Figure 6.2. Comparative FT-IR spectra of mono-PFB and the crude reaction mixture upon the reaction with BDB for 20 min in the presence of 34.3 mol-% DBU.

Additionally, other superbases, i.e. TBD and DBN, were also exploited in order to reveal their impact on the model reaction under the same experimental conditions. However, both TBD and DBN resulted in precipitation of a yellow gel during the model PFTR. The fact that a gelation was observed was likely an indication of some side reactions by substitution of the *ortho-* and *meta-* fluorine atoms, which was further manifested by ^{1}H-NMR and ^{19}F-NMR spectra compared to that of a DBU-catalyzed PFTR, as shown in **Figure D2 and Figure D3** (Appendix). The presence of side reactions resulted in imperfections during the synthesis, which would inevitably affect the homogeneity when it comes to the construction of polymer networks. Accordingly, DBU was chosen as the most appropriate catalytic superbase for the following investigations.
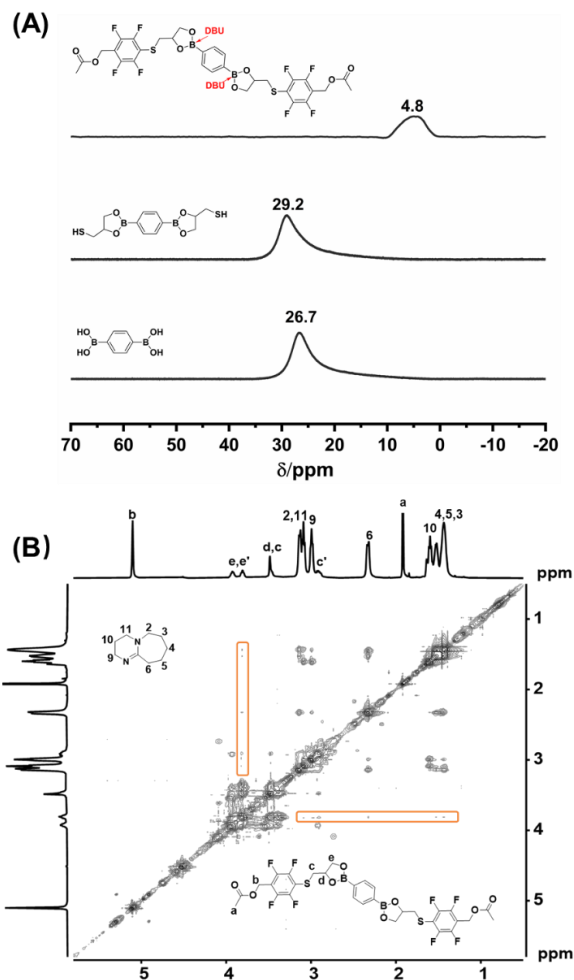
Figure 6.3. (A) ^{11}B-NMR spectra (128 MHz) of mono-PFB+BDB (top), BDB (middle) and 1,4-phenylenediboronic acid (bottom) in THF-d_8. (B) 2D NOESY spectrum (298 K) of mono-PFB with BDB upon DBU-catalyzed PFTR in THF-d_8.

Since DBU is a nitrogen-containing superbase, it was postulated that besides acting as an efficient PFTR catalyst, DBU can also coordinate with the boron center to form tetrahedral boronic ester bonds via B-N dative interactions.[242] To identify the latter, ^{11}B-NMR spectroscopy was first performed, as shown in **Figure 6.3 (A)**. Both 1,4-phenylenediboronic acid and bifunctional thiol BDB exhibited a single peak in the ^{11}B-NMR spectrum at 26.7 and 29.2 ppm, respectively, which can be assigned to the trigonal sp^2 boron centers. After the DBU-catalyzed PFTR, this signal of the trigonal sp^2 boron center fully disappeared and instead a new resonance peak at 4.8 ppm occurred, which was consistent with a tetrahedral sp^3 boron center via the B-N dative bonding.[242, 243] Further insight into the presence of B-N dative interactions was obtained from 2D NOESY analysis. The spectrum in **Figure 6.3 (B)** shows that there was detectable cross-

resonance at 3.8 ppm (orange box) arising from the anticipated ^{1}H-^{1}H interactions between the protons adjacent to the boron center and the DBU protons, further demonstrating the existence covalent B-N interactions after the DBU-catalyzed PFTR of mono-PFB with BDB.

6.2 Synthesis and characterization of the polymeric networks

After the detailed insight into the model PFTR, these optimized reaction conditions were then transferred to the formation of dynamic covalent networks. First, a three-arm linker (3PFB) was synthesized and subsequently reacted with BDB in the presence of DBU as the base, as illustrated in **Scheme 6.1 (B)**.
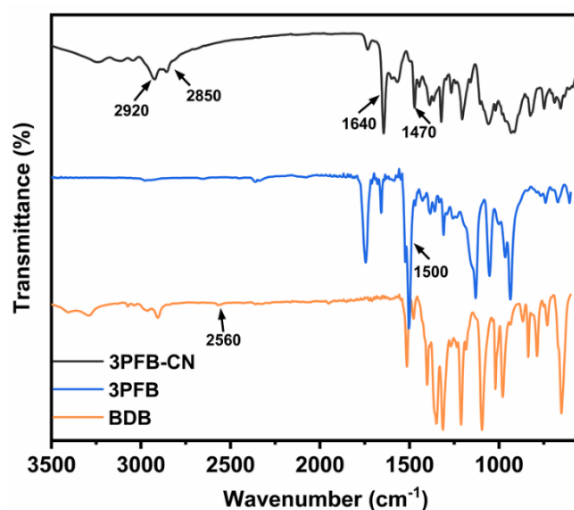
Figure 6.4. FT-IR spectrum of cross-linked network 3PFB-CN (black line), 3PFB linker (blue line) and bifunctional thiol BDB (yellow line);

According to the investigations on the model PFTR, DBU was able to play two important roles during the nucleophilic substitution reaction: (1) DBU as a strong organic base facilitated the deprotonation of thiol groups during the PFTR and hence accelerating the reaction; (2) DBU as a Lewis base was also capable of coordinating with the Lewis acid, i.e. boronic esters, thus forming a tetrahedral sp^3-hydridized boron center. To identify the successful nucleophilic substitution reactions during the PFTR network formation, FT-IR analysis was performed and the results are shown in **Figure 6.4**. As known from FT-IR spectra of the model reaction, the indicative thiol stretching band at 2560 cm^{-1} was only visible in the BDB spectrum, and not in

the spectrum of the crosslinked network (3PFB-CN). Instead, bands at 3040 cm^{-1}, 2920 - 2850 cm^{-1} were detected in the spectrum of 3PFB-CN, which corresponded to the C-H stretching of the aromatic rings and aliphatic chains, respectively. Besides, the band at 1640 cm^{-1} was attributed to the aromatic S=C stretching bond in resonance forms, and the shift of aromatic C-C stretching band from $v(C_6F_5) = 1500$ cm^{-1} to $v(C_6F_4S)$ $= 1470$ cm^{-1} was also observed, indicating the successful reaction as well as the incorporation of dynamic boronic ester bonds into the cross-linked network via thiol-based PFTR.

In addition, a ^{19}F-NMR spectrum of the network was recorded, after it was fully swollen in CDCl$_3$ prior to the measurement. As shown in **Figure 6.5**, compared to original 3PFB ^{19}F-NMR spectrum, the signals of *para*-fluorine atoms disappeared and only signals of *ortho*- and *meta*- fluorine atoms remained, which in turn were shifted after the PFTR, thus again revealed the high efficiency and regioselectivity of PFTR involving only the *para*-fluorine atoms.
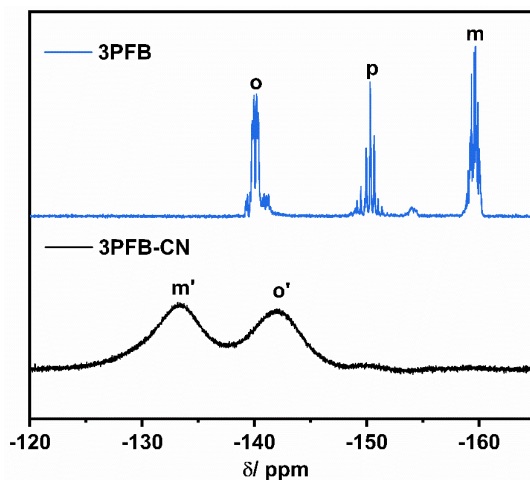
Figure 6.5. Gel ^{19}F-NMR spectra (58 MHz) of 3PFB (top) and 3PFB-CN polymeric network (bottom) in CDCl$_3$.

Crucially, the polymeric network 3PFB-CN facilely obtained by PFTR was featured with heteroatom-rich character (i.e. C, O, S, F, B and N), and among them, B and O atoms imparted 3PFB-CN with dynamic bond motifs due to the successful incorporation of boronic ester bonds, which can undergo a reversible dioxaborolane metathesis at elevated temperatures. As a typical feature of dynamic covalent networks, the stress from deformation can be easily released at relatively high temperature through internal exchange reactions of dynamic cross-links.[244]

Therefore, the dynamic behavior of the as-fabricated polymeric network was characterized by stress relaxation analysis. As shown in **Figure 6.6 (A)**, the dynamic polymeric network was able to relax the stress completely (< 1% of the initial stress) within 100 s. The characteristic relaxation time (τ), which was defined as the time required to relax to 1/e (ca. 36.8%) of the initial stress, gradually decreased with increasing temperature from 60 to 80 °C, demonstrating a faster relaxation behavior at higher temperature. The 3PFB-CN featured with rich heteroatoms displayed much faster characteristic relaxation time (τ) (within 1s) compared to that of simple boronic ester based networks (normally within a few minutes even at higher temperature[245, 246]). We postulate its fast relaxation behaviors arise to the high content of B and O atoms in the form of boronic esters, along with its heteroatom-rich environment.
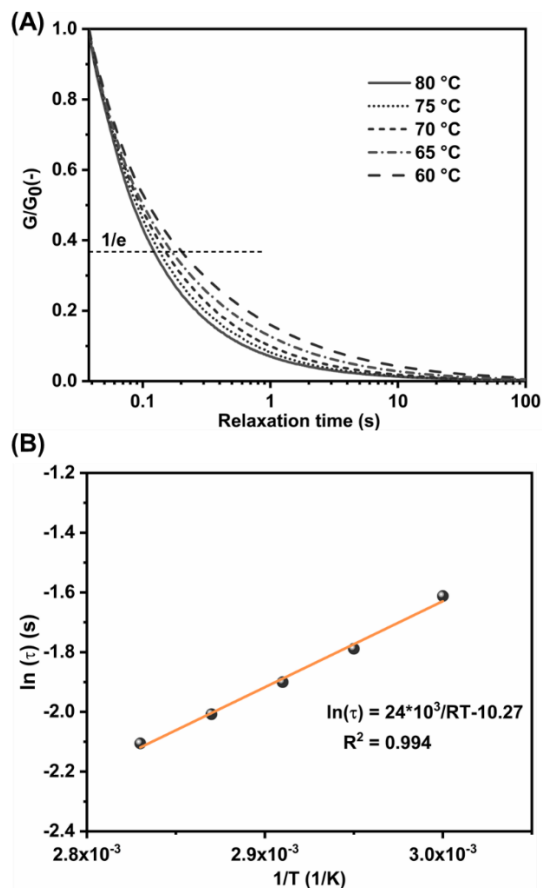
Figure 6.6. (A) Normalized stress relaxation curves of the network to study the dynamic behavior of 3PFB-CN polymeric network (from 13 mm plate-plate geometry at strain of 0.5-2% within the linear viscoelastic regime). (B) Plots of ln (τ) against 1/T and a linear fit to calculate the activation energy ($E_a \sim 24$ kJ/mol).

Additionally, the temperature-dependent relaxation arising from internal dynamic cross-links can be described by an Arrhenius model,

$$\tau(T) = \tau_0 exp\left(\frac{E_a}{RT}\right) \tag{1}$$

where τ_0 is the Arrhenius prefactor and E_a is the activation energy for viscous flow. From the plot of the relaxation time ($\ln(\tau)$) against the inverse temperature ($1/T$), a linear correlation was obtained as shown in **Figure 6.6 (B)**. The activation energy E_a of the relaxation process was calculated to be 24 kJ/mol, which is slightly higher than reported values measured for the small molecule boronic ester exchange reaction (15.9 kJ/mol)[53] and simple boronic ester based networks (7.7-13.8 kJ/mol)[245]. This might be attributed to the diffusion-limiting topology associated with the cross-linked network environment, as well as the heteroatom-rich structure of the network, but is nevertheless within typical activation energies for polymer melts.

The dynamic nature of the 3PFB-CN network associated with the high content of B and O atoms in the form of boronic esters, as well as the coordinated N atoms originating form DBU base, also enabled a good reprocessability and self-healing ability. Prior to investigating these possibilities, the glass transition temperature (T_g) of the 3PFB-CN was determined by DSC analysis to be around 21 °C (see **Figure 6.7 (A)**). This relatively low T_g facilitates a reprocessability, as shown in **Figure 6.7 (B)**. For this, the 3PFB-CN sample was first cut into pieces or grinded into a power at ambient temperature, which then could be easily reshaped into transparent films at 60 °C under 10 MPa within 10 min. These conditions were sufficient to enable a spontaneous dioxaborolane metathesis among internal boronic ester bonds (as shown in **Scheme 6.1 (B)**). Crucially, the dynamic network also exhibited a good solvent resistance, since it did not dissolve but only swell in common organic solvents, such as THF, DCM, acetone or DMF, as shown in **Figure D4 (Appendix)**. Its good solvent resistance is partially attributed to the incorporated S and F atoms, which have been reported to exhibit inherent chemical resistance.[247, 248] However, the polymer network decomposed in THF in the presence of glycerol, which was ascribed to the fast exchange reactions between boronic esters and the excess diol groups provided by glycerol.
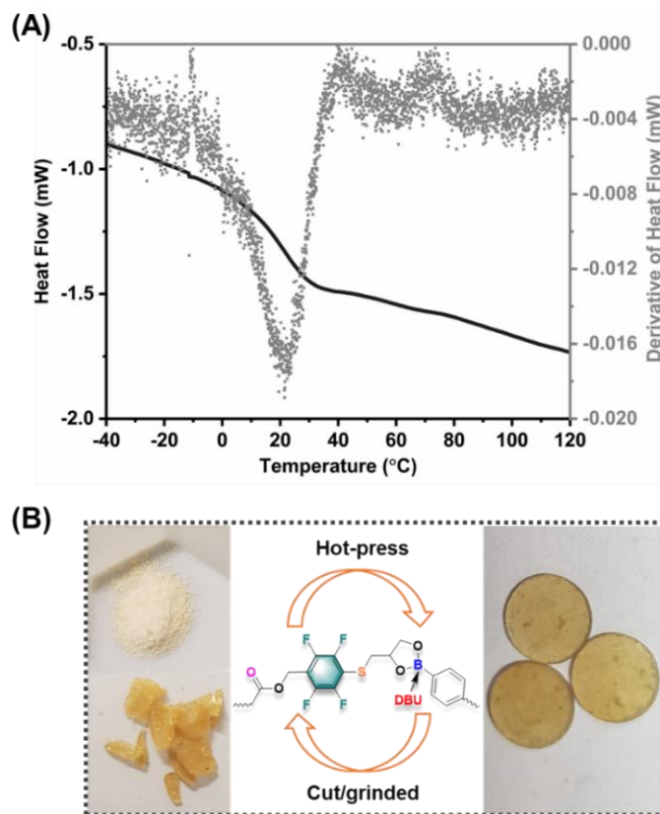
Figure 6.7. (A) DSC analysis of the 3PFB-CN network to determine the T_g of the 3PFB-CN polymeric network. (B) Photographs showing the reprocessability of the 3PFB-CN network.

Except for the direct dioxaborolane metathesis, the exchange of boronic esters could be also achieved via hydrolysis and re-esterification in the presence of water, thus facilitating a self-healing behavior of the 3PFB-CN network. The possible mechanism for the water-triggered self-healing behavior is illustrated in **Figure 6.8 (A) and (B)**. The addition of water to the freshly cleaved surfaces induced the hydrolysis of boronic esters, leaving some free boronic acids and diols exposed on the fracture surface. When placed into contact with each other at elevated temperature (i.e. above T_g to increase the chain mobility), the surface-exposed boronic acids and diols can associate again via a re-condensation reaction. Notably, the dynamic boronic esters within 3PFB-CN polymeric network were in tetrahedral configurations, as evidenced in **Figure 6.3**, which normally show a higher rate of association over disassociation under wet conditions compared to the trigonal counterparts.[129] Consequently, tetrahedral boronic esters with continual reversibility impart the 3PFB-CN polymeric network with relatively fast self-healing behavior in the presence of water.

Therefore, the self-healing ability of 3PFB-CN polymeric network was further qualitatively explored. As shown in **Figure 6.8 (C)**, the disk-shaped sample was first cut into two pieces and dabbed with water at the fracture interfaces, followed by being placed into contact. After 1h at 60 °C, the two separated parts were successfully integrated into one piece as evidenced by the thorough disappearance of the original scar.
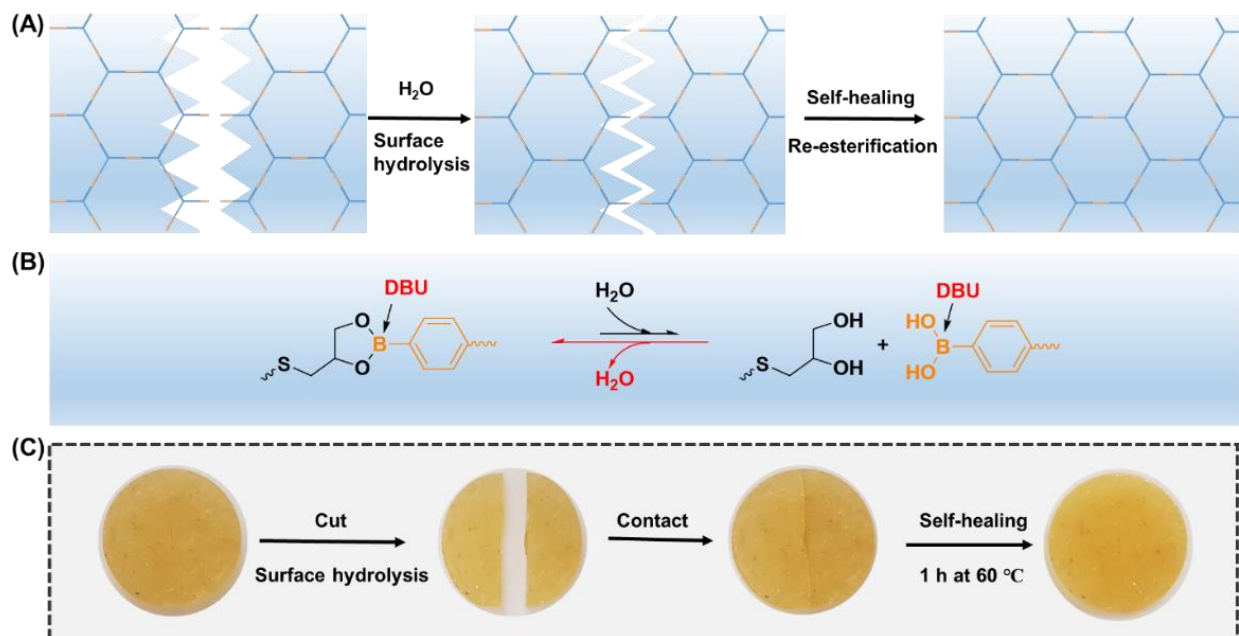
Figure 6.8. Self-healing behavior of 3PFB-CN polymeric network. (A) Proposed mechanism of healing according to the shift of equilibrium as illustrated in (B); (C) Photographs showing the self-healing process.

6.3   Summary

In summary, a new facile method was proposed to prepare a malleable, reprocessable and self-healable covalent network based on dynamic boronic ester bonds using *para*-fluoro-thiol click reaction (PFTR). The model reaction revealed the dual roles of DBU during the PFTR ligation chemistry, which can act as a catalyst to initiate PFTR with high efficiency and regioselectivity while coordinating with boron centers via boron-nitrogen dative interactions. The unique heteroatom-rich character endowed 3PFB-CN polymeric network with good solvent resistance,

rapid stress relaxation (below 1% of original stress within 100 s), and could be reprocessed easily within 10 min at 60 °C. Meanwhile, the 3PFB-CN network showed accelerated self-healing performance with the aid of water due to the sp^3-hybridized boronic ester bonds associated with boron-nitrogen coordination. With the merged merits of facile synthesis, heteroatom-rich character, easy reprocessability and fast self-healing properties, it was envisioned that the novel polymeric network can be a new platform for the development of dynamic materials, as well as one-pot polymerization of heteroatom-rich materials, by the use of the unique chemistry of PFTR ligation.

7. Conclusion and outlook

The fascinating and emerging properties of dynamic polymer networks based on reversible bonds have boosted their widespread applications in the real world, especially in the area of adaptable biomedical materials and malleable thermosets. In this dissertation, studies towards the implementations of both reversible non-covalent bonds (i.e. host-and-guest and electrostatic interactions) and covalent bonds (i.e. boronic ester bonds) to the design of dynamic functional networks were presented. As a primary step, delicately designed protocols, with the combination of controlled living polymerization (like RAFT and ATRP) and facile post-polymerization modification (such as active ester modification and *para*-fluoro-thiol reaction), were proposed to synthesize the targeting functional copolymers, which served as the fundamental materials for further developed dynamically cross-linked networks.

Dual-functionalized hydrogels with both self-healable and conductive properties were first presented, involving both dynamically noncovalent and covalent networks. The former, non-covalent cross-linked hydrogel was formed by integrating Py-*β*-CD modified SWCNTs, polycations ((PAMPT)) and polyanions (PNaSS). The π-π stacking interactions between pyrene groups and SWCNTs, as well as the host-guest interactions between cyclodextrin and adamantane moieties were analyzed by UV-vis and 2D NOESY spectroscopy, respectively. Its physical and electrical self-healing abilities were manifested through a series of cut-and-heal tests. The later, covalent cross-linked hydrogel was achieved based on SWCNTs, PVA and a functional copolymer P(DMA-*co*-APB-*co*-PBA) bearing pendant pyrene and phenylboronic acids derivatives. Within the cross-linked system, evenly dispersed SWCNTs built the conducting channels for the network, while tetrahedral boronate ester bonds were formed through reversible complexation between the phenylboronic acids and adjacent diol groups along PVA chains, therefore endowing the hydrogel with autonomous self-healing ability without any external stimuli. The covalent hydrogel exhibited bulk conductivity (1.27 S/m with 8 mg/mL SWCNTs) with a fast and autonomous self-healing ability that restored 95 % of its original conductivity within 10 s under ambient conditions. Accordingly, due to its outstanding properties, it was postulated to be a good potential candidate to be applied in hydrogel-based biomedical fields, especially in tissue engineering, wound healing and electronic skins**.**

The subsequent chapter of this thesis introduced another autonomously self-healable hydrogel based on a one-pot borax catalyzed thiol-acrylate Michael addition reaction and borax-diol chemistry. Herein, by simply mixing a functional copolymer P(DMA-*co*-EDA-*co*-DHA) decorated with pendent acrylate and 1,2-diol groups, thiol-terminated Pluronic F127 (PF127) and borax solution, two distinguishable systems, i.e.

dynamic micelles cross-links and boronate ester bonds, were successfully incorporated into one hydrogel system. The as-fabricated hydrogel displayed outstanding shape-recovery, fatigue resistance and moderate stretchability (up to 340%), which was attributed to the reversible fracture / recombination behaviors of PF127-SH micelles upon loading-unloading process. Additionally, dynamic boronate ester bonds imparted the hydrogel with a self-healing ability and its healing efficiency was up to 90% within 24 h as evaluated by tensile tests. This work significantly broadened the application of borax-catalyzed chemistry in dynamic networks, and might have versatile applications in biological tissue engineering fields, considering the superior biocompatibility of Pluronic F-127 as well as the low toxicity of catalyst borax.

Beside the above mentioned hydrogel systems, dynamically cross-linked system imbedded with exchangeable boronic ester bonds was also amenable to bulk polymeric network. Accordingly, in chapter 5, a new facile method was proposed to prepare a malleable, reprocessable and self-healable covalent network based on dynamic boronic ester bonds using *para*-fluoro-thiol click reaction (PFTR). The model reaction revealed the dual-roles of superbase DBU, which could act as a catalyst to initiate PFTR with high efficiency and regioselectivity while coordinating with boron centers via boron-nitrogen dative interactions. Additionally, the as-fabricated polymeric network displayed good solvent resistance, fast relaxation (below 1% within 100 s), fast self-healing properties with the aid of water (within 1 h at 60 °C), and could be repeatedly reprocessed within 10 min at 60 °C. This work was envisioned to be new platform for the development of dynamic materials by the use PFTR chemistry.

In summary, versatile possibilities of preparing dynamic functional networks with reversible bonds are presented in this thesis, from hydrogel systems to bulk polymeric network by using currently available controlled polymerizations and post-polymerization modification methods. The strategies undertaken in this thesis are envisioned to broaden the customized applications of dynamic networks in both biological engineering and recyclable plastics areas.

Nevertheless, there still exists enormous challenges in front of us regarding the full understanding of dynamically cross-linked network, since the theoretical frameworks and characterization techniques on all the dynamic motif are still insufficient. Especially for self-healing measurements, current studies are only limited to the macroscopic analysis on their bulk mechanical changes before and after damage, and how to reveal and further assess their self-healing ability on molecular level still remains a challenge. Besides, new strategies should be put forward to install the dynamic bonds into existing commodity products to truly improve their service life. As a result, continuous research in dynamic networks is still a prerequisite to make them more amenable to industrial manufacturing.

8. Experimental section

8.1 Materials

β-Cyclodextrin (*β*-CD, >98%, TCI), *p*-toluenesulfonyl chloride (TsCl, >98%, Sigma-Aldrich), ethylendiamin (EDA, 99%, ACROS OrganicsTM), *N,N'*-dicyclohexylcarbodiimid (DCC, 99%, Sigma-Aldrich), 1-hydroxybenzotriazol hydrate (HOBt, 97%, Sigma-Aldrich), 1-adamantanol (99%, Sigma-Aldrich), 2-bromoisobutyryl bromide (98%, Sigma-Aldrich), sodium hydroxide (NaOH, 99%, Roth), copper(I)-bromide (CuBr, 99.999%, Alfa Aesar), *N,N,N',N'',N''*-pentamethyldiethylenetriamine (PMDETA, 99%, Sigma-Aldrich), ammonium persulfate (98%, Sigma-Aldrich), *N,N,N',N'*-tetramethylethylenediamine (TMEDA, 98%, Alfa Aesar) and sodium 4-vinylbenzenesulfonate (NaSS, 90%, Sigma-Aldrich) were used as received. (3-Acrylamidopropyl) trimethylammonium chloride solution (AMPTMA, 75 wt% in H_2O, Sigma-Aldrich) was purified by passing through a basic aluminium column prior to polymerization.

N,N-Dimethyl acrylamide (DMA, 99%, Sigma-Aldrich) was purified by passing through a basic aluminium column before polymerization, 2,2'-azobis(2-methylpropionitrile) (AIBN, 98%, Sigma-Aldrich) was recrystallized from methanol before polymerization. 2,3,4,5,6-Pentafluorophenol (99%, Sigma-Aldrich), 2,6-lutidine (98%, Sigma-Aldrich), acryloyl chloride (96%, Alfa Aesar), 4-cyano-4-[(dodecylsulfanylthiocarbonyl) sulfanyl] pentanoic acid (CDTPA, 97%, TCI), 1-pyrenebutyric acid (97%, Sigma-Aldrich), pentafluorophenyl trifluoroacetate (98%, Sigma-Aldrich), 1,6-hexamethylenediamine (98%, Sigma-Aldrich), (4-aminomethylphenyl) boronic acid hydrochloride (98%, abcr), poly(vinyl alcohol) (PVA, 98%, TCI, M_w~88,000 g/mol), trimethylamine (TEA) were used as received. Ultra-pure water was obtained from GenPure Pro™ (Thermo scientific). SWCNTs were supplied from OCSiAl Europe and heated in air at 500 °C for 30 minutes to remove amorphous carbon material before use.

2- Hydroxyethyl acrylate (HEA, 95%, TCI), isopropylideneglycerol (IPG, 97%, Sigma-Aldrich), 4-(dimethylamino) pyridine (DMAP, 97%, Sigma-Aldrich), Pluronic F-127 (PF127, bioreagent, Sigma-Aldrich), 3-mercaptopropionic acid (99%, Sigma-Aldrich), *p*-toluenesulfonic acid monohydrate (98.5%, Sigma-Aldrich), dithiothreitol (DTT, bioreagent, Fisher scientific), borax (97%, Sigma-Aldrich),

hydrochloric acid (HCl, 37 wt%, Sigma-Aldrich). 1,4-Phenylenediboronic acid (96%, abcr), 1-thioglycerol (90%, Alfa Aesar), acetic acid (99%, ROTH), tricarballylic acid (99%, Sigma Aldrich), 2,3,4,5,6-pentafluorobenzyl bromide (97%, Acros Organics), potassium carbonate (K_2CO_3, 99%, Sigma Aldrich), cesium carbonate (99.5%, Acros Organics), magnesium sulfate ($MgSO_4$, 99%, ROTH), 1, 8-diazabicyclo[5.4.0]undec-7-ene (DBU, 98%, Sigma Aldrich), 1,5,7-triaza-bicyclo-[4.4.0]dec-5-ene (TBD, 98%, Sigma Aldrich), 1,5-diazabicyclo[4.3.0]non-5-ene (DBN, 98%, Sigma Aldrich) were used as received.

8.2   The characterization techniques

8.2.1   Nuclear magnetic resonance (NMR) spectroscopy

Nuclear magnetic resonance (NMR) spectroscopy is an effective and non-destructive technique to analyze the molecular structure at atomic level. When the nucleus of certain atom is immersed into a strong static magnetic field, it will undergo the procession movement, and once exposed to an electromagnetic irradiation with the same frequency as the procession one, the nuclear magnetic resonance (NMR) phenomenon occurred. The absorbed energy required to be in resonance produces a radiofrequency signal which is further recorded by a radiofrequency receiver, converted into NMR spectra by using mathematical Fourier transform. Nuclear magnetic resonance spectroscopy makes the use of NMR phenomenon to identify the chemical structures of the materials. Normally, certain nuclei with inherent spin properties, such as ^{1}H, ^{13}C, ^{19}F, ^{15}N, ^{11}B and ^{31}P, exhibit NMR effect and are commonly explored in NMR spectroscopy.[249]

In this work, all ^{1}H-NMR, ^{19}F-NMR and ^{11}B-NMR measurements were recorded on a Bruker Avance 400 spectrometer at 298 K (400 MHz for ^{1}H, 376 MHz for ^{19}F and 128 MHz for ^{11}B). Tetramethylsilane (TMS) was used as internal standard for ^{1}H-NMR. All the samples were dissolved in deuterated solvent prior to the measurement. The NOESY NMR spectra were recorded on a Bruker Avance 600 MHz spectrometer. The gel ^{19}F-NMR measurement (Chapter 5) was recorded on a Magritek Spinsolve 60 spectrometer (58 MHz for ^{19}F-NMR), the polymeric network was first synthesized in THF, dried under vacuum oven and then re-swollen into CDCl$_3$ solvent prior to the measurement.

8.2.2 Gel permeation Chromatography (GPC)

Gel permeation chromatography (GPC), which is also called as size exclusion chromatography (SEC), is a versatile analytical technique to characterize the polymer samples' molecular weights and molecular weight distributions. It consists of the stationary phase (small porous beads), the mobile phase (eluent solvent), the columns, the pumps as well as the detectors. The polymer sample was first dissolved into the eluent solvent and then injected into the columns by the pumps. As flowing through the columns with the eluent solvent, large sized polymer chains (above the biggest size of porous beads) will be directly excluded from the pores without penetrating into the stationary phase, while smaller sized polymers will pass through the interior of the porous beads partially or wholly. Therefore, the polymer sample was spontaneously separated based on their sizes with the flow of mobile phase, and the corresponding retention time was recorded in a chromatogram, which will be further utilized to determine the molecular weight and dispersity by comparing to the calibration curve of a certain polymer standard (normally polystyrene or poly(methyl methacrylate)).

In this work, GPC measurements were performed using Polymer Laboratories (Varian) PL-GPC 50 Plus Integrated System equipped with two PL gel 5 m Mixed-Columns (300 × 7.5 mm). DMAc were used as the eluent solvent. The polymer samples were first dissolved into DMAc with a concentration of 2 mg/mL and then filtered to remove the undissolved phase before the GPC measurements.

8.2.3 Fourier-transform infrared spectroscopy (FTIR)

Fourier-transform infrared spectroscopy (FTIR) are commonly utilized techniques to identify the functional groups of unknown compounds by measuring their infrared absorption spectrum. Fourier-transform infrared spectroscopy (FTIR) collects the interfergram signals via an interferometer, translates the interfergram by using mathematical Fourier transform, and then displays the desirable spectrum. Attenuated total reflection (ATR) is an advanced FTIR technique which could allow the fast analysis of samples in their nature states without additional sample preparation process, therefore it has been intensively utilized in this work. The mechanism of ATR-FTIR is illustrated in **Figure 8.2.1.** In principle, an IR beam is emitted to the ATR crystal featuring with a high refractive index, and when the slop of incident beam is above the critical angle, the IR beam will be reflected completely, producing an evanescent wave at the same time. Once contacting with the sample placed directly on the ATR crystal surface, the evanescent wave will penetrate into the

specimen between 0.5 and 2 μm, and the wave energy absorption on the sample will lead to an attenuated IR beam. The attenuated IR beam will be eventually collected by the detector and further translated into IR spectra.[250]

In this work, all the FT-IR spectra were recorded from a Bruker VERTEX 80V FT-IR spectrometer within the range of 4000-600 cm^{-1} at ambient temperature.
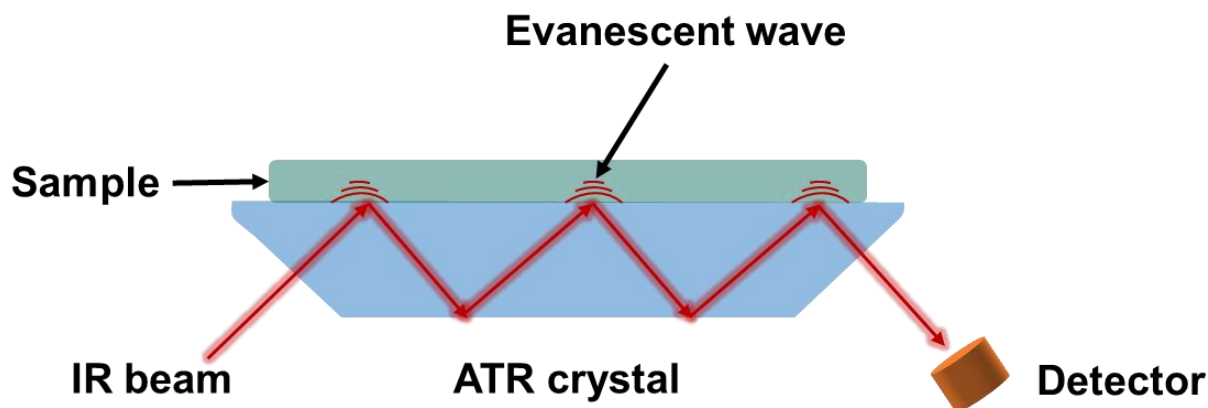
Figure 8.2.1. Schematic illustration of an ATR-FTIR system.

8.2.4   Ultraviolet-visible (UV-vis) spectroscopy

Ultraviolet-visible (UV-vis) spectroscopy is another spectrophotometric technique which is based on the absorption of electromagnetic radiations in ultraviolent (10-400 nm) and visible (400-800 nm) regions. The electrons of the molecules will be excited from stable ground state to higher energy state after absorbing the radiation energy, and the corresponding wavelength of the absorbed radiation was equal to the energetic difference between the excited state and the ground state. By plotting the amount of absorbed energy against the wavelength of the absorbed irradiations, a UV-vis spectrum was obtained which could be applied for identifying certain functional groups, as well as quantitatively calculating their concentrations according to the Beer-Lambert Law.[251]

In Chapter 4.1, Py-β-CD/SWCNTs suspension was prepared by sonicating Py-β-CD (50 mg) in 0.1 M NaOH with SWCNTs (10 mg) for 4 h, and the UV/vis absorption spectra were recorded on an Ocean optics spectrometer at ambient temperature.

In Chapter 4.2, the dispersion of SWCNTs was prepared by dissolving SWCNTs and P2 in aqueous solution with the weight ratio of SWCNTs : P2 =1 : 10 (corresponding weight ratio of CNTs : pyrene moieties $\approx$ 1:1), and then treated with sonication for 1 h. UV/vis absorption spectra were recorded on a Perkin Elmer Lambda 35 UV/Vis spectrometer with Peltier system at ambient temperature. The transmittances of the SWCNTs dispersion were recorded with an Ocean optics spectrometer at ambient temperature.

8.2.5   Scanning electron microscopy (SEM)

Scanning electron microscopy (SEM) is a widely used technique to characterize the surficial micro-morphologies of the observed specimen. In a typical imaging process, electrons were first emitted from electron gun, accelerated in the applied electric field, accumulated into a high-energy electron beam by passing through series of lens and apertures, which eventually hit on the sample surface. As a result, a variety of signals, including secondary electrons, backscattered electrons and characteristic X-rays were produced and collected by corresponding detectors. Normally, the collecting signals from secondary electrons were utilized for investigating the morphology and topography of the specimen.

Morphological images of hydrogels were obtained from a Zeiss LEO 1350 field emission scanning electron microscope. Freeze-dried hydrogel samples were prepared by lyophilization overnight before measurement.

8.2.6   Electrical characterizations

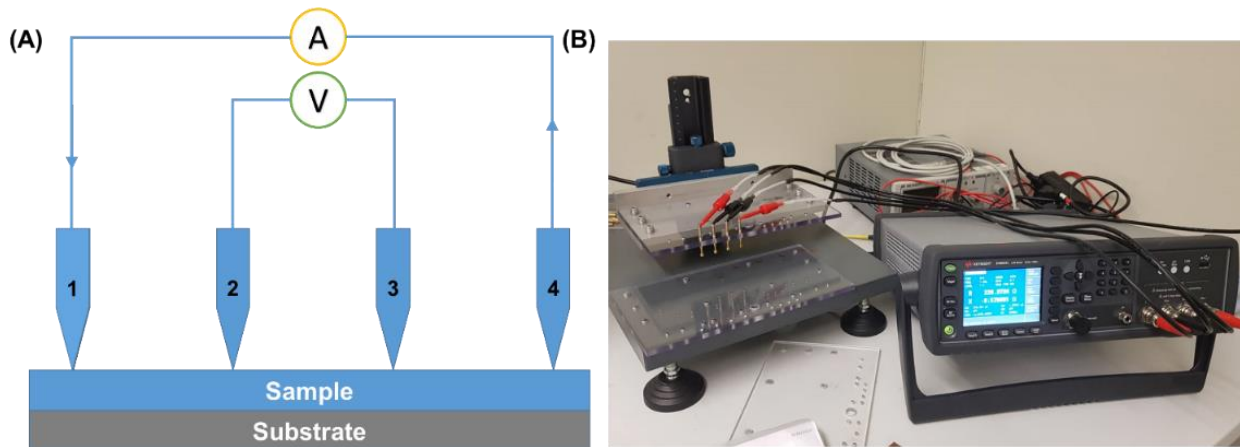Electrical conductivity was measured by four-point probe method,[252] as shown in **Figure 7.2.2**. Sample was put on an insulated substrate and connected to a digital LCR meter by contacting with four equally-spaced and co-linear copper probes. A constant current (I) was loaded on probe 1 and probe 4, and corresponding voltage drop (V) between probe 2 and probe 3 was recorded to deliver the electrical resistance (Ω).

Electrical conductivity was calculated by the following equation:

$$\sigma = \frac{1}{R}\frac{l}{wt}$$

where R is the measured resistance, l is the length between the adjacent probes, w is the width of the sample, and t is the thickness of the sample.

In Chapter 4.2, to determine the conductivity of the hydrogels with different CNT concentrations, hydrogel samples were first prepared and then moulded into rectangle thin films (50 mm in length, 5 mm in width). Subsequently, electrical resistance (Ω) was monitored using LCR meter (KEYSIGHT, E4980AL) by four-point probe method, and corresponding electrical conductivity was calculated by the above formulation. Real-time monitoring of the electrical signals from the cut and self-healed hydrogels was performed on Fluke 287 digital multimeter. Hydrogel samples were tethered to the multimeter by copper tape. Real-time monitoring of the electrical signals from the cut and self-healed hydrogels was performed on Fluke 287 digital multimeter. Hydrogel samples were tethered to the multimeter by copper tape.

Figure 8.2.2 (A) Schematic illustration of the mechanism of four-point probe method for electrical conductivity measurement. (B) Photograph showing the in-situ measurement platform, including the four-point probes and a LCR meter.

8.2.7   Rheological measurements

Rheological measurements were performed directly on the as-fabricated and disk-shaped samples to characterized their mechanical properties. All the rheological measurements in this thesis were based on small amplitude oscillatory shear testing (SAOS), which is widely utilized to characterize the viscoelastic properties of polymer samples.

In chapter 4.2, rheological measurements were performed on a HAAKE RS 150 Rheometer with a 25 mm plate-plate geometry. First, oscillation amplitude strain sweep measurements were conducted to determine the linear viscoelastic region of the hydrogels at a constant frequency of 1 Hz. Then, frequency sweep measurements were performed at a constant strain of 1% to determine the storage modulus G' and loss modulus G'' over the frequency region from 0.1 to 10 Hz. As for the self-healing experiments, dynamic rheology tests were performed on hydrogel samples with 4 mg/mL SWCNTs. Strain-sweep test was first carried out over the strain region from 1% to 200% with a constant frequency of 1 Hz at 20 ℃. Afterwards, the alternate strain-sweep measurement was performed at 1 Hz and 20 ℃ under the cyclic change from small strain (1%) to large strain (100%).

In chapter 5, hydrogel samples were prepared in a cylindrical mould with a diameter of 28 mm to obtain uniform disc-shaped specimens with a height of 4 mm. Rheological measurements were performed on a ARES-G2 TA-instrument with a 28 mm plate-plate geometry. The geometry was lowered until a constant axial force of 0.5 N (812 Pa) was applied to the sample and the temperature was controlled to 25 ± 0.1 ℃ by a Peltier element (Advanced Peltier System, TA Instruments). Oscillatory amplitude strain sweep over the region from $\gamma\_0 = 0.1\%$ to 500% was performed prior to determine the linear viscoelastic region under a constant frequency of 1 Hz. Then, oscillatory frequency sweep was conducted to determine the storage modulus G' and loss modulus G'' over the frequency region from 0.2 to 300 rad/s at a constant strain of $\gamma_0 = 0.1\%$. A solvent trap was utilized to avoid water evaporation during the tests.

In chapter 6, stress relaxation experiments were conducted on a strain-controlled rheometer, ARES-G2 (TA Instruments, New Castle, USA), with a 13 mm plate-plate Invar geometry. The loaded samples were first equilibrated at the set temperatures and then subjected to a constant stain within the linear viscoelastic region of the material (0.5 – 2%) and the stress decay was recorded immediately. The temperature was elevated by

5 °C for each test. The characteristic relaxation times, τ, and the activation energy, E_a, were determined by using the standard procedures.[253]

8.2.8 Mechanical characterizations

All mechanical tests were performed on a universal tensile testing machine (TA-XT Plus Texture Analyzer) at room temperature. Compression tests were performed on cylinder-shaped samples with a diameter of 10 mm and height of 6~7 mm at a crosshead speed of 10% strain/min. Rectangle-shaped samples with size of 30×15×2 mm were used for tensile tests at a crosshead speed of 10 mm/min. The nominal stress (σ) was defined as $\sigma = F/S$, where F was the loading force and S was the initial cross-sectional area of the sample. The nominal strain (ε) was defined as $\varepsilon = \Delta l/l$, where Δl was the length change and l was the initial length. The toughness of hydrogel was estimated by integrating of the area under the stress-strain curves, and the dissipated energy was calculated by the area of hysteresis loops in one cyclic curve.

8.2.9 Differential Scanning Calorimetry (DSC)

Differential scanning calorimetry (DSC) is one of the commonly used techniques in the thermal characterization fields. It is based on the difference in the amount of absorbed or released energy between the sample and the reference pan when they are heated or cooled under the same temperature. In principle, the sample could undergo some endothermic process (such as glass transition and melting) or exothermic process (like crystallization), inducing more or less heat flow is needed in order to maintain the same temperature as the reference pan. By monitoring the corresponding difference in the heating flow, DSC curve could be obtained as the heating flow against the temperature, and characteristic temperature, such as the glass transition temperature (T_g), melting temperature (T_m) and crystallization temperature (T_c) of the sample could be determined.

Differential scanning calorimetry (DSC) was performed on TA Instruments Q200. The sample underwent cyclic heating-cooling procedure twice from -50 TGA5500 to 200 °C, with a rate of 5 °C/min. The glass transition temperature (T_g) is defined as the lowest derivative of heating flow in the second heating process.
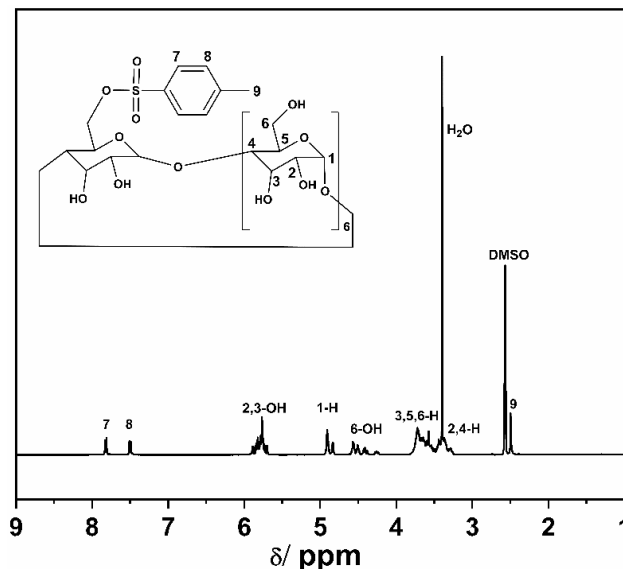
8.3   Experimental Procedures

8.3.1   Synthesis of mono-6-dexoy-6-(*p*-tolysulfonyl)-*β*-CD (*β*-CD-OTs)
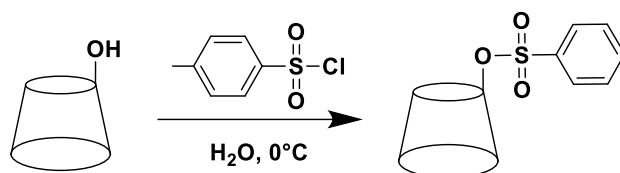
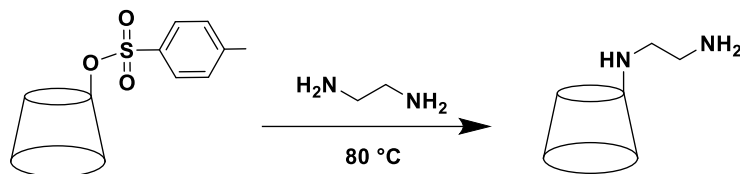**Scheme 8.3.1.** The synthesis route of mono-6-dexoy-6-(*p*-tolysulfonyl)-*β*-CD (*β*-CD-OTs).

β-CD (6 g, 5.28 mmol, 1.0 eq) was dissolved into 50 mL of H_2O, followed by the addition of NaOH (0.657 g, 16.41 mmol, 3.1 eq) in 2 mL of H_2O. The mixture solution was stirred at 0 °C in an ice bath for 30 min. Afterwards, TsCl (1.512 g, 7.92 mmol, 1.5 eq) dissolved into 3 mL acetonitrile was added dropwise into the mixture solution. The whole mixture was stirred in the ice bath for 30 min, further at room temperature for another 4 h, and then refrigerated overnight. Afterwards, precipitation was filtered and recrystallized three times from deionized water. The final product was obtained as white crystal after dried under vacuum at 45 °C for 24 h (yield: 1.2 g, 17.6%).

^{1}H NMR (400 MHz, DMSO-d_6, δ in ppm): 7.82 (d, 2H, –**Ar**), 7.50 (d, 2H, –**Ar**), 5.94 – 5.67 (m, 7H, –O**H** from *β*-CD), 4.97 – 4.78 (m, 7H, repeat units from *β*-CD), 4.61 – 4.45 (m, 6H, –O**H** from *β*-CD), 3.82 – 3.23 (m, 42H, repeat units from *β*-CD), 2.49 (d, 3H, –**CH**$_3$).

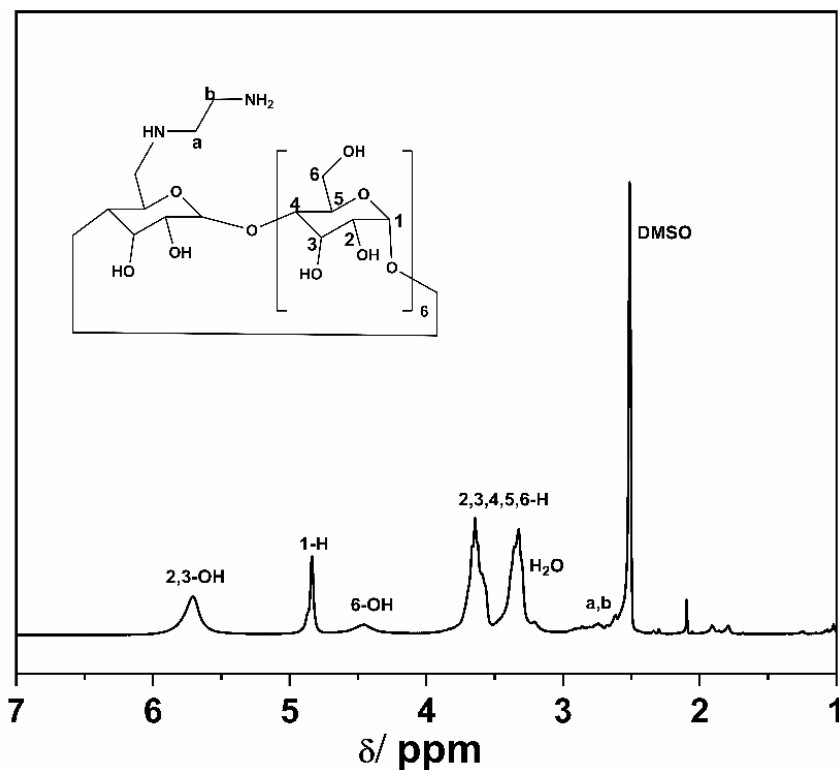**Figure 8.3.1.** ^{1}H-NMR spectra (400 MHz) of mono-6-dexoy-6-(*p*-tolysulfonyl)-*β*-CD (*β*-CD-OTs) DMSO-d_6.

8.3.2   Synthesis of mono-6-dexoy-6-(*p*-ethylenediamine)-*β*-CD (*β*-CD-NH₂)

Scheme 8.3.2. The synthesis route of mono-6-dexoy-6-(p-ethylenediamine)-*β*-CD (*β*-CD-NH₂).

β-CD-OTs (0.3 g, 0.2 mmol) was dissolved into 4 mL of EDA, and refluxed at 80 °C overnight. Then, the EDA was removed by rotary evaporation. Afterwards, the crude product was re-dissolved into water/methanol mixture (3:1, v/v), and precipitated into acetone three times. The purified product was finally obtained as white solid after dried under vacuum oven at 45 °C for 24 h (yield: 0.2 g, 85.1%).

^{1}H NMR (400 MHz, DMSO-d_6, δ in ppm): 5.71 (s, 14H, –**OH** from *β*-CD), 4.84 (s, 7H, repeat units from *β*-CD), 4.46 (s, 6H, –**OH** from *β*-CD), 3.82 – 3.23 (m, 42H, repeat units from *β*-CD), 2.85 – 2.65 (m, 4H, –NH–**CH₂**–**CH₂**–NH₂).

Figure 8.3.2. ^{1}H-NMR spectra (400 MHz) of mono-6-dexoy-6-(p-ethylenediamine)-*β*-CD (*β*-CD-NH₂) in DMSO-d_6.

8.3.3 Synthesis of mono-6-(2-pyrenebutylamino)-6-deoxy-*β*-CD (Py-*β*-CD)
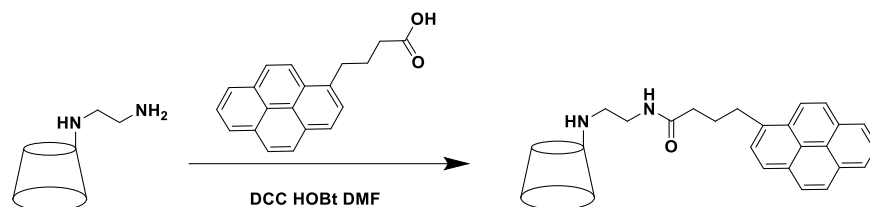
Scheme 8.3.3. The synthesis route of mono-6-(2-pyrenebutylamino)-6-deoxy-*β*-CD *(Py-β-CD).*

*β*-CD-NH$_2$ (500 mg, 0.44 mmol, 1.0 eq), 1-pyrenebutyric acid (254 mg, 1.09 mmol, 2.5 eq), DCC (200 mg, 0.97 mmol, 2.2 eq) and HOBt (100 mg, 0.74 mmol, 1.7 eq) were dissolved into 5 mL of anhydrous DMF solvent at 0 °C under nitrogen atmosphere. The mixture was stirred in an ice bath for 1 h, and then for another 24 h at ambient temperature. The insoluble salts were filtered and the filtrate was then precipitated into acetone. The precipitation was then washes with water several times to remove the excess *β*-CD-NH$_2$. The final product was obtained as a yellow solid after freeze-dried for 48 h. (yield: 310 mg, 50.7%).

^{1}H-NMR (400 Hz, DMSO-d_6, $δ$ in ppm): 8.70 – 7.86 (m, 9H, pyrene group), 5.97 – 5.68 (m, 14H, –O**H** from *β*-CD), 4.96 (d, s, 7H, repeat units from *β*-CD), 4.55 (s, 6H, –O**H** from *β*-CD), 3.82 – 3.23 (m, 44H, repeat units from *β*-CD and –C**H**$_2$–pyrene), 2.09 (d, 2H, –C**H**$_2$–CH$_2$–pyrene).
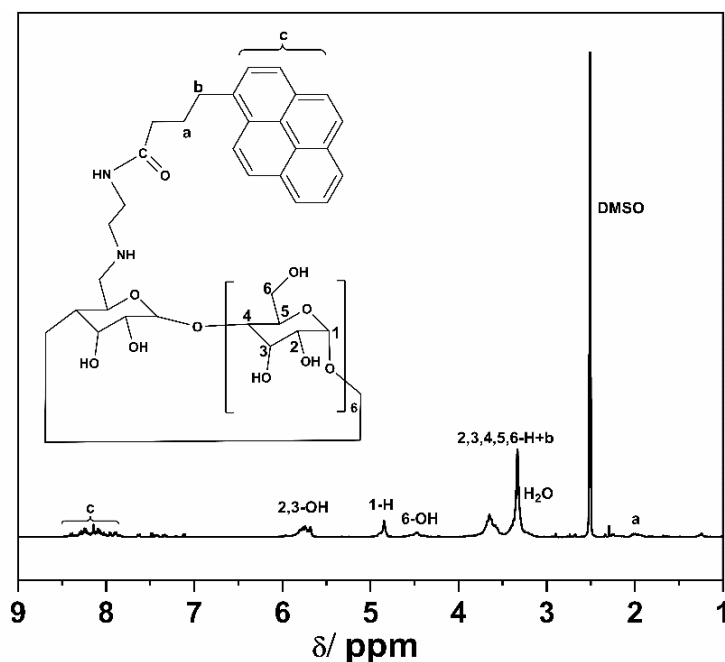
Figure 8.3.3. ^{1}H-NMR spectra (400 MHz) of mono-6-(2-pyrenebutylamino)-6-deoxy-*β*-CD (Py-*β*-CD) in DMSO-d_6.

8.3.4 Synthesis of 1-Adamantyl 2-Bromoisobutyrate (ABIB)
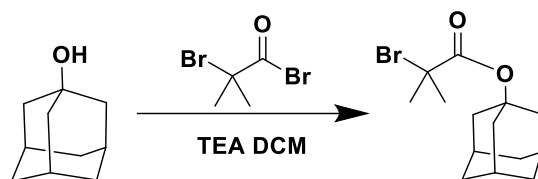
Scheme 8.3.4. The synthesis route of 1-Adamantyl 2-Bromoisobutyrate (ABIB).

The ATRP initiator, ABIB, was prepared by the esterification reaction of 1-adamantanol with 2-bromoisobutyryl bromide. Briefly, 1-adamantanol (7.61 g, 0.05 mol, 1.0 eq), TEA (6.07 g, 0.06 mol, 1.2 eq), and dry CH_2Cl_2 (100 mL) were added into a 250 mL round-bottom flask. The mixture was cooled to 0 °C in an ice-water bath. Afterwards, 2-bromoisobutyryl bromide (7.42 mL, 0.06 mol, 1.2 eq) in CH_2Cl_2 (20 mL) was added dropwise over 1 h followed by stirring at 0 °C for 1 h and then at room temperature for another 12 h. After removing the insoluble salts, the organic solvent was washed three times with DI water, and condensed by a rotary evaporator. Then, the mixed chemicals were resolved in DCM and then purified by silica gel column chromatography using petroleum ether/ethyl acetate (10:1 v/v) as the eluent. After removing the solvents by a rotary evaporator, ABIB was obtained as a white solid (yield: 12.7 g, yield: 85%)

^{1}H-NMR (400 Hz, CDCl$_3$, δ in ppm): 2.12 (s, 3H, from adamantane), 2.07 (s, 6H, from adamantane), 1.81 (s, 6H, –**CH$_3$**), 1.61 (s, 6H, from adamantane).
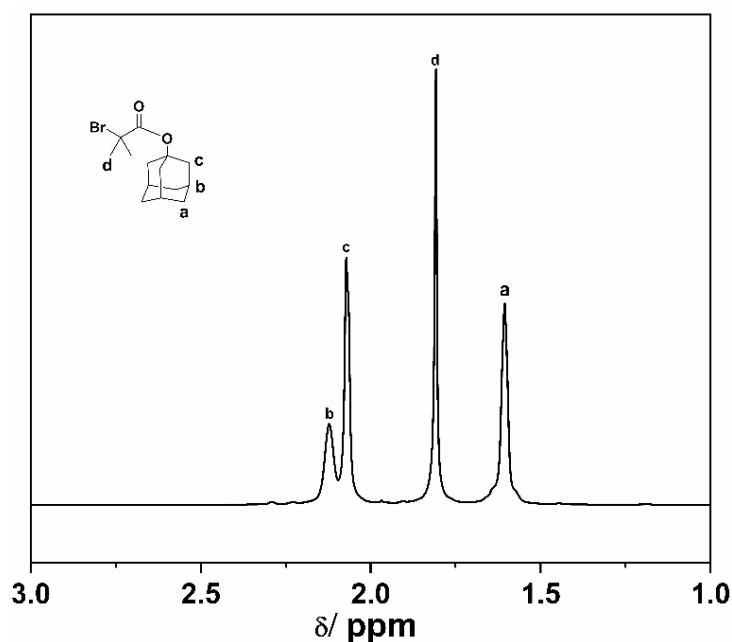
Figure 8.3.4. ^{1}H-NMR spectra (400 MHz) of 1-Adamantyl 2-Bromoisobutyrate (ABIB) in CDCl$_3$.

8.3.5   Synthesis of pentafluorophenyl acrylate (PFPA)
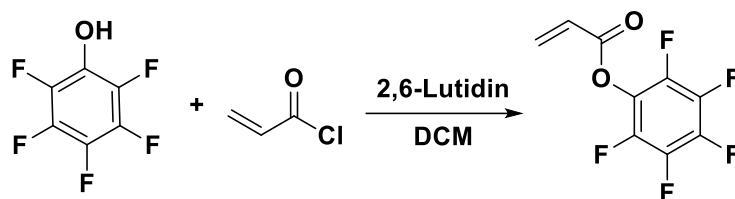
Scheme 8.3.5. The synthesis route of pentafluorophenyl acrylate (PFPA).

Pentafluorophenol (80 g, 0.434 mmol, 1.0 eq) and 2,6-Lutidin (47.5 g, 0.443 mmol, 1.02 eq) were dissolved in 700 mL DCM in a round bottom flask under stirring in an ice bath. After that, acryloyl chloride (42.27 g, 0.467 mmol, 1.07 eq) was added dropwise into the mixture and kept stirring in the ice bath for 3 h. The whole mixture was then stirred for another 20 h at ambient temperature. Subsequently, precipitate was filtered and the mixture was condensed to around 200 mL under reduced pressure. The organic fraction was then washed with water (3 x 50 mL), dried with anhydrous magnesium sulfate, and then further condensed under reduced pressure to deliver the crude product. Final purified product was obtained as colorless oily liquid by passing through a silicone gel column in hexane (72 g, yield 70%).

^{1}H NMR (400 MHz, CDCl$_3$, δ in ppm): 6.74 (dd,1H, **CH$_2$**=CH-), 6.39 (dd,1H, CH$_2$=**CH**-), 6.20 (dd, 1H, **CH$_2$**=CH-).

^{19}F NMR (376 MHz, CDCl$_3$, δ/ppm): -153.16 (*ortho*), -158.51 (*para*), -163.01 (*meta*)
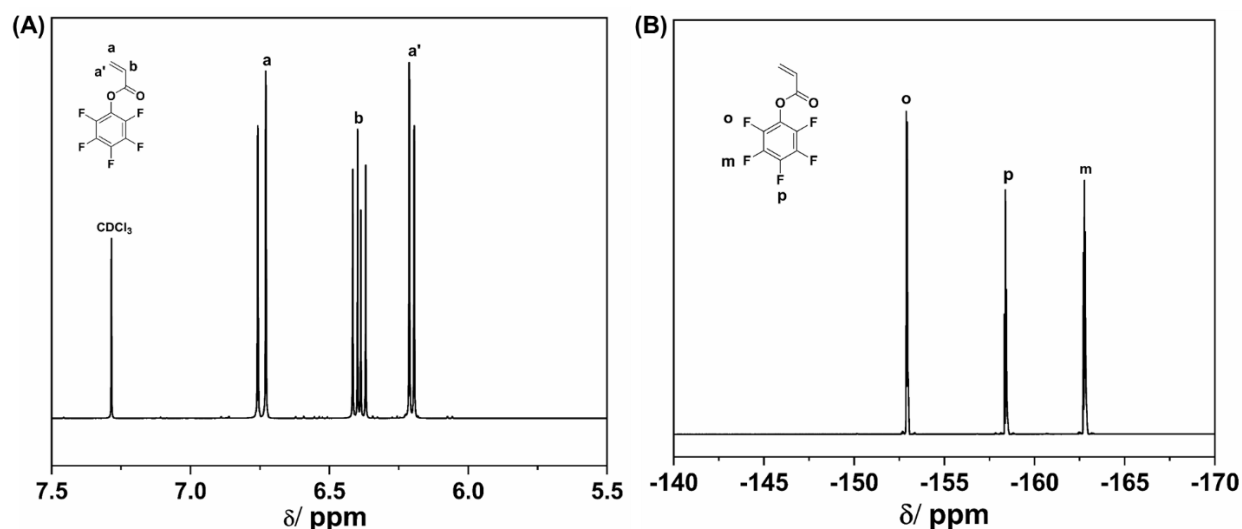
Figure 8.3.5. (A) ^{1}H-NMR spectra (400 MHz) and (B) ^{19}F-NMR spectra (376 MHz) for pentafluorophenyl acrylate (PFPA) in CDCl$_3$.

8.3.6 Synthesis of perfluorophenyl 4-(pyren-1-yl) butanoate
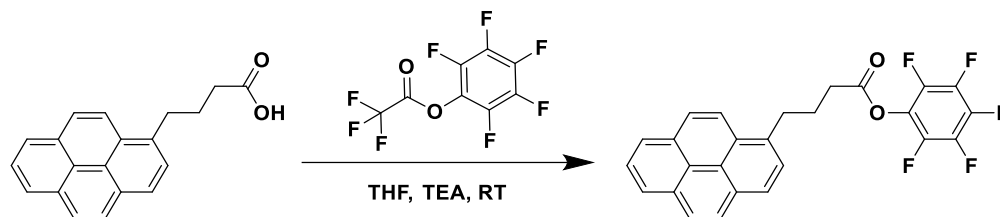
Scheme 8.3.6. The synthesis route of perfluorophenyl 4-(pyren-1-yl) butanoate.

1-Pyrenebutyric acid (1.2 g, 4.2 mmol, 1.0 eq) and trimethylamine (1.72 mL, 12.6 mmol, 3.0 eq) were dissolved in 10 mL of dry THF, and then pentafluorophenyl trifluoroacetate (2.2 mL, 12.6 mmol, 3.0 eq) was added dropwise. The solution was stirred overnight at ambient temperature. Afterwards, THF was removed under reduced pressure. The residue was re-dissolved in 100 mL of DCM and washed by water (3 x 20 mL). The combined organic solvent was dried with anhydrous $MgSO_4$ and then condensed. Final product was obtained as a yellow powder after being purified by column chromatography (silica, DCM) and dried under vacuum at 45 °C (1.4 g, yield 73.7%).

^{1}H-NMR (400 Hz, CDCl$_3$, δ in ppm): 8.70 – 7.86 (m, 9H, pyrene group), 3.58 – 3.46 (m, 2H, –**CH$_2$**–pyrene), 2.81 (t, 2H, –**CH$_2$**–CH$_2$–pyrene), 2.42 – 2.31 (m, 2H, –CH$_2$–**CH$_2$**–C$_6$F$_5$).

^{19}F-NMR (376 MHz, CDCl$_3$, δ in ppm): -152.71 (*ortho*), -158.03 (*para*), -162.28 (*meta*).

FT-IR: v (cm^{-1}): 1774 (C=O ester bond), 1520 (aromatic C=C from PFP).
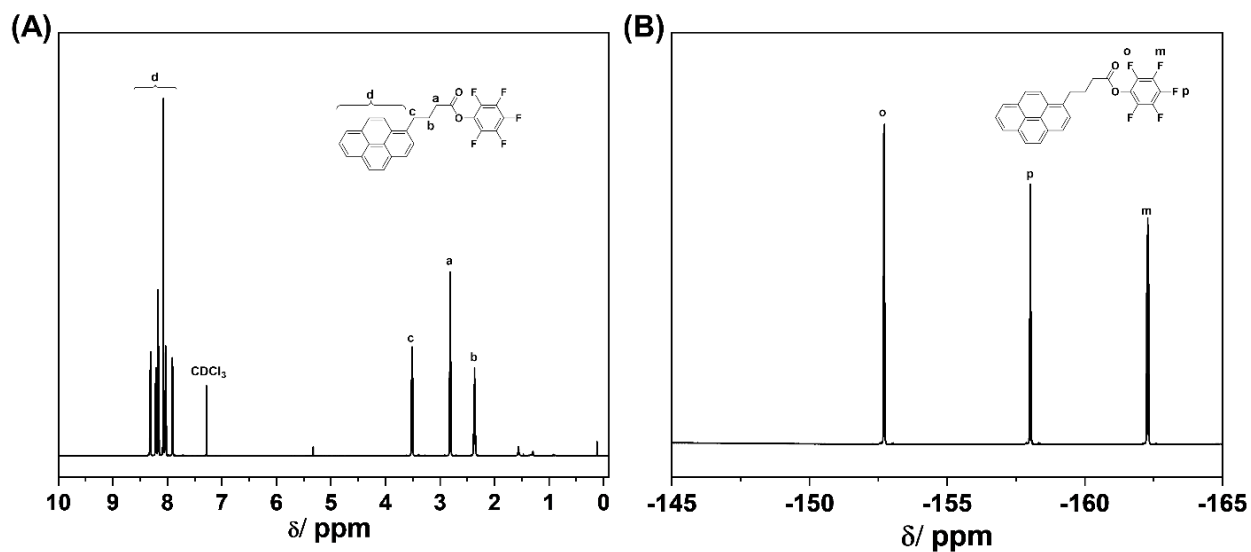
Figure 8.3.6. (A) ^{1}H-NMR spectra (400 MHz) and (B) ^{19}F-NMR spectra (376 MHz) of perfluorophenyl 4-(pyren-1-yl) butanoate in CDCl$_3$.

8.3.7   Synthesis of *N*-(6-aminohexyl)-4-(pyren-1-yl) butanamide (APB)
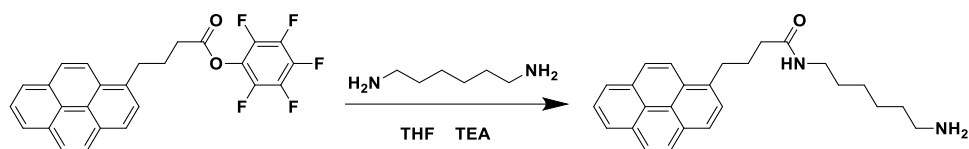
Scheme 8.3.7. The synthesis route of *N*-(6-aminohexyl)-4-(pyren-1-yl) butanamide (APB).

In a round flask, 1,6-hexamethylenediamine (2.04 g, 17.5 mmol, 20 eq) and TEA (0.24 mL, 1.75 mmol, 2 eq) were dissolved into 10 mL THF, and then perfluorophenyl 4-(pyren-1-yl) butanoate (0.4 g, 0.88 mmol, 1.0 eq) was dissolved in 2 mL THF and added dropwise. The mixture was stirred overnight at ambient temperature, and then THF was removed under reduced pressure. The residue was re-dissolved in 50 mL of DCM and washed by water (3 x 10 mL). The combined organic solvent was dried with anhydrous $MgSO_4$ and then condensed under reduced pressure. Final product was obtained as a yellow powder after being dried under vacuum at 45 °C (240 mg, yield 70.6 %).

^{1}H-NMR (400 MHz, DMSO-d_6, δ in ppm): 8.48 – 7.88 (m, 9H, pyrene group), 3.33 – 3.29 (m, 2H, –**CH**$_2$–pyrene), 3.06 (dd, 2H, –**CH**$_2$–CH$_2$–pyrene), 2.50 – 2.47 (m, 2H, –**CH**$_2$–NH$_2$), 2.23 (t, 2H, –C(O)– NH–**CH**$_2$), 2.08 – 1.96 (m, 2H, –**CH**$_2$–CH$_2$–pyrene), 1.44 – 1.37 (m, 2H, –**CH**$_2$–CH$_2$–NH$_2$), 1.35 – 1.20 (m, 6H, –(**CH**$_2$)$_3$–(CH$_2$)$_2$–NH$_2$).
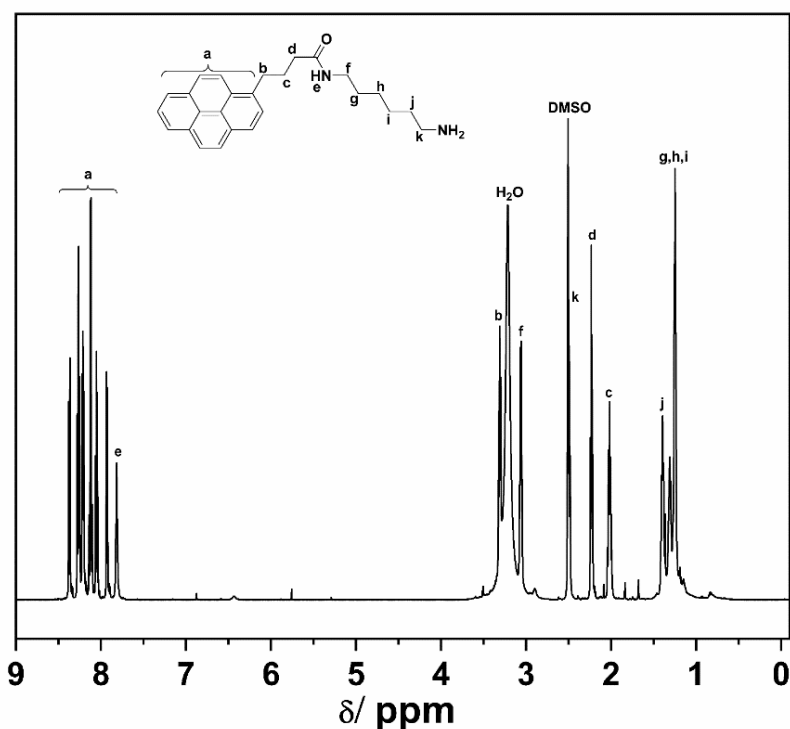
Figure 8.3.7. ^{1}H-NMR spectra (400 MHz) of *N*-(6-aminohexyl)-4-(pyren-1-yl) butanamide (APB) in DMSO-d_6.

8.3.8   Synthesis of poly((3-Acrylamidopropyl) trimethylammonium chloride) (PAMPT)
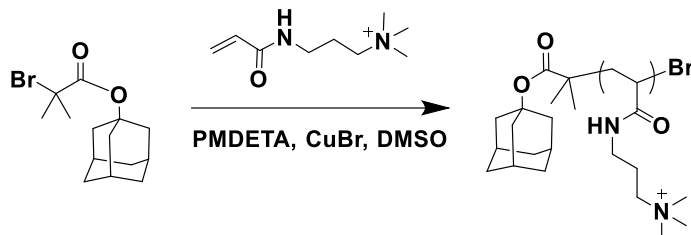
Scheme 8.3.8. The synthesis route of poly((3-Acrylamidopropyl) trimethylammonium chloride) (PAMPT).

AMPTMA (4.8 mmol, 1.34 g) was dissolved into 2 mL of anhydrous DMSO in a Schlenk tube, and then degassed three times by freeze-chawing method. Afterwards, CuBr (0.048 mmol, 6.88 mg) and PMDETA (0.096 mmol, 16.6 mg) was added into the Schlenk tube quickly when the mixture was in freeze state. The Schlenk tube was further degassed three times to remove the oxygen inside. Meanwhile, initiator ABIB (0.04 mmol, 14.4 mg) dissolved into 1 mL of anhydrous DMSO was degassing under N_2 flow and then transferred into Schlenk tube to start the reaction. The whole mixture was stirred at 70 °C for 20 h.

^{1}H NMR (400 MHz, D_2O, δ in ppm): 3.49 – 3.09 (m, 13H, repeating units from AMPTMA), 2.13– 1.70 (m, backbone of PAMPTMA and $-CH_2-CH_2-N(CH_3)_3$), 1.12 (d, 12H, from ABIB).
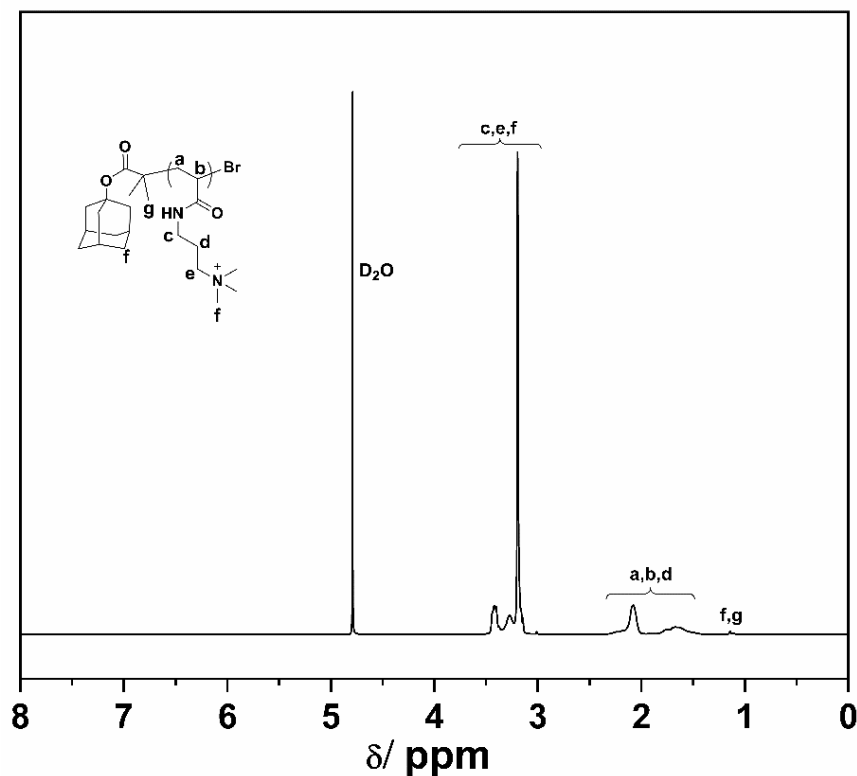
Figure 8.3.8. ^{1}H-NMR spectra (400 MHz) of poly((3-Acrylamidopropyl) trimethylammonium chloride) (PAMPTMA) in D_2O.

8.3.9 Synthesis of poly(*N,N*-dimethyl acrylamide-*co*-pentafluorophenyl acrylate) (P(DMA-*co*-PFPA)) (P1)
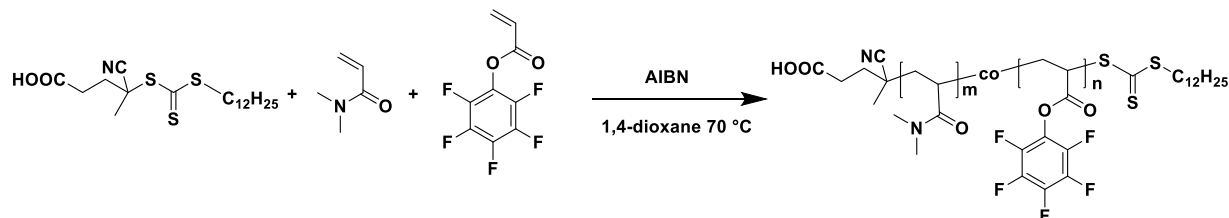
Scheme 8.3.9. The synthesis route of poly(*N,N*-dimethyl acrylamide-co-pentafluorophenyl acrylate) (P(DMA-*co*-PFPA)) (P1).

Pentafluorophenyl acrylate (PFPA) was synthesized according to a previously published procedure. Accordingly, hydrophilic copolymer P(DMA-*co*-PFPA) was synthesized via typical RAFT polymerization. Briefly, *N,N*-Dimethyl acrylamide (20 mmol, 2.0 g), pentafluorophenyl acrylate (2.2 mmol, 0.534 g), RAFT agent CDTPA (0.075 mmol, 30 mg), AIBN (0.0075 mmol, 1.2 mg) and 6 mL of dried 1,4-dioxane was added into a pre-dried Schlenk tube. The mixture was degassed three times through freeze-thawing cycles. Subsequently, the Schlenk tube was transferred into pre-heated oil bath at 70 °C and stirred for additional 16 h. The reaction was terminated by cooling down in liquid nitrogen, and then exposure to air. The crude copolymer was purified via precipitation from THF into ice cold *n*-hexane three times. The final product was dried under vacuum at 45 °C overnight (2.3 g, yield 92 %).

^{1}H-NMR (400 Hz, CDCl$_3$, δ in ppm): 3.18–2.76 (d, 7H, –CH$_2$–**CH**– from the backbone of PPFPA and –N(C**H**$_3$)$_2$ from the side chain of PDMA), 2.75–2.54 (s, 1H, –CH$_2$–**CH**– in the backbone of PDMA), 2.0–1.0 (m, 2H, –**CH**$_2$–CH– in the backbone of PPFPA and PDMA), 0.88 (t, 3H, –**CH**$_3$ from CTA).

^{19}F-NMR (377 MHz, CDCl$_3$, δ in ppm): -152.54 (*ortho*), -157.44 (*para*), -162.05 (*meta*) from PPFPA.

GPC: $M_{n, \text{GPC}} = 2.32 \times 10^4$ g mol^{-1}, $M_w/M_n = 1.44$.

8.3.10 Synthesis of poly(*N,N*-dimethyl acrylamide-*co*-aminohexyl pyren-butane acrylamide-*co*-methylphenylboronic acid acrylamide) (P(DMA-*co*-APB-*co*-PBA)) (P2)
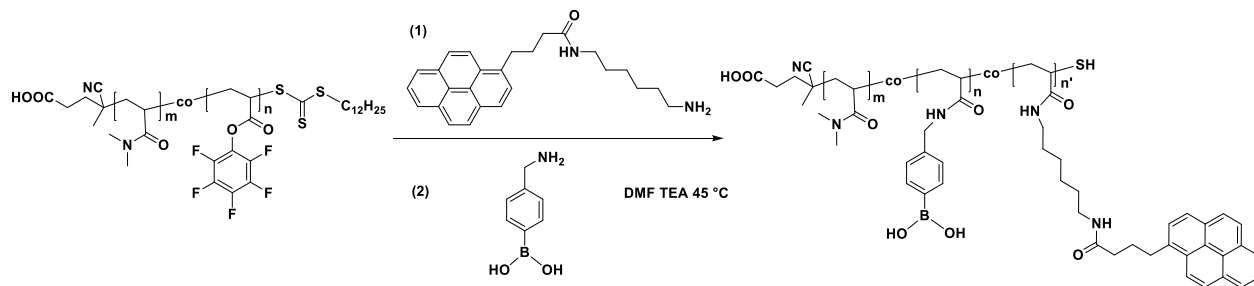
Scheme 8.3.10. The synthesis route of poly(*N,N*-dimethyl acrylamide-co-aminohexyl pyren-butane acrylamide-*co*-methylphenylboronic acid acrylamide) (P(DMA-*co*-APB-*co*-PBA)) (P2).

P(DMA-*co*-APB-*co*-PBA) (P2) was synthesized via sequential post-polymerization modification process. Briefly, P(DMA-*co*-PFPA) (1.0 g, containing 1mmol PPFPA) was dissolved into 6 mL anhydrous DMF in a vial. To this, *N*-(6-aminohexyl)-4-(pyren-1-yl) butanamide (APB) (115.8 mg, 0.3 mmol) in 1 mL dry DMF was added, followed by 0.15 mL TEA. The vial was sealed with rubber septum and placed into pre-heated oil bath at 45 °C. After 6 h, an excess of (4-aminomethylphenyl) boronic acid hydrochloride (PBA) (190.5 mg, 1.05 mmol) was dissolved into 1 mL dry DMF and added into the reaction mixture. Subsequently, the mixture was stirred overnight at 45 °C. After that, the copolymer was purified via dialysis against MeOH for 24 h, and DI water, respectively, for another 24 h. The final product was isolated as a pale yellow solid after lyophilisation (850 mg, yield 85%).

^{1}H-NMR (400 Hz, CDCl$_3$, δ in ppm): 8.30–7.86 (m, 9H, pyrene group), 7.85–7.67 (s, 2H, **Ar**–B(OH)$_2$), 7.28–7.18 (s, 2H, **Ar**–B(OH)$_2$), 3.37–3.21 (s, 2H, –NH–**CH**$_2$-Ar), 3.18–2.76 (d, 6H, –N(**CH**$_3$)$_2$ from the side chain of PDMA), 2.75–2.0 (m, 1H, –CH$_2$–**CH** in the backbone), 2.0–1.0 (m, 2H, –**CH**$_2$–CH– in the backbone).

FT-IR: v (cm^{-1}): 3433 (broad, $v_{\text{-OH-}}$ in Ar-B(OH)$_2$), 1720 ($v_{\text{-C=O-}}$ in pendent *N*-(6-aminohexyl)-4-(pyren-1-yl) butanamide (APB) moieties).

GPC: $M_{\text{n, GPC}} = 2.69 \times 10^4$ g mol^{-1}, $M_{\text{w}}/M_{\text{n}} = 1.40$.

8.3.11 Synthesis of poly(*N,N*-dimethyl acrylamide-*co*-ethyl diacrylate-*co*-isopropylidene ethyl acrylate) (P(DMA-*co*-EDA-*co*-IPA))
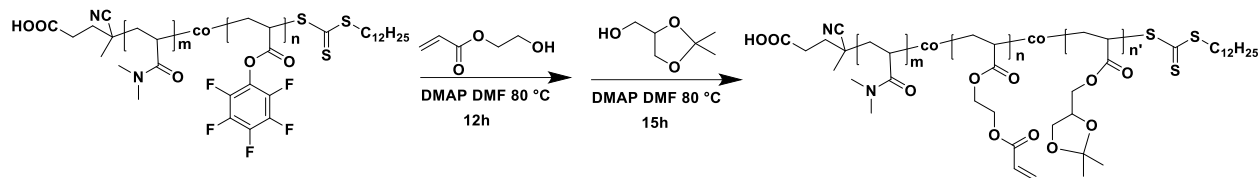
Scheme 8.3.11. The synthesis route of poly(*N,N*-dimethyl acrylamide-*co*-ethyl diacrylate-*co*-isopropylidene ethyl acrylate) (P(DMA-*co*-EDA-*co*-IPA)).

P(DMA-*co*-EDA-*co*-IPA)) (P2) with the designated molar feeding ratio of EDA: IPA = 30: 70 was synthesized via two-steps transesterification modification. Firstly, P(DMA-*co*-PFPA) (1 g, containing 1 mmol PPFPA) was dissolved into 6 mL of dry DMF in a vial, followed by adding with DMAP (97.7 mg, 0.8 mmol, 0.8 equiv. of PPFPA). Then, 2-hydroxyethyl acrylate (34.8 mg, 0.3 mmol, 0.3 equiv. of PPFPA) dissolved in 1 mL of dry DMF was added into the vial. The mixture was stirred for 12 h at 80 °C. After that, a slight excess of isopropylideneglycerol (118.9 mg, 0.9 mmol, 0.9 equiv. of PPFPA) dissolved in 1 mL of dry DMF was added and the mixture was stirred for another 15 h at 80 °C. Afterwards, a small amount of the mixture was withdrawn and dialysis against to DI water directly for two days for characterization and this P2 sample was obtained as a pale yellow solid after lyophilization. The remaining parts of the mixture were immediately exposed to the deprotection (see below). P(DMA-*co*-EDA-*co*-IPA)) (P2) with other molar ratio of EDA: IPA was synthesized by the same procedure.

^{1}H NMR (400 MHz, CDCl$_3$, δ in ppm): 6.38 (d,1H, **CH**$_2$=CH–), 6.17–5.98 (m, 1H, CH$_2$=C**H**–), 5.86 (d, 1H, **CH**$_2$=CH–), 4.74–3.53 (m, 9H, –O–**CH**$_2$–**CH**$_2$–O– from PEDA, –C(O)O–**CH**$_2$–, –**CH**$_2$–**CH**(O)–, –CH(O)–**CH**$_2$– from PIPA), 3.34–2.73 (m, 6H, –N(**CH**$_3$)$_2$ from PDMA), 2.62 (s, 1H, –**CH**$_2$–**CH**– in the backbone of PDMA), 2.40–1.05 (m, 16H, –**CH**$_3$ from PIPA, –**CH**$_2$–CH$_3$ from CTA, –**CH**$_2$–**CH**– in the backbone of PDMA, PEDA and PIPA), 0.88 (t, 3H, –**CH**$_3$ from CTA).

FT-IR: v (cm^{-1}): 1720 ($v_{O=C-O-}$ in PEDA and PIPA)

GPC: $M_{n, GPC} = 1.12 \times 10^4$ g mol^{-1}, $M_w/M_n =1.89$

8.3.12 Synthesis of poly(*N*,*N*-dimethyl acrylamide-*co*-ethyl diacrylate-*co*-dihydroxypropyl acrylate) (P(DMA-*co*-EDA-*co*-DHA)) (P3)

Scheme 8.3.12. The synthesis route of poly(*N*,*N*-dimethyl acrylamide-*co*-ethyl diacrylate-*co*-dihydroxypropyl acrylate) (P(DMA-*co*-EDA-*co*-DHA)) (P3).
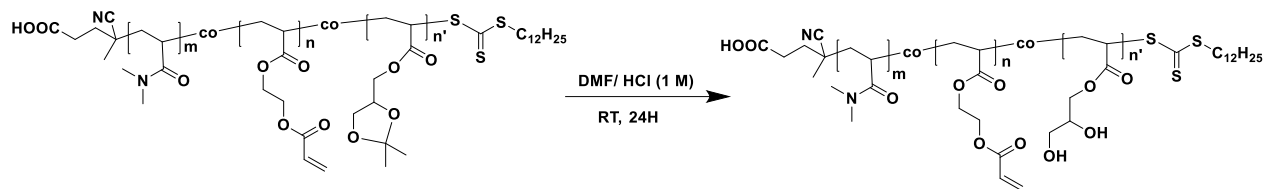
The remaining DMF solution of P2 was transferred into 50 mL round flask and mixed with 8 mL of 1M HCl solution. The whole mixture was stirred overnight at room temperature. The final product (P(DMA-*co*-EDA-*co*-DHA)) (P3) was purified via dialysis against DI water for 2 days and obtained as a pale brown solid after lyophilization (820 mg, yield: 82%).

^{1}H NMR (400 MHz, CDCl$_3$, δ in ppm): 6.38 (d,1H, **CH**$_2$=CH–), 6.17–5.98 (m, 1H, CH$_2$=**CH**–), 5.86 (d, 1H, **CH**$_2$=CH–), 4.74-3.53 (m, 11H, –O–**CH**$_2$–**CH**$_2$–O– in PEDA, –C(O)O–**CH**$_2$–, –**CH**$_2$–**CH**(O)–, –CH(O)–**CH**$_2$–, –**OH** from PDHA), 3.34 to 2.73 (m, 6H, –N(**CH**$_3$)$_2$ from PDMA), 2.62 (s, 1H, –CH$_2$–**CH**– in the backbone of PDMA), 2.40 – 1.05 (m, 10H, –**CH**$_2$–**CH**$_3$ from CTA, –**CH**$_2$–**CH**– in the backbone of PDMA, PEDA and PDHA), 0.88 (t, 3H, –**CH**$_3$ from CTA).

FT-IR: v (cm^{-1}): 3433 (broad, $v_{\text{-OH-}}$ in PDHA), 1720 ($v_{\text{O=C-O-}}$ in PEDA and PDHA).

GPC: $M_{\text{n, GPC}} = 1.98 \times 10^4$ g mol^{-1}, $M_{\text{w}}/M_{\text{n}} = 1.52$.

8.3.13 Synthesis of thiol-terminated Pluronic F127 (PF127-SH)
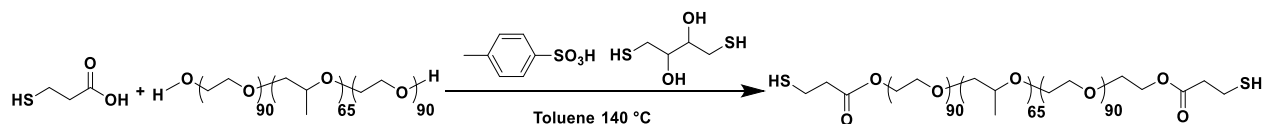
Scheme 8.3.13. The synthesis route of thiol-terminated Pluronic F127 (PF127-SH).

Thiol-terminated Pluronic F127 (PF127-SH) was synthesized according to a published procedure.[254] Briefly, 3-mercaptopropionic acid (2.13 g, 20 mmol), Pluronic F127 (12.5 g, 1 mmol), *p*-toluenesulfonic acid monohydrate (0.384 g, 2 mmol), DTT (1.54 g, 10 mmol) were dissolved in 200 mL of dry toluene in a round flask equipped with a Dean-Stark trap and an air condenser. The mixture solution was refluxed for two days at 140 °C until no water was evolved in the Dean-Stark trap. Afterwards, toluene was removed under reduced pressure. The residue was re-dissolved in 150 mL DCM, and washed by saturated saline (three times, 50 mL for each). The combined organic solvent was dried with anhydrous $MgSO_4$, condensed and then precipitated into 300 mL cold ethyl ether. The final product was obtained as white powder after being dried in a vacuum oven at 45°C (10 g, yield: 84.6%).

^{1}H NMR (400 MHz, CDCl$_3$, δ in ppm): 4.24–4.17 (m, 2H, –**CH**$_2$–OC(O)–), 3.79–3.70 (m, 2H, –CH$_2$–**CH**$_2$–OC(O)–), 3.58 (s, 4H, –O–**CH**$_2$–**CH**$_2$–O– in the PEO repeating units), 3.53–3.42 (m, 2H, –**CH**$_2$–CH(CH$_3$)– in PPO repeating units), 3.36–3.28 (m, 2H, –**CH**$_2$–CH(CH$_3$)– in PPO repeating units), 2.75–2.68 (m, 2H, –**CH**$_2$–CH$_2$–SH), 2.65–2.58 (m, 2H, –CH$_2$–**CH**$_2$–SH), 1.62 (t, 1H, –**SH**), 1.10–1.03 (m, 3H, –O–CH$_2$–CH(**CH**$_3$)– in PPO repeating units).

FT-IR: v (cm^{-1}): 1740 (C=O ester bond).
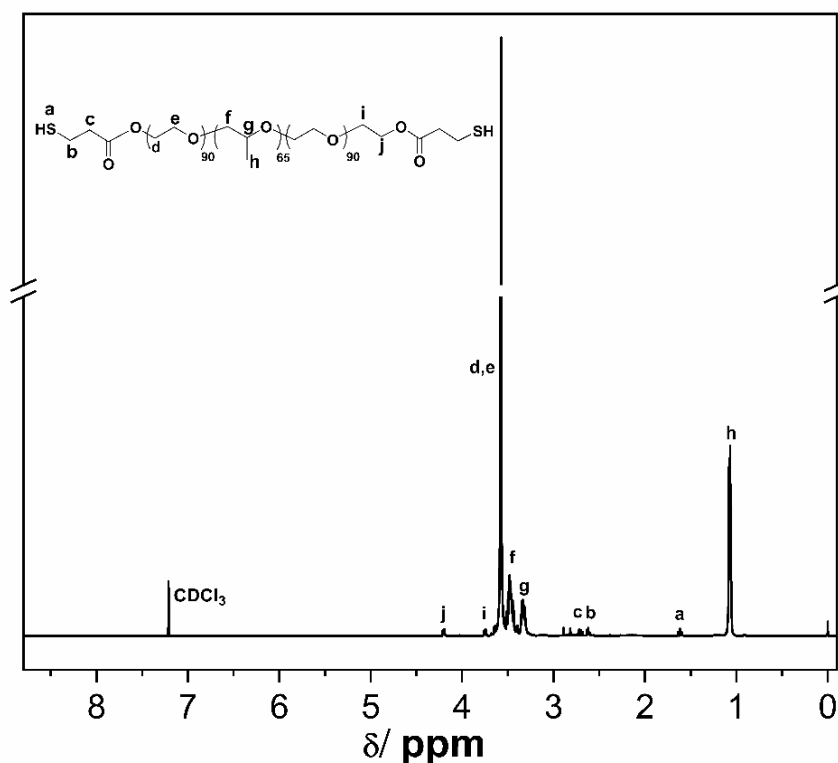
Figure 8.3.13. ^{1}H-NMR spectra (400 MHz) of thiol-terminated Pluronic F127 (PF127-SH) in CDCl$_3$.

8.3.14 Synthesis of 2,2′-(1,4-phenylene)-bis[4-mercaptan-1,3,2-dioxaborolane] (BDB)
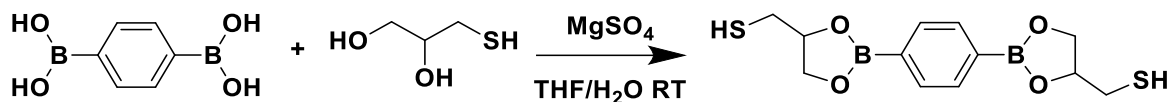
Scheme 8.3.14. The synthesis route of 2,2'-(1,4-phenylene)-bis [4-mercaptan-1,3,2-dioxaborolane] (BDB).

1,4-phenylenediboronic acid (3 g, 18.1 mmol, 1.00 eq.), 1-thioglycerol (4.01 g, 37.0 mmol, 2.04 eq.) and magnesium sulfate (5 g, 41.5 mmol, 2.3 eq.) were dissolved in the mixed solvent of 80 mL of tetrahydrofuran and 0.1 mL of water. The mixture was stirred at room temperature overnight, filtered and then concentrated under reduced pressure. The final product was obtained as white solid after being repeatedly washed with DCM and dried under vacuum oven at 45 °C (5.0 g, yield: 88%).

^{1}H NMR (400 MHz, CDCl$_3$, δ in ppm): 7.75 (d, 4H, **Ar**), 4.66 (dq, 2H, –O–C**H**(CH$_2$)–), 4.41 (dd, 2H, –O–CH(C**H**$_2$)–O–), 4.10 (dd, 2H, –O–CH(C**H**$_2$)–O–), 2.73 (dd, 4H, –O–CH(C**H**$_2$)–SH), 1.41 (t, 2H, –S**H**).
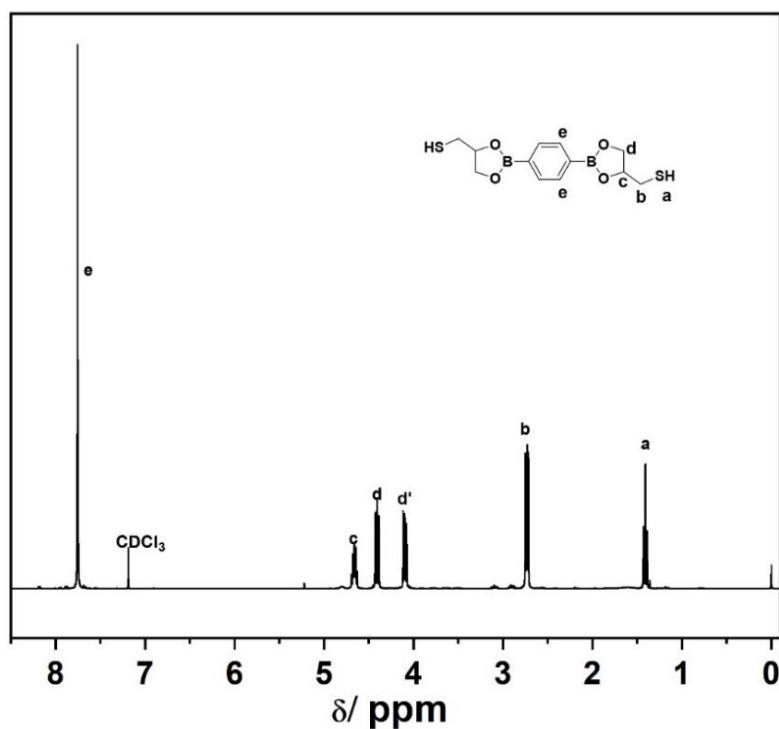
Figure 8.3.14. ^{1}H-NMR spectra (400 MHz) of 2,2'-(1,4-phenylene)-bis [4-mercaptan- 1,3,2-dioxaborolane] (BDB) in CDCl$_3$.

8.3.15 Synthesis of (pentafluorophenyl)methyl acetate (PFPMA)
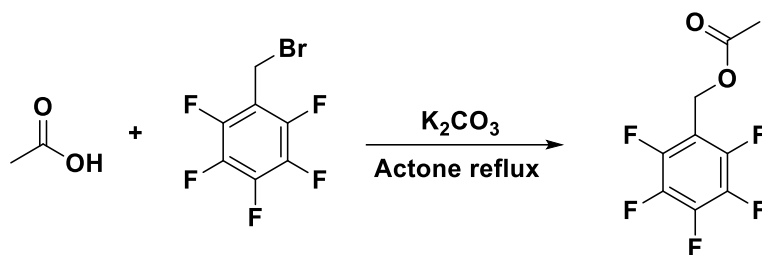
Scheme 8.3.15. The synthesis route of (Pentaflurophenyl)methyl acetate (PFPMA).

Acetic acid (0.54 g, 9 mmol, 3.2 eq), pentafluorobenzyl bromide (0.73 g, 2.8 mmol, 1.0 eq) and potassium carbonate (0.83 g, 6 mmol, 2.1 eq) were dissolved into 50 mL of anhydrous acetone. Afterwards, the mixture was refluxed at 60 °C for 24 h, filtrated and condensed in a rotavaporator. The crude product was then re-dissolved into 30 mL of *n*-hexane, and washed by water (three times, 10 mL for each). The final product was obtained as pale yellow liquid after removing *n*-hexane under reduced pressure.

^{1}H NMR (400 MHz, CDCl$_3$, δ in ppm): 5.12 (t, 2H, $-$**CH$_2$**$-$C$_6$F$_5$), 2.06 $-$ 1.91 (m, 3H, $-$O$-$C(O)**CH$_3$**).

^{19}F-NMR (376 MHz, CDCl$_3$, δ in ppm): -141.96 $-$ -142.37 (*ortho*), -152.87 (*para*), -161.71 $-$ -162.06 (*meta*).
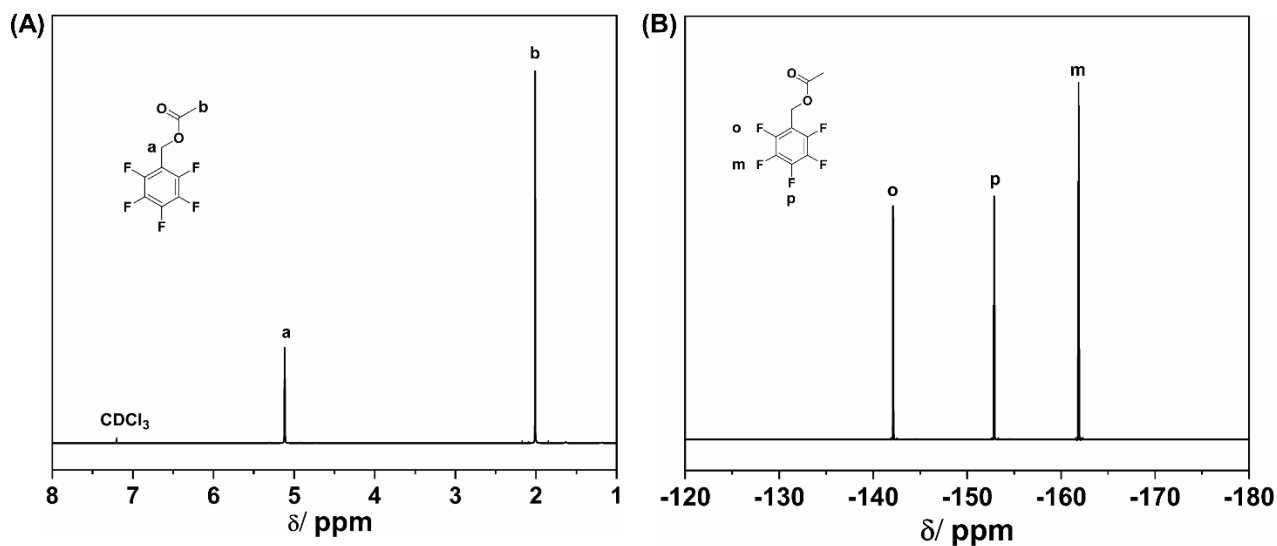
Figure 8.3.15. (A) ^{1}H-NMR spectra (400 MHz) and (B) ^{19}F-NMR spectra (376 MHz) of (Pentafluorophenyl)methyl acetate (PFPMA) in CDCl$_3$.

8.3.16 Synthesis of tris((perfluorophenyl)methyl) propane-1,2,3-tricarboxylate (3PFB)
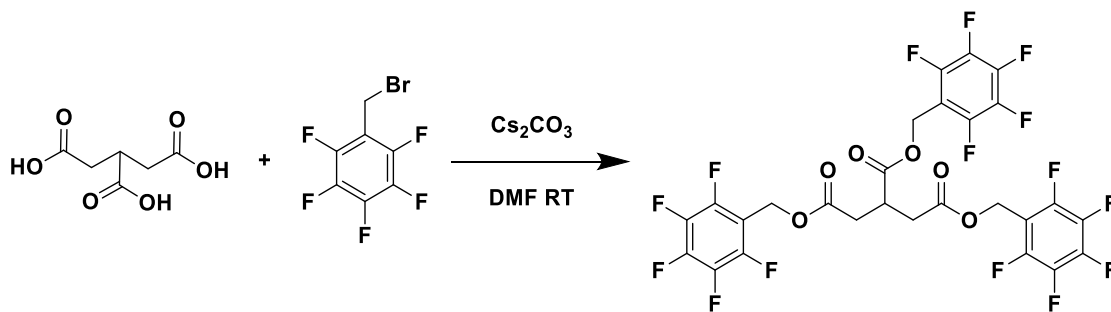
Scheme 8.3.16. The synthesis route of (tris((perfluorophenyl)methyl) propane-1,2,3-tricarboxylate (3PFB).

Cs_2CO_3 (17.5 mmol, 6.174 g, 5.00 eq.) was dispersed in dry 12 ml of dry DMF and degassed with nitrogen for 30 min. Afterwards, tricarballylic acid (3.50 mmol, 0.616 g, 1.00 eq.) was dissolved in 2 mL of dry DMF and added into the mixture under nitrogen atmosphere. After degassing for another 30 minute, 2,3,4,5,6-pentafluorobenzyl bromide (11.3 mmol, 1.7 mL, 3.2 eq.) was added and the whole mixture was stirred overnight at room temperature. Afterwards, the mixture was filtered, diluted with 20 mL water and extracted with DCM (3 times, 20 mL for each). The combined organic phases were washed by saturated saline (three times, 20 mL each), dried over anhydrous $MgSO_4$ and then condensed under reduced pressure. The crude product was purified by column chromatography (gradient DCM) to provide final product as a clear oil (1.5 g, yield: 60%).

^{1}H NMR (400 MHz, CDCl$_3$, δ in ppm): 5.28 – 5.16 (m, 6H, –O–**CH**$_2$), 3.29 (p, 1H, **CH**), 2.80 (dd, 2H, –**CH**$_2$–COO), 2.66 (dd, 2H, –**CH**$_2$–COO).

^{19}F NMR (376 MHz, CDCl$_3$, δ in ppm): -142.00 (m, 2F, *ortho*), -152.20 (m,1F, *para*), -161.54 (m, 2F, *meta*).
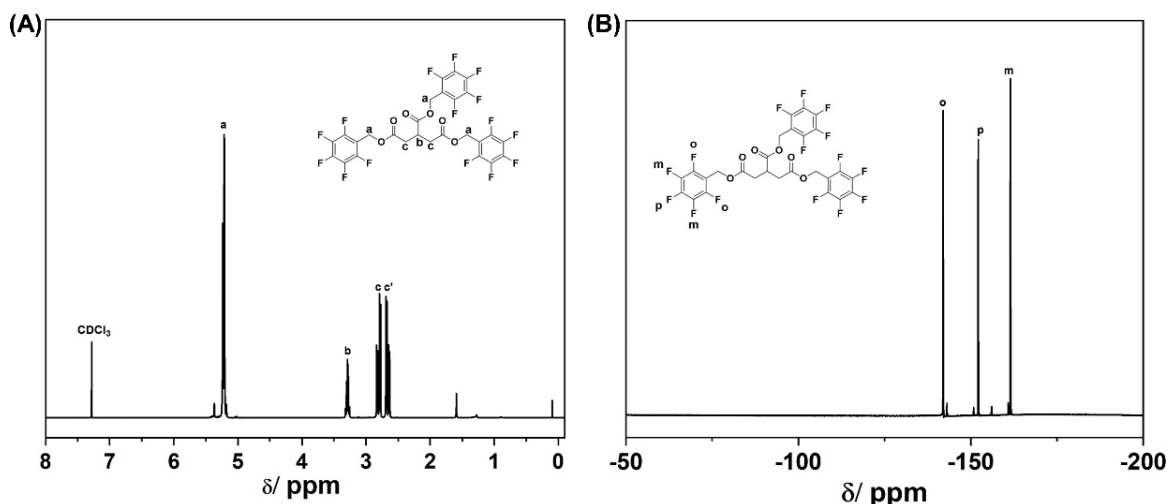
Figure 8.3.16. (A) ^{1}H-NMR spectra (400 MHz) and (B) ^{19}F-NMR spectra (377 MHz) of tris((perfluorophenyl)methyl) propane-1,2,3-tricarboxylate (3PFB) in CDCl$_3$.

8.4 Fabrication procedures

8.4.1 Preparation of Py-*β*-CD/SWCNTs hybrids (Chapter 4)

Py-*β*-CD (50 mg) and SWCNTs (10 mg) were dissolved in 20 mL 0.1M NaOH, followed by sonication for 4 h. The supernatant was then loaded into a dialysis bag (MWCO 8000), dialyzed against 0.1 M NaOH for a week to remove excess free Py-*β*-CD. The Py-*β*-CD/SWCNTs hybrids were obtained after lyophilization for two days.

8.4.2 Preparation of hydrogels based on non-covalent interactions (Chapter 4)

Py-*β*-CD/SWCNTs hybrids (10 mg) and Polycations (poly((3-Acrylamidopropyl) trimethylammonium chloride) (PAMPT)) with adamantane end-group (200 mg) were dissolved into 2 mL DI water, and stirred overnight to prepare the inclusion complexes between cyclodextrin an adamantane moieties. After that, anionic monomer sodium 4-vinylbenzenesulfonate (NaSS, 1 g) was added into the mixture solution, followed by the in-situ polymerization initiated with ammonium persulfate (APS, 20 mg) and accelerator *N*,*N*,*N′*,*N′*-tetramethylethylenediamine (TMEDA, 0.1 mL). Hydrogel was formed within 5 minutes at room temperature under vigorous stirring.

8.4.3 Preparation of hydrogels based on boronate ester bonds (Chapter 4)

100 mg copolymer P2 (containing ~ 11.6 mg, 0.03 mmol *N*-(6-aminohexyl)-4-(pyren-1-yl) butanamide (APB)) was dissolved in 0.9 mL purified DI water in a vial with different amount of SWCNTs (3, 6, 9 and 12 mg, respectively). The vial was sonicated for 20 min to evenly disperse CNTs in the aqueous media. Afterwards, 600 mg of PVA solution (10 wt%) was added, and the mixture was stirred heavily until gelation was observed. The final concentration of SWCNTs was 2, 4, 6, and 8 mg/mL, responsively.

8.4.4 Complex hyperbranched sample preparation for ^{1}H-NMR (Chapter 5)

A dilute solution of P(DMA-*co*-EDA-*co*-DHA) (P3, 20 mg, containing 0.006 mmol CH$_2$=CH–) and PF127-SH (38 mg, containing 0.0061 mmol SH) was prepared by dissolving the polymers into 1

mL DI water, then borax solution (0.1M, 0.024 mL) was added dropwise into the mixture solution. The whole mixture solution was stirred for 30 minutes at room temperature and then reaction was quenched immediately in liquid nitrogen. The solution was lyophilized for 24 h, afterwards, 20 mg of the mixture was withdrawn and dissolved into $CDCl_3$ to perform ^{1}H-NMR measurements.

8.4.5 Preparation of hydrogels under the catalyst of borax (Chapter 5)

Hydrophilic copolymer (P(DMA-co-EDA-co-DHA)) (P3) (100 mg, containing around 0.03 mmol $CH_2=CH-$ and 0.07 mmol 1,2-diols groups) and PF127-SH (190 mg, containing 0.03 mmol –SH group) were dissolved in 1 mL ice cold water to form a homogenous solution. Afterwards, 0.12 mL of 0.1 mol/L borax solution was added dropwise into the polymer solution under vigorous stirring at room temperature. Final hydrogels with 20 wt% solid content formed within two minutes. Other hydrogel samples were prepared through the same procedure.

8.4.6 General procedure for the PFTR model reactions (Chapter 6)

PFPMA (52.8 mg, 2.2 mmol, 2.2 eq.) and the base (DBU, TBD or DBN, 2.2 mmol, 2.2 eq.) were dissolved in 0.3 mL THF-d_8 to form mixed solution, then BDB (31.0 mg, 1.0 mmol, 1.0 eq.) dissolved in 0.1 mL THF-d_8 was added dropwise into the mixture. The whole mixture was then utilized for further characterizations.

8.4.7 Synthesis of cross-linked network via PFTR reaction (Chapter 6)

In a vial, 3PFB (72 mg, 0.3 mmol in PFB, 1.0 eq.) and DBU (49.5 μL, 0.31 mmol, 1.1 eq.) were dissolved in 0.2 mL THF. Afterwards, the cross-linker BDB (72 mg, 0.45 mmol in thiol, 1.5 eq.) was dissolved in 0.1 mL THF and added dropwise into the aforementioned solution. The organic gel formed immediately after the addition of the BDB solution, hence requiring adequate stirring. The fresh gel was removed from the vial, washed with THF and then dried under vacuum oven at 45 °C.

8.4.8 Hot-press for the reprocessing procedure (Chapter 6)

Hot-processing was operated on a HKP300 hot presser. Samples were first cut into small pieces or grind into a power, and then loaded into a I.D. = 13 mm mold connected with a vacuum pump. The sample was finally compressed into 1 mm thick disks at 60 °C under a pressure of 10 MPa for 10 min.

References

1   H. Staudinger, *Berichte der deutschen chemischen Gesellschaft (A and B Series)*, 1920, **53**, 1073-1085.

2   R. Geyer, J. R. Jambeck and K. L. Law, *Sci. Adv.*, 2017, **3**, e1700782.

3   Y. Yang and M. W. Urban, *Chem. Soc. Rev.*, 2013, **42**, 7446-7467.

4   M. D. Hager, *Handbook of Solid State Chemistry*, 2017, 201-225.

5   R. P. Wool, *Soft Matter*, 2008, **4**, 400-418.

6   F. Herbst, D. Döhler, P. Michael and W. H. Binder, *Macromol. Rapid Commun.*, 2013, **34**, 203-220.

7   Y. Yang, X. Ding and M. W. Urban, *Prog. Polym. Sci.*, 2015, **49**, 34-59.

8   D. L. Taylor and M. in het Panhuis, *Adv. Mater.*, 2016, **28**, 9060-9093.

9   J. A. Syrett, C. R. Becer and D. M. Haddleton, *Polym. Chem.*, 2010, **1**, 978-987.

10   J. M. Lehn, *Prog. Polym. Sci.*, 2005, **30**, 814-831.

11   J. M. Lehn, *Chem. Soc. Rev.*, 2007, **36**, 151-160.

12   Z. Wei, J. H. Yang, J. Zhou, F. Xu, M. Zrínyi, P. H. Dussault, Y. Osada and Y. M. Chen, *Chem. Soc. Rev.*, 2014, **43**, 8114-8131.

13   L. Brunsveld, B. Folmer, E. W. Meijer and R. Sijbesma, *Chem. Rev.*, 2001, **101**, 4071-4098.

14   J. W. Steed, D. R. Turner and K. Wallace, *Core concepts in supramolecular chemistry and nanochemistry*, 2007.

15   The Nobel Prize in Chemistry 1987. NobelPrize.org. Nobel Media AB 2020. Wed. 23 Dec 2020., (https://www.nobelprize.org/prizes/chemistry/1987/summary/).

16   A. J. Savyasachi, O. Kotova, S. Shanmugaraju, S. J. Bradberry, G. M. Ó'Máille and T. Gunnlaugsson, *Chem*, 2017, **3**, 764-811.

17   J. C. G. Bünzli, *Chem. Rev.*, 2010, **110**, 2729-2755.

18   A. Bom, M. Bradley, K. Cameron, J. K. Clark, J. van Egmond, H. Feilden, E. J. MacLean, A. W. Muir, R. Palin and D. C. Rees, *Angew. Chem. Int. Ed.*, 2002, **41**, 265-270.

19   Y. Yang and M. W. Urban, *Adv. Mater. Interfaces*, 2018, **5**, 1800384.

20   Y. Jin, C. Yu, R. J. Denman and W. Zhang, *Chem. Soc. Rev.*, 2013, **42**, 6634-6654.

21   S. J. Rowan, S. J. Cantrill, G. R. Cousins, J. K. Sanders and J. F. Stoddart, *Angew. Chem. Int. Ed.*, 2002, **41**, 898-952.

22   X. Chen, M. A. Dam, K. Ono, A. Mal, H. Shen, S. R. Nutt, K. Sheran and F. Wudl, *Science*, 2002, **295**, 1698-1702.

23   K. K. Oehlenschlaeger, J. O. Mueller, J. Brandt, S. Hilf, A. Lederer, M. Wilhelm, R. Graf, M. L. Coote, F. G. Schmidt and C. Barner-Kowollik, *Adv. Mater.*, 2014, **26**, 3561-3566.

24   Y. Lu and Z. Guan, *J. Am. Chem. Soc.*, 2012, **134**, 14226-14231.

25   M. E. Belowich and J. F. Stoddart, *Chem. Soc. Rev.*, 2012, **41**, 2003-2024.

26   H. Wang and S. C. Heilshorn, *Adv. Mater.*, 2015, **27**, 3717-3736.

27   S. Mukherjee, M. R. Hill and B. S. Sumerlin, *Soft matter*, 2015, **11**, 6152-6161.

28   Z. Zhang, C. He and X. Chen, *Mater. Chem. Front.*, 2018, **2**, 1765-1778.

29   J. Kalia and R. T. Raines, *Angew. Chem. Int. Ed.*, 2008, **47**, 7523-7526.

30   H. Ying, Y. Zhang and J. Cheng, *Nat. Commun.*, 2014, **5**, 1-9.

31   Y. Zhang, H. Ying, K. R. Hart, Y. Wu, A. J. Hsu, A. M. Coppola, T. A. Kim, K. Yang, N. R. Sottos and S. R. White, *Adv. Mater.*, 2016, **28**, 7646-7651.

32   R. C. Brachvogel and M. von Delius, *Chem. Sci.*, 2015, **6**, 1399-1403.

33   J. Otera, *Chem. Rev.*, 1993, **93**, 1449-1470.

34   R. C. Brachvogel and M. von Delius, *Eur. J. Org. Chem.*, 2016, **2016**, 3662-3670.

35   S. P. Black, J. K. Sanders and A. R. Stefankiewicz, *Chem. Soc. Rev.*, 2014, **43**, 1861-1872.

36   B. Marco Dufort and M. Tibbitt, *Mater. Today Chem.*, 2019, **12**, 16-33.

37   G. Fang, H. Wang, Z. Bian, J. Sun, A. Liu, H. Fang, B. Liu, Q. Yao and Z. Wu, *RSC Adv.*, 2018, **8**, 29400-29427.

38   S. b. Delpierre, B. Willocq, G. Manini, V. Lemaur, J. Goole, P. Gerbaux, J. r. m. Cornil, P. Dubois and J. M. Raquez, *Chem. Mater.*, 2019, **31**, 3736-3744.

39   A. P. Bapat, B. S. Sumerlin and A. Sutti, *Mater. Horiz.*, 2020, **7**, 694-714.

40   M. Podgórski, B. D. Fairbanks, B. E. Kirkpatrick, M. McBride, A. Martinez, A. Dobson, N. J. Bongiardina and C. N. Bowman, *Adv. Mater.*, 2020, **32**, 1906876.

41   B. Marco Dufort, R. Iten and M. W. Tibbitt, *J. Am. Chem. Soc.*, 2020, **142**, 15371-15385.

42   N. J. Van Zee and R. Nicolaÿ, *Prog. Polym. Sci.*, 2020, 101233.

43   M. Hayashi, *Polymers*, 2020, **12**, 1322.

44   G. M. Scheutz, J. J. Lessard, M. B. Sims and B. S. Sumerlin, *J. Am. Chem. Soc.*, 2019, **141**, 16181-16196.

45   D. Montarnal, M. Capelot, F. Tournilhac and L. Leibler, *Science*, 2011, **334**, 965-968.

46   S. Schäfer and G. Kickelbick, *Polymer*, 2015, **69**, 357-368.

47   H. Otsuka, *Polym. J.*, 2013, **45**, 879-891.

48   M. Z. Rong and M. Q. Zhang, *Polymer*, 2014, **55**, 1782-1791.

49   A. Takahashi, R. Goseki and H. Otsuka, *Angew. Chem. Int. Ed.*, 2017, **56**, 2016-2021.

50   B. Zhang, Z. A. Digby, J. A. Flum, P. Chakma, J. M. Saul, J. L. Sparks and D. Konkolewicz, *Macromolecules*, 2016, **49**, 6871-6878.

51   M. Capelot, D. Montarnal, F. Tournilhac and L. Leibler, *J. Am. Chem. Soc.*, 2012, **134**, 7664-7667.

52   F. I. Altuna, C. E. Hoppe and R. J. Williams, *Eur. Polym. J.*, 2019, **113**, 297-304.

53   M. Röttger, T. Domenech, R. van der Weegen, A. Breuillac, R. Nicolaÿ and L. Leibler, *Science*, 2017, **356**, 62-65.

54   F. Caffy and R. Nicolaÿ, *Polym. Chem.*, 2019, **10**, 3107-3115.

55   Y. Zuo, Z. Gou, C. Zhang and S. Feng, *Macromol. Rapid Commun.*, 2016, **37**, 1052-1059.

56   Y. Lu, F. Tournilhac, L. Leibler and Z. Guan, *J. Am. Chem. Soc.*, 2012, **134**, 8424-8427.

57   J. J. Lessard, L. F. Garcia, C. P. Easterling, M. B. Sims, K. C. Bentz, S. Arencibia, D. A. Savin and B. S. Sumerlin, *Macromolecules*, 2019, **52**, 2105-2111.

58   W. Denissen, G. Rivero, R. Nicolaÿ, L. Leibler, J. M. Winne and F. E. Du Prez, *Adv. Funct. Mater.*, 2015, **25**, 2451-2457.

59   J. S. Ishibashi and J. A. Kalow, *ACS Macro Lett.*, 2018, **7**, 482-486.

60   W. Zou, J. Dong, Y. Luo, Q. Zhao and T. Xie, *Adv. Mater.*, 2017, **29**, 1606100.

61   S. Wang and M. W. Urban, *Nat. Rev. Mater.*, 2020, **5**, 562-583.

62   B. J. Blaiszik, S. L. Kramer, S. C. Olugebefola, J. S. Moore, N. R. Sottos and S. R. White, *Annu. Rev. Mater. Sci.*, 2010, **40**, 179-211.

63   W. H. Binder, *Self-healing polymers*, 2013.

64   S. R. White, N. R. Sottos, P. H. Geubelle, J. S. Moore, M. R. Kessler, S. R. Sriram, E. N. Brown and S. Viswanathan, *Nature*, 2001, **409**, 794-797.

65   J. D. Rule, E. N. Brown, N. R. Sottos, S. R. White and J. S. Moore, *Adv. Mater.*, 2005, **17**, 205-208.

66   M. Kessler, N. R. Sottos and S. R. White, *Compos. Part A Appl. Sci. Manuf.*, 2003, **34**, 743-753.

67   K. S. Toohey, N. R. Sottos, J. A. Lewis, J. S. Moore and S. R. White, *Nat. Mater.*, 2007, **6**, 581-585.

68   C. J. Hansen, W. Wu, K. S. Toohey, N. R. Sottos, S. R. White and J. A. Lewis, *Adv. Mater.*, 2009, **21**, 4143-4147.

69   J. Dahlke, S. Zechel, M. D. Hager and U. S. Schubert, *Adv. Mater. Interfaces*, 2018, **5**, 1800051.

70   G. Zhang, T. Ngai, Y. Deng and C. Wang, *Macromol. Chem. Phys.*, 2016, **217**, 2172-2181.

71   L. Ouyang, C. B. Highley, C. B. Rodell, W. Sun and J. A. Burdick, *ACS Biomater. Sci. Eng.*, 2016, **2**, 1743-1751.

72   K. Liu, S. Zang, R. Xue, J. Yang, L. Wang, J. Huang and Y. Yan, *ACS Appl. Mater. Interfaces*, 2018, **10**, 4530-4539.

73   Y. Rao, A. Chortos, R. Pfattner, F. Lissel, Y. Chiu, V. Feig, J. Xu, T. Kurosawa, X. Gu and C. Wang, *J. Am. Chem. Soc.*, 2016, **138**, 6020-6027.

74   C. Li, C. Wang, C. Keplinger, J. Zuo, L. Jin, Y. Sun, P. Zheng, Y. Cao, F. Lissel and C. Linder, *Nat. Chem.*, 2016, **8**, 618-624.

75   Y. J. Tan, J. Wu, H. Li and B. C. Tee, *ACS Appl. Mater. Interfaces*, 2018, **10**, 15331-15345.

76   V. Can, Z. Kochovski, V. Reiter, N. Severin, M. Siebenbürger, B. Kent, J. Just, J. P. Rabe, M. Ballauff and O. Okay, *Macromolecules*, 2016, **49**, 2281-2287.

77   D. C. Tuncaboylu, A. Argun, M. Sahin, M. Sari and O. Okay, *Polymer*, 2012, **53**, 5513-5522.

78   T. L. Sun, T. Kurokawa, S. Kuroda, A. B. Ihsan, T. Akasaki, K. Sato, M. A. Haque, T. Nakajima and J. P. Gong, *Nat. Mater.*, 2013, **12**, 932-937.

79   W. Pu, F. Jiang, P. Chen and B. Wei, *Soft Matter*, 2017, **13**, 5645-5648.

80   T. Kakuta, Y. Takashima, M. Nakahata, M. Otsubo, H. Yamaguchi and A. Harada, *Adv. Mater.*, 2013, **25**, 2849-2853.

81   Z. Hu, D. Zhang, F. Lu, W. Yuan, X. Xu, Q. Zhang, H. Liu, Q. Shao, Z. Guo and Y. Huang, *Macromolecules*, 2018, **51**, 5294-5303.

82   K. Miyamae, M. Nakahata, Y. Takashima and A. Harada, *Angew. Chem. Int. Ed.*, 2015, **54**, 8984-8987.

83   L. Shi, P. Ding, Y. Wang, Y. Zhang, D. Ossipov and J. Hilborn, *Macromol. Rapid Commun.*, 2019, **40**, 1800837.

84   D. Mozhdehi, S. Ayala, O. R. Cromwell and Z. Guan, *J. Am. Chem. Soc.*, 2014, **136**, 16128-16131.

85   Z. Yang, F. Wang, C. Zhang, J. Li, R. Zhang, Q. Wu, T. Chen and P. Sun, *Polym. Chem.*, 2019, **10**, 3362-3370.

86   Y. Liu and T. Chuo, *Polym. Chem.*, 2013, **4**, 2194-2205.

87   P. Du, X. Liu, Z. Zheng, X. Wang, T. Joncheray and Y. Zhang, *RSC advances*, 2013, **3**, 15475-15482.

88   Z. Wei, J. H. Yang, X. J. Du, F. Xu, M. Zrinyi, Y. Osada, F. Li and Y. M. Chen, *Macromol. Rapid Commun.*, 2013, **34**, 1464-1470.

89   J. A. Yoon, J. Kamada, K. Koynov, J. Mohin, R. Nicolaÿ, Y. Zhang, A. C. Balazs, T. Kowalewski and K. Matyjaszewski, *Macromolecules*, 2012, **45**, 142-149.

90   J. Canadell, H. Goossens and B. Klumperman, *Macromolecules*, 2011, **44**, 2536-2541.

91   A. Rekondo, R. Martin, A. R. de Luzuriaga, G. Cabañero, H. J. Grande and I. Odriozola, *Mater. Horiz.*, 2014, **1**, 237-240.

92   C. Cheng, X. Zhang, Y. Meng, Z. Zhang, J. Chen and Q. Zhang, *Soft Matter*, 2017, **13**, 3003-3012.

93   J. Xu, Y. Liu and S. Hsu, *Molecules*, 2019, **24**, 3005.

94   J. Hu, R. Mo, X. Sheng and X. Zhang, *Polym. Chem.*, 2020, **11**, 2585-2594.

95   A. J. Amaral and G. Pasparakis, *Polym. Chem.*, 2017, **8**, 6464-6484.

96   F. Yu, X. Cao, J. Du, G. Wang and X. Chen, *ACS Appl. Mater. Interfaces*, 2015, **7**, 24023-24031.

97   Y. Guan and Y. Zhang, *Chem. Soc. Rev.*, 2013, **42**, 8106-8121.

98   D. G. Hall, *Boronic acids: preparation, applications in organic synthesis and medicine*, 2006.

99   W. L. Brooks and B. S. Sumerlin, *Chem. Rev.*, 2016, **116**, 1375-1397.

100   R. Martin and S. L. Buchwald, *Acc. Chem. Res.*, 2008, **41**, 1461-1473.

101   D. G. Hall, *Chem. Soc. Rev.*, 2019, **48**, 3475-3496.

102   S. D. Bull, M. G. Davidson, J. M. H. van den Elsen, J. S. Fossey, A. T. A. Jenkins, Y.-B. Jiang, Y. Kubo, F. Marken, K. Sakurai, J. Zhao and T. D. James, *Acc. Chem. Res.*, 2013, **46**, 312-326.

103   P. C. Trippier and C. McGuigan, *Med. Chem. Commun.*, 2010, **1**, 183-198.

104   J. N. Cambre and B. S. Sumerlin, *Polymer*, 2011, **52**, 4631-4643.

105   W. Yang, X. Gao and B. Wang, *Med Res Rev*, 2003, **23**, 346-368.

106   E. Aeridou, D. Díaz Díaz, C. Alemán and M. M. Pérez-Madrigal, *Biomacromolecules*, 2020, **21**, 3984-3996.

107   J. P. Lorand and J. O. EDWARDS, *J. Org. Chem.*, 1959, **24**, 769-774.

108   A. Pettignano, S. Grijalvo, M. Haering, R. Eritja, N. Tanchoux, F. Quignard and D. D. Díaz, *Chem. Commun.*, 2017, **53**, 3350-3353.

109   L. Bosch, T. Fyles and T. D. James, *Tetrahedron*, 2004, **60**, 11175-11190.

110   W. L. Brooks, C. C. Deng and B. S. Sumerlin, *ACS omega*, 2018, **3**, 17863-17870.

111   G. Wulff, M. Lauer and H. Böhnke, *Angew. Chem. Int. Ed.*, 1984, **23**, 741-742.

112   Y. Chen, D. Diaz-Dussan, D. Wu, W. Wang, Y. Peng, A. B. Asha, D. G. Hall, K. Ishihara and R. Narain, *ACS Macro Lett.*, 2018, **7**, 904-908.

113   Y. Chen, Z. Tan, W. Wang, Y. Peng and R. Narain, *Biomacromolecules*, 2018, **20**, 1028-1035.

114   Y. Chen, W. Wang, D. Wu, H. Zeng, D. G. Hall and R. Narain, *ACS Appl. Mater. Interfaces*, 2019, **11**, 44742-44750.

115   M. Shan, C. Gong, B. Li and G. Wu, *Polym. Chem.*, 2017, **8**, 2997-3005.

116   L. He, D. E. Fullenkamp, J. G. Rivera and P. B. Messersmith, *Chem. Commun.*, 2011, **47**, 7497-7499.

117   G. Springsteen and B. Wang, *Chem. Commun.*, 2001, 1608-1609.

118   X. Wu, Z. Li, X. Chen, J. S. Fossey, T. D. James and Y. Jiang, *Chem. Soc. Rev.*, 2013, **42**, 8032-8048.

119   F. Abdi, R. Michel, R. Poirot, M. Dakir, L. Sancey, V. Ravaine and R. Auzély-Velty, *Macromol. Rapid Commun.*, 2020, **41**, 2000213.

120   T. Figueiredo, V. Cosenza, Y. Ogawa, I. Jeacomine, A. Vallet, S. Ortega, R. Michel, J. D. Olsson, T. Gerfaud and J. G. Boiteau, *Soft Matter*, 2020, **16**, 3628-3641.

121   A. J. Amaral, M. Emamzadeh and G. Pasparakis, *Polym. Chem.*, 2018, **9**, 525-537.

122   C. C. Deng, W. L. Brooks, K. A. Abboud and B. S. Sumerlin, *ACS Macro Lett.*, 2015, **4**, 220-224.

123   S. Wu, H. Yang, S. Huang and Q. Chen, *Macromolecules*, 2020, **53**, 1180-1190.

124   A. Breuillac, A. Kassalias and R. Nicolaÿ, *Macromolecules*, 2019, **52**, 7102-7113.

125   J. J. Cash, T. Kubo, D. J. Dobbins and B. S. Sumerlin, *Polym. Chem.*, 2018, **9**, 2011-2020.

126   J. J. Cash, T. Kubo, A. P. Bapat and B. S. Sumerlin, *Macromolecules*, 2015, **48**, 2098-2106.

127   F. Meng, M. O. Saed and E. M. Terentjev, *Macromolecules*, 2019, **52**, 7423-7429.

128   O. R. Cromwell, J. Chung and Z. Guan, *J. Am. Chem. Soc.*, 2015, **137**, 6492-6495.

129   C. Kim, H. Ejima and N. Yoshie, *J. Mater. Chem. A*, 2018, **6**, 19643-19652.

130   R. G. Ricarte, F. Tournilhac, M. Cloître and L. Leibler, *Macromolecules*, 2020, **53**, 1852-1866.

131   M. Nakahata and S. Sakai, *Chemnanomat*, 2019, **5**, 141-151.

132   M. Vazquez-Gonzalez and I. Willner, *Angew. Chem. Int. Ed.*, 2020, **59**, 15342-15377.

133   Y. Chen, D. Diaz-Dussan, D. Wu, W. Wang, Y.-Y. Peng, A. B. Asha, D. G. Hall, K. Ishihara and R. Narain, *ACS Macro Lett.*, 2018, **7**, 904-908.

134   H. Meng, J. Zheng, X. Wen, Z. Cai, J. Zhang and T. Chen, *Macromol. Rapid Commun.*, 2015, **36**, 533-537.

135   T. Figueiredo, J. Jing, I. Jeacomine, J. Olsson, T. Gerfaud, J. G. Boiteau, C. Rome, C. Harris and R. Auzély-Velty, *Biomacromolecules*, 2019, **21**, 230-239.

136   G. Cai, J. Wang, K. Qian, J. Chen, S. Li and P. S. Lee, *Adv. Sci.*, 2017, **4**, 1600190.

137   G. Wu, K. Jin, L. Liu and H. Zhang, *Soft Matter*, 2020, **16**, 3319-3324.

138   D. Wei, H. Wang, J. Zhu, L. Luo, H. Huang, L. Li and X. Yu, *Macromol Mater Eng*, 2020, **305**, 2000018.

139   M. Liao, P. Wan, J. Wen, M. Gong, X. Wu, Y. Wang, R. Shi and L. Zhang, *Adv. Funct. Mater.*, 2017, **27**, 1703852.

140   S. W. Sinton, *Macromolecules*, 1987, **20**, 2430-2441.

141   H. An, Y. Bo, D. Chen, Y. Wang, H. Wang, Y. He and J. Qin, *RSC Advances*, 2020, **10**, 11300-11310.

142   W. Li, F. Gao, X. Wang, N. Zhang and M. Ma, *Angew. Chem.*, 2016, **128**, 9342-9347.

143   C. N. Bowman and C. J. Kloxin, *Angew. Chem. Int. Ed.*, 2012, **51**, 4272-4274.

144   C. J. Kloxin and C. N. Bowman, *Chem. Soc. Rev.*, 2013, **42**, 7161-7173.

145   K. Matyjaszewski, *Overview: Fundamentals of controlled/living radical polymerization*, 1998.

146   W. A. Braunecker and K. Matyjaszewski, *Prog. Polym. Sci.*, 2007, **32**, 93-146.

147   K. Parkatzidis, H. S. Wang, N. P. Truong and A. Anastasaki, *Chem*, 2020, **6**, 1575-1588.

148   K. Matyjaszewski and T. P. Davis, *Handbook of radical polymerization*, John Wiley & Sons, 2003.

149   J. Nicolas, Y. Guillaneuf, C. Lefay, D. Bertin, D. Gigmes and B. Charleux, *Prog. Polym. Sci.*, 2013, **38**, 63-235.

150   L. Tebben and A. Studer, *Angew. Chem. Int. Ed.*, 2011, **50**, 5034-5068.

151   J. Wang and K. Matyjaszewski, *J. Am. Chem. Soc.*, 1995, **117**, 5614-5615.

152   M. Kato, M. Kamigaito, M. Sawamoto and T. Higashimura, *Macromolecules*, 1995, **28**, 1721-1723.

153   K. Matyjaszewski and J. Xia, *Chem. Rev.*, 2001, **101**, 2921-2990.

154   M. Kamigaito, T. Ando and M. Sawamoto, *Chem. Rev.*, 2001, **101**, 3689-3746.

155   J. Xia, X. Zhang and K. Matyjaszewski, *The Effect of Ligands on Copper-Mediated Atom Transfer Radical Polymerization*, 2000.

156   D. J. Siegwart, J. K. Oh and K. Matyjaszewski, *Prog. Polym. Sci.*, 2012, **37**, 18-37.

157   J. Chiefari, Y. Chong, F. Ercole, J. Krstina, J. Jeffery, T. P. Le, R. T. Mayadunne, G. F. Meijs, C. L. Moad and G. Moad, *Macromolecules*, 1998, **31**, 5559-5562.

158   H. Mori, in *Encyclopedia of Polymeric Nanomaterials*, 2015, pp. 1148-1155.

159   H. Willcock and R. K. O'Reilly, *Polym. Chem.*, 2010, **1**, 149-157.

160   G. Moad, E. Rizzardo and S. H. Thang, *Aust. J. Chem.*, 2005, **58**, 379-410.

161   G. Moad, E. Rizzardo and S. H. Thang, *Polymer*, 2008, **49**, 1079-1131.

162   M. A. Gauthier, M. I. Gibson and H. A. Klok, *Angew. Chem. Int. Ed.*, 2009, **48**, 48-58.

163   H. Staudinger, *Nobel Lecture*, 1953, 397-419.

164   K. A. Günay, P. Theato and H. A. Klok, *Functional Polymers by Post-Polymerization Modification*, 2013, 1-44.

165   A. Das and P. Theato, *Chem. Rev.*, 2016, **116**, 1434-1495.

166   R. Kakuchi and P. Theato, *ACS Macro Lett.*, 2014, **3**, 329-332.

167   W. H. Binder and R. Sachsenhofer, *Macromol. Rapid Commun.*, 2007, **28**, 15-54.

168   J. F. Lutz, *Angew. Chem. Int. Ed.*, 2007, **46**, 1018-1025.

169   D. J. Hall, H. M. Van Den Berghe and A. P. Dove, *Polym. Int.*, 2011, **60**, 1149-1157.

170   S. Agar, E. Baysak, G. Hizal, U. Tunca and H. Durmaz, *J Polym Sci A Polym Chem*, 2018, **56**, 1181-1198.

171   H. G. Batz, G. Franzmann and H. Ringsdorf, *Die Makromolekulare Chemie: Macromolecular Chemistry and Physics*, 1973, **172**, 27-47.

172   P. Ferruti, A. Bettelli and A. Feré, *Polymer*, 1972, **13**, 462-464.

173   W. Chiang, Y. Hsu, T. Lou, C. Chern and H. Chiu, *Macromolecules*, 2009, **42**, 3611-3619.

174   R. Kakuchi and P. Theato, *Functional polymers by post-polymerization modification*, 2013, 45-64.

175   M. Eberhardt, R. Mruk, R. Zentel and P. Théato, *Eur. Polym. J.*, 2005, **41**, 1569-1575.

176   H. Gaballa, S. Lin, J. Shang, S. Meier and P. Theato, *Polym. Chem.*, 2018, **9**, 3355-3358.

177   P. Schattling, F. D. Jochum and P. Theato, *Polym. Chem.*, 2014, **5**, 25-36.

178   S. Lin, J. Shang, X. Zhang and P. Theato, *Macromol. Rapid Commun.*, 2018, **39**, 1700313.

179   H. Gaballa and P. Theato, *Biomacromolecules*, 2019, **20**, 871-881.

180   S. Lin, J. Shang and P. Theato, *ACS Macro Lett.*, 2018, **7**, 431-436.

181   X. Huang, H. Mutlu and P. Theato, *Adv. Mater. Interfaces*, 2020, **7**, 2000101.

182   H. Jo, N. Haberkorn, J. A. Pan, M. Vakili, K. Nielsch and P. Theato, *Langmuir*, 2016, **32**, 6437-6444.

183   A. Das and P. Theato, *Macromolecules*, 2015, **48**, 8695-8707.

184   E. Baumgarten and C. R. Hauser, *J. Am. Chem. Soc.*, 1944, **66**, 1037-1038.

185   C. E. Hoyle and C. N. Bowman, *Angew. Chem. Int. Ed.*, 2010, **49**, 1540-1573.

186   C. E. Hoyle, A. B. Lowe and C. N. Bowman, *Chem. Soc. Rev.*, 2010, **39**, 1355-1387.

187   S. P. Koo, M. M. Stamenović, R. A. Prasath, A. J. Inglis, F. E. Du Prez, C. Barner-Kowollik, W. Van Camp and T. Junkers, *J. Polym. Sci., Part A: Polym. Chem.*, 2010, **48**, 1699-1713.

188   A. K. Sinha and D. Equbal, *Asian J. Org. Chem.*, 2019, **8**, 32-47.

189   D. P. Nair, M. Podgórski, S. Chatani, T. Gong, W. Xi, C. R. Fenoli and C. N. Bowman, *Chem. Mater.*, 2014, **26**, 724-744.

190   J. Engelke and V. X. Truong, *Polym. Chem.*, 2020, **11**, 7015-7019.

191   F. Cavalli, H. Mutlu, S. O. Steinmueller and L. Barner, *Polym. Chem.*, 2017, **8**, 3778-3782.

192   G. Delaittre and L. Barner, *Polym. Chem.*, 2018, **9**, 2679-2684.

193   X. Li, X. Huang, H. Mutlu, S. Malik and P. Theato, *Soft Matter*, 2020, **16**, 10969-10976.

194   G. Huang, F. Li, X. Zhao, Y. Ma, Y. Li, M. Lin, G. Jin, T. J. Lu, G. M. Genin and F. Xu, *Chem. Rev.*, 2017, **117**, 12764-12850.

195   J. Li, L. Mo, C. Lu, T. Fu, H. Yang and W. Tan, *Chem. Soc. Rev.*, 2016, **45**, 1410-1431.

196   P. Li, Y. F. Poon, W. Li, H. Zhu, S. H. Yeap, Y. Cao, X. Qi, C. Zhou, M. Lamrani and R. W. Beuerman, *Nat. Mater.*, 2011, **10**, 149-156.

197   T. Distler and A. R. Boccaccini, *Acta Biomater.*, 2020, **101**, 1-13.

198   L. Li, L. Pan, Z. Ma, K. Yan, W. Cheng, Y. Shi and G. Yu, *Nano Lett.*, 2018, **18**, 3322-3327.

199   J. Shang, X. Le, J. Zhang, T. Chen and P. Theato, *Polym. Chem.*, 2019, **10**, 1036-1055.

200   C. Yang, Z. Liu, C. Chen, K. Shi, L. Zhang, X. Ju, W. Wang, R. Xie and L. Chu, *ACS Appl. Mater. Interfaces*, 2017, **9**, 15758-15767.

201   Z. Lei, Q. Wang, S. Sun, W. Zhu and P. Wu, *Adv. Mater.*, 2017, **29**, 1700321.

202   S. Lee, A. Reuveny, J. Reeder, S. Lee, H. Jin, Q. Liu, T. Yokota, T. Sekitani, T. Isoyama and Y. Abe, *Nat. Nanotechnol.*, 2016, **11**, 472.

203   E. Fantino, A. Chiappone, I. Roppolo, D. Manfredi, R. Bongiovanni, C. F. Pirri and F. Calignano, *Adv. Mater.*, 2016, **28**, 3712-3717.

204   L. Han, K. Liu, M. Wang, K. Wang, L. Fang, H. Chen, J. Zhou and X. Lu, *Adv. Funct. Mater.*, 2018, **28**, 1704195.

205   P. Li, Z. Jin, L. Peng, F. Zhao, D. Xiao, Y. Jin and G. Yu, *Adv. Mater.*, 2018, **30**, 1800124.

206   F. H. Gojny, M. H. Wichmann, B. Fiedler and K. Schulte, *Compos. Sci. Technol.*, 2005, **65**, 2300-2313.

207   Y. Huang, Y. Zheng, W. Song, Y. Ma, J. Wu and L. Fan, *Compos. Part A Appl. Sci. Manuf.*, 2011, **42**, 1398-1405.

208   Y. S. Song and J. R. Youn, *Carbon*, 2005, **43**, 1378-1385.

209   K. Balasubramanian and M. Burghard, *J. Mater. Chem.*, 2008, **18**, 3071-3083.

210   T. Fujigaya and N. Nakashima, *Sci Technol Adv Mater*, 2015, **16**, 024802.

211   K. C. Etika, F. D. Jochum, M. A. Cox, P. Schattling, P. Theato and J. C. Grunlan, *Macromolecules*, 2010, **43**, 9447-9453.

212   C. Kanimozhi, M. J. Shea, J. Ko, W. Wei, P. Huang, M. S. Arnold and P. Gopalan, *Macromolecules*, 2019, **52**, 4278-4286.

213   S. Brahmachari, D. Das, A. Shome and P. K. Das, *Angew. Chem.*, 2011, **123**, 11439-11443.

214   B. K. Billing, P. K. Agnihotri and N. Singh, *Analyst*, 2018, **143**, 3343-3352.

215   K. Kataoka, H. Miyazaki, T. Okano and Y. Sakurai, *Macromolecules*, 1994, **27**, 1061-1062.

216   X. Li, H. Mutlu, C. Fengler, M. Wilhelm and P. Theato, *Polym. Chem.*, 2021, **12**, 361-369.

217   D. L. Elbert, A. B. Pratt, M. P. Lutolf, S. Halstenberg and J. A. Hubbell, *J. Controlled Release*, 2001, **76**, 11-25.

218   K. C. Koehler, K. S. Anseth and C. N. Bowman, *Biomacromolecules*, 2013, **14**, 538-547.

219   L. He, D. Szopinski, Y. Wu, G. A. Luinstra and P. Theato, *ACS Macro Lett.*, 2015, **4**, 673-678.

220   I. Jeon, J. Cui, W. R. Illeperuma, J. Aizenberg and J. J. Vlassak, *Adv. Mater.*, 2016, **28**, 4678-4683.

221   P. Wang, G. Deng, L. Zhou, Z. Li and Y. Chen, *ACS Macro Lett.*, 2017, **6**, 881-886.

222   L. Arens and M. Wilhelm, *Macromol. Chem. Phys.*, 2019, **220**, 1900093.

223   Z. Liu and P. Yao, *Polym. Chem.*, 2014, **5**, 1072-1081.

224   Y. Sun, G. Gao, G. Du, Y. Cheng and J. Fu, *ACS Macro Lett.*, 2014, **3**, 496-500.

225   J. Qu, X. Zhao, Y. Liang, T. Zhang, P. X. Ma and B. Guo, *Biomaterials*, 2018, **183**, 185-199.

226   X. Yu, Z. Qin, H. Wu, H. Lv and X. Yang, *Macromolecules*, 2019, **52**, 1249-1256.

227   A. Das and P. Theato, *Macromolecules*, 2015, **48**, 8695-8707.

228   E. Pezron, A. Ricard, F. Lafuma and R. Audebert, *Macromolecules*, 1988, **21**, 1121-1125.

229   L. Xu, C. Wang, Y. Cui, A. Li, Y. Qiao and D. Qiu, *Sci. Adv.*, 2019, **5**, eaau3442.

230   Y. Chen, W. Qian, R. Chen, H. Zhang, X. Li, D. Shi, W. Dong, M. Chen and Y. Zhao, *ACS Macro Lett.*, 2017, **6**, 1129-1133.

231   F. Vidal, J. Gomezcoello, R. A. Lalancette and F. Jäkle, *J. Am. Chem. Soc.*, 2019, **141**, 15963-15971.

232   K. Song, W. Ye, X. Gao, H. Fang, Y. Zhang, Q. Zhang, X. Li, S. Yang, H. Wei and Y. Ding, *Mater. Horiz.*, 2021, **8**, 216-223.

233   A. P. Bapat, B. S. Sumerlin and A. Sutti, *Mater. Horizons*, 2020, **7**, 694-714.

234   Y. Yang, F. Du and Z. Li, *ACS Appl. Polym. Mater.*, 2020, **2**, 5630-5640.

235   F. Cavalli, F. R. Bloesser, C. Barner Kowollik and L. Barner, *Chem. Eur. J.*, 2019, **25**, 10049-10053.

236   Y. H. Wang, Z. Y. Cao, Q. H. Li, G. Q. Lin, J. Zhou and P. Tian, *Angew. Chem.*, 2020, **132**, 8080-8090.

237   A. M. Hyde, R. Calabria, R. Arvary, X. Wang and A. Klapars, *Org. Process Res. Dev.*, 2019, **23**, 1860-1871.

238   J. M. Noy, M. Koldevitz and P. J. Roth, *Polym. Chem.*, 2015, **6**, 436-447.

239   T. Zhao, V. P. Beyer and C. R. Becer, *Macromol. Rapid Commun.*, 2020, **41**, 2000409.

240   N. H. Park, G. dos Passos Gomes, M. Fevre, G. O. Jones, I. V. Alabugin and J. L. Hedrick, *Nat. Commun.*, 2017, **8**, 1-7.

241   J. M. Noy, A. K. Friedrich, K. Batten, M. N. Bhebhe, N. Busatto, R. R. Batchelor, A. Kristanti, Y. Pei and P. J. Roth, *Macromolecules*, 2017, **50**, 7028-7040.

242   S. L. Diemer, M. Kristensen, B. Rasmussen, S. R. Beeren and M. Pittelkow, *Int. J. Mol. Sci.*, 2015, **16**, 21858-21872.

243   G. P. Harlow, L. N. Zakharov, G. Wu and S. Y. Liu, *Organometallics*, 2013, **32**, 6650-6653.

244   M. Chen, L. Zhou, Y. Wu, X. Zhao and Y. Zhang, *ACS Macro Lett.*, 2019, **8**, 255-260.

245   Y. Chen, Z. Tang, X. Zhang, Y. Liu, S. Wu and B. Guo, *ACS Appl. Mater. Interfaces*, 2018, **10**, 24224-24231.

246   F. Yang, L. Pan, Z. Ma, Y. Lou, Y. Li and Y. Li, *Polym. Chem.*, 2020, **11**, 3285-3295.

247   W. J. Chung, J. J. Griebel, E. T. Kim, H. Yoon, A. G. Simmonds, H. J. Ji, P. T. Dirlam, R. S. Glass, J. J. Wie and N. A. Nguyen, *Nat. Chem.*, 2013, **5**, 518-524.

248   M. Pagliaro and R. Ciriminna, *J. Mater. Chem.*, 2005, **15**, 4981-4991.

249   J. Keeler, *Understanding NMR spectroscopy*, John Wiley & Sons, 2011.

250   M. J. Baker, J. Trevisan, P. Bassan, R. Bhargava, H. J. Butler, K. M. Dorling, P. R. Fielden, S. W. Fogarty, N. J. Fullwood and K. A. Heys, *Nat. Protoc.*, 2014, **9**, 1771.

251   M. S. H. Akash and K. Rehman, *Ultraviolet-Visible (UV-VIS) Spectroscopy*, Springer Singapore, 2020.

252   W. Zhou, Y. Tang, R. Song, L. Jiang, K. S. Hui and K. Hui, *Mater. Des.*, 2012, **37**, 161-165.

253   J. P. Brutman, P. A. Delgado and M. A. Hillmyer, *ACS Macro Lett.*, 2014, **3**, 607-610.

254   H. Yu, Y. Wang, H. Yang, K. Peng and X. Zhang, *J Mater Chem B*, 2017, **5**, 4121-4127.

Appendix

A. Abbreviations

|	
ABIB	1-Adamantyl 2-bromoisobutyrate
Ad	Adamantane
AIBN	2,2'-Azobis(2-methylpropionitrile)
3-AMPBA	3-Aminophenyboronic acid
AMPTMA	(3-Acrylamidopropyl) trimethylammonium chloride solution
APB	*N*-(6-aminohexyl)-4-(pyren-1-yl) butanamide
APS	Ammonium persulfate
ARS	Alizarin Red S
ATRP	Atom transfer radical polymerization
ATR-IR	Attenuated total reflection-infrared spectroscopy
BDB	2,2′-(1,4-Phenylene)-bis [4-mercaptan- 1,3,2-dioxaborolane]
BPO	Benzoyl peroxide
Bpy	2,2'-Bipyridine
CAN	Covalent adaptable network
CD	Cyclodextrin
$CDCl_3$	Chloroform, deuterated
β-CD-NH$_2$	Mono-6-dexoy-6-(*p*-ethylenediamine)-*β*-CD
CDTPA	4-Cyano-4-[(dodecylsulfanylthiocarbonyl) sulfanyl] pentanoic acid

β-CD-OTs	Mono-6-dexoy-6-(*p*-tolylsulfonyl)-*β*-CD
CNT	Carbon nanotube
Cs$_2$CO$_3$	Cesium carbonate
CTA	Chain transfer agent
CuAAC	Copper catalyzed azide-alkyne cycloaddition
CuBr	Copper(I) bromide
DA reaction	Diels-Alder reaction
DBU	1,8- Diazabicyclo[5.4.0]undec-7-ene
DBN	1,5-diazabicyclo[4.3.0]non-5-ene
DCC	*N,N′*-Dicyclohexylcarbodiimid
DCM	Dichloromethane
DI water	Deionized water
DMA	*N,N*-Dimethyl acrylamide
DMAc	Dimethylacetamine
DMAP	4-(Dimethylamino) pyridine
DMF	Dimethylformamide
DMSO	Dimethyl sulfoxide
DSC	Differential scanning calometry
DTT	Dithiothreitol
EDA	Ethylendiamine
FRP	Free-radical polymerization
FSWCNTs	Functionalized single wall carbon nanotubes

|	
FT-IR	Fourier-transform infrared spectroscopy
GPC	Gel permeation chromatography
HA	Hyaluronic acid
HCl	Hydrochloric acid
HEA	2- Hydroxyethyl acrylate
HMTETA	1,1,4,7,10,10-Hexamethyltriethylenetetramine
HOBt	Hydroxybenzotriazol Hydrate
K_2CO_3	Potassium carbonate
LCR meter	Inductance (L), capacitance (C) and resistance (R) meter
LVE	Linear viscoelastic region
Me_6TREN	Tris[2-(dimethylamino)ethyl]amine
M_n	Number-average molar mass
M_w	Weight-average molar mass
MMA	Methyl methylacrylate
$MgSO_4$	Magnesium sulfate
NaOH	Sodium hydroxide
NaSS	Sodium 4-vinylbenzenesulfonate
NHS	*N*-Hydroxysuccinimide
NMP	Nitroxide-mediated polymerization
NMR	Nuclear magnetic resonance
NOESY	Nuclear overhauser effect spectroscopy
PAMPT	Poly((3-Acrylamidopropyl) trimethylammonium chloride)

PBA	Phenylboronic acid
PBS	Phosphate buffer solution
PEG	Poly(ethylene glycol)
PEO	Poly(ethylene oxide)
PF127	Pluronic F-127
PF127-SH	Thiol-terminated Pluronic F127
PFB	Pentafluoro benzyl
PFP	Pentafluorophenyl
PFPA	Pentafluorophenyl acrylate
PFTR	*Para*-fluoro-thiol reaction
PMDETA	*N,N,N',N'',N''*-Pentamethyldiethylenetriamine
PPM	Post-modification polymerization
PVA	Poly(vinyl alcohol)
Py	Pyrene
Py-*β*-CD	Mono-6-(*2*-pyrenebutylamino)-6-deoxy-*β*-CD
RAFT	Reversible addition-fragmentation chain transfer
RDRP	Reversible-deactivation radical polymerization
SAOS	Small amplitude oscillatory shear testing
SDS	Sodium dodecyl sulfate
SEC	Size exclusion chromatography
SEM	Scanning electron microscopy
SWCNTs	Single wall carbon nanotubes

|	
TBD	1,5,7-Triaza-bicyclo-[4.4.0]dec-5-ene
TEA	Trimethylamine
THF	Tetrahydrofuran
TMEDA	N,N,N',N'-tetramethylethylenediamine
TMS	Tetramethylsilyl group
TPMA	Tris[(2-pyridyl)methyl]amine
TsCl	p-Toluenesulfonyl chloride
UPy	2-Ureido-4-pyrimidone
UV-vis	Ultraviolet-visible

B. Additonal figures of Chapter 4
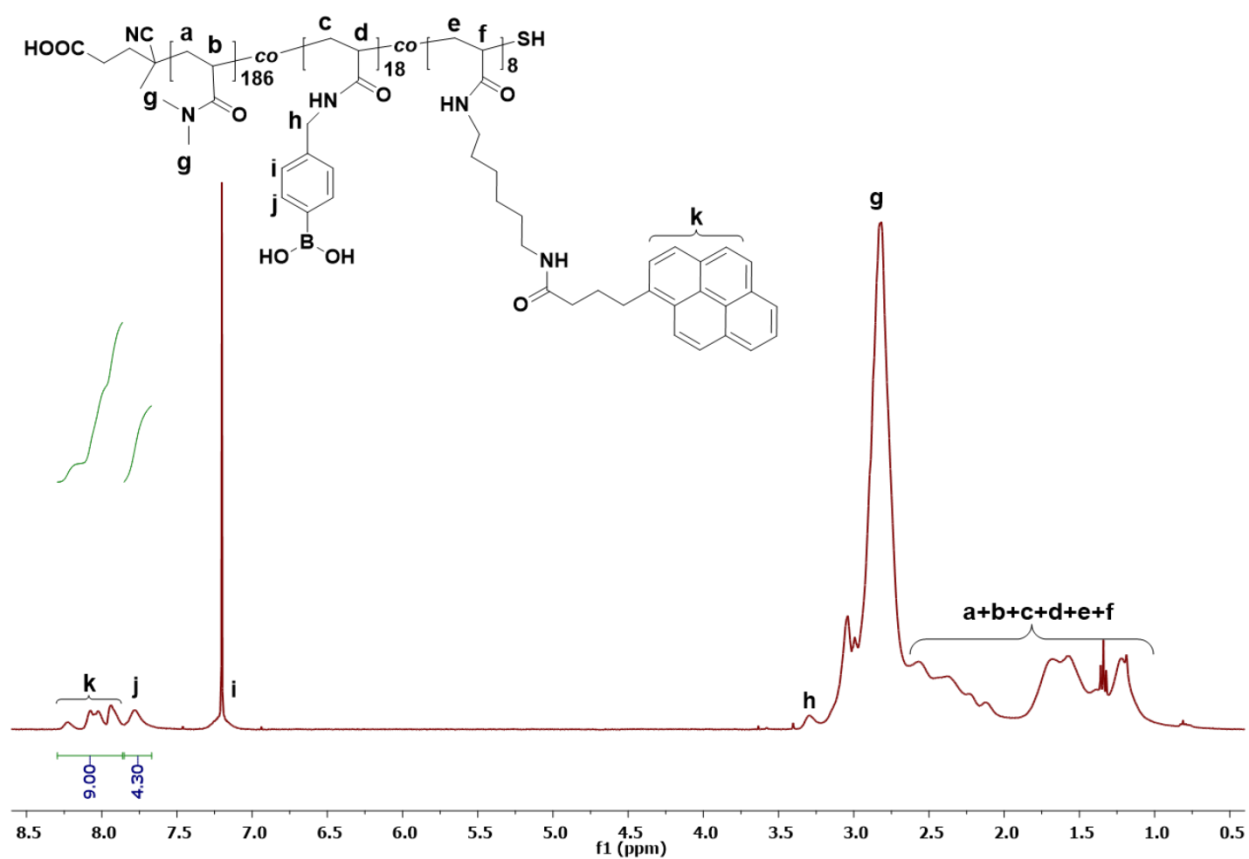
Figure B1. The ^{1}H-NMR (400 MHz, in CDCl$_3$) spectra of P(DMA-*co*-APB-*co*-PBA), i.e. P2, with detailed integral information.
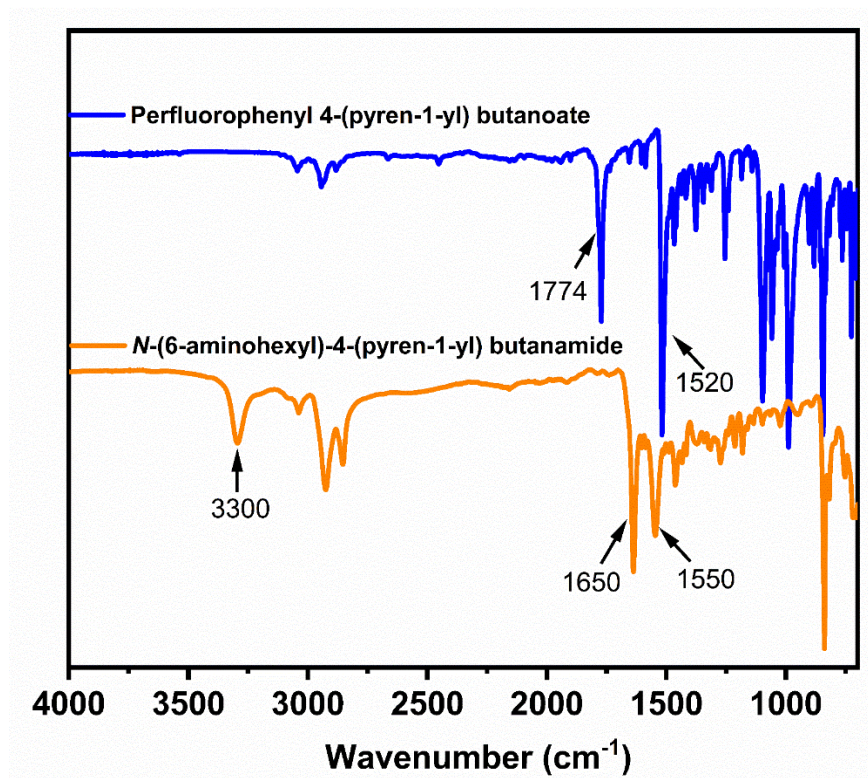
Figure B2. The FT-IR spectra of perfluorophenyl 4-(pyren-1-yl) butanoate and *N*-(6-aminohexyl)-4-(pyren-1-yl) butanamide (APB).
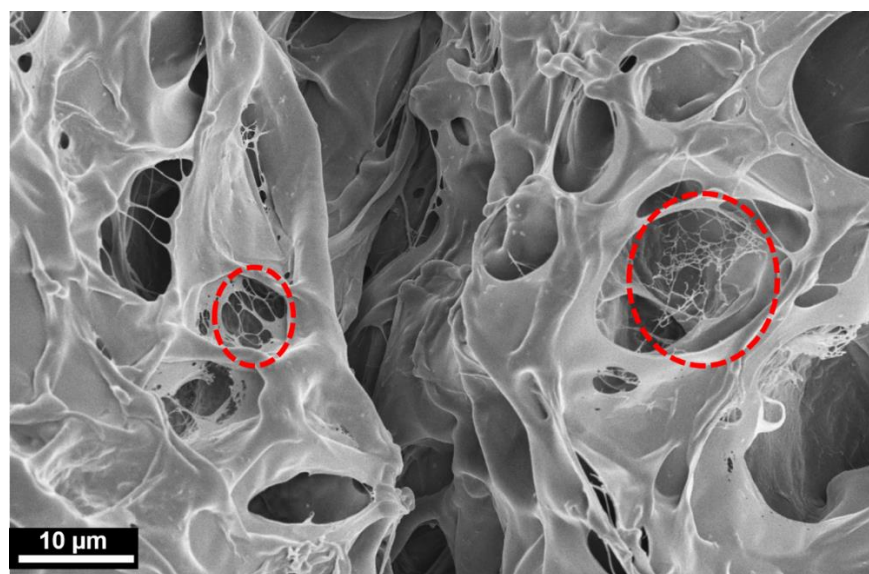
Figure B3. SEM image of the freeze-dried hydrogel formed at neutral pH, and micro-fibrils were highlighted in the red cycles.

C. Additonal figures of Chapter 5
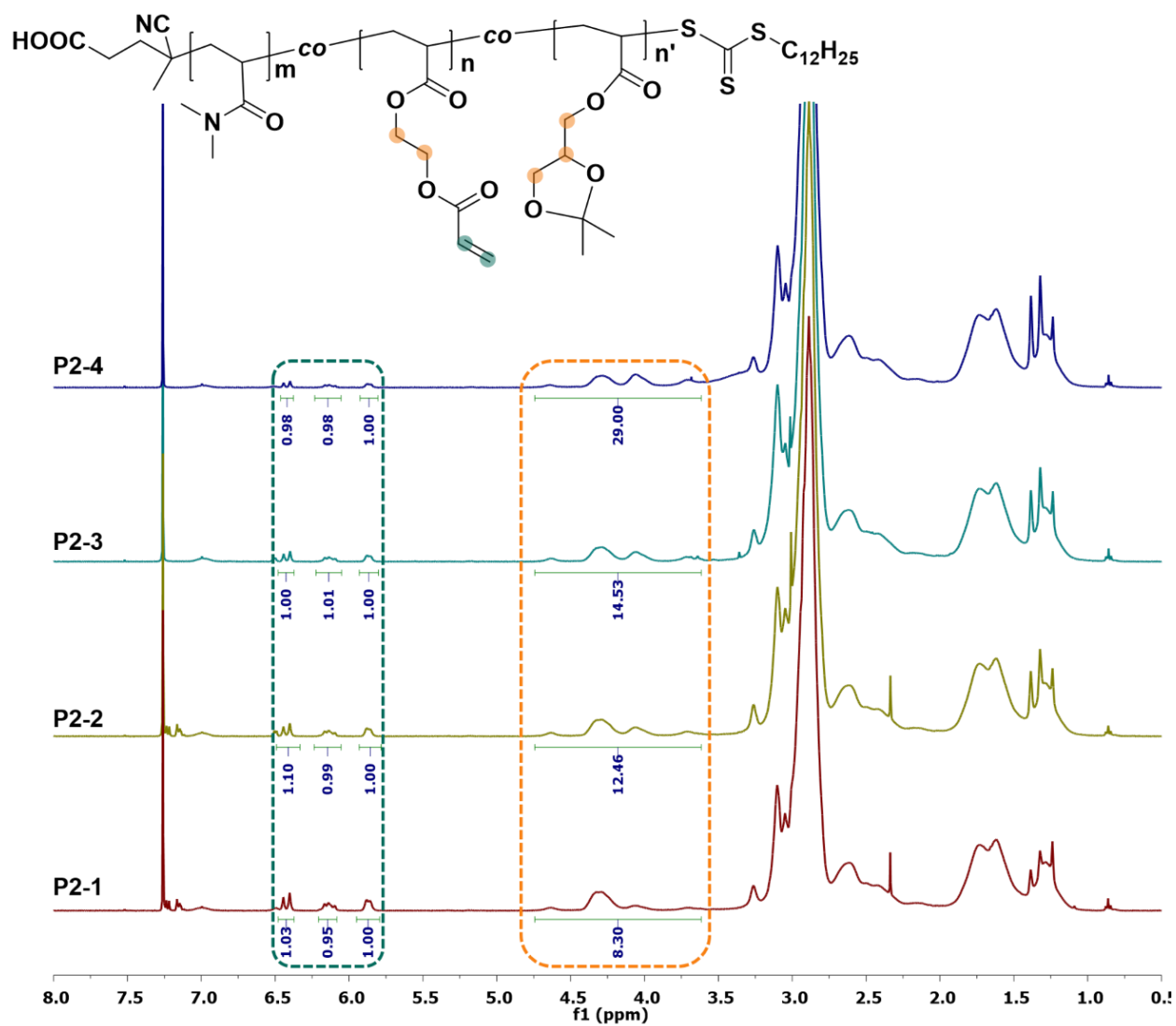
Figure C1. ^{1}H-NMR spectra (400 MHz) of P(DMA-*co*-EDA-*co*-IPA), i.e. P2, with different ratios of EDA: IPA in CDCl$_3$, respectively P2-1, P2-2, P2-3 and P2-4.

Table C1. The molar ratios of EDA : IPA as determined by ^{1}H-NMR spectra in Figure C1 for P2, respectively P2-1, P2-2, P2-3 and P2-4.

Copolymer	Feeding molar ratio (EDA:IPA)	Actual molar ratio[a] (EDA:IPA)
P2-1	60:40	60:51 (1:0.86)
P2-2	40:60	40:67 (1:1.69)
P2-3	30:70	30:63 (1:2.11)
P2-4	20:80	20:100 (1:5.00)

[a] Determined by ^{1}H-NMR spectra in Figure C1

Table C2 Formulations for different specimens containing (P(DMA-*co*-EDA-*co*-DHA)) (P3) with different molar ratios of EDA : DHA (P3-1, P3-2, P3-3 and P3-4 are the deprotection products of P2-1, P2-2, P2-3 and P2-4, respectively) and their corresponding gelation time.

| Specimen	Copolymer	Acrylate: diol: SH: borax[a]	Solid Content	Gelation time
S3-1	P3-1	1:0.86:1:0.17	20%	30"
S3-2	P3-2	1:1.69:1:0.33	20%	58"
S3-3	P3-3	1:2.11:1:0.42	20%	1'50"
S3-4	P3-4	1:5.00:1:1	20%	No gelation

[a] Molar ratio between the acrylate and diol groups was determined by ^{1}H-NMR spectra in Figure C1, and molar ratio of diol and borax was fixed at 5 : 1.
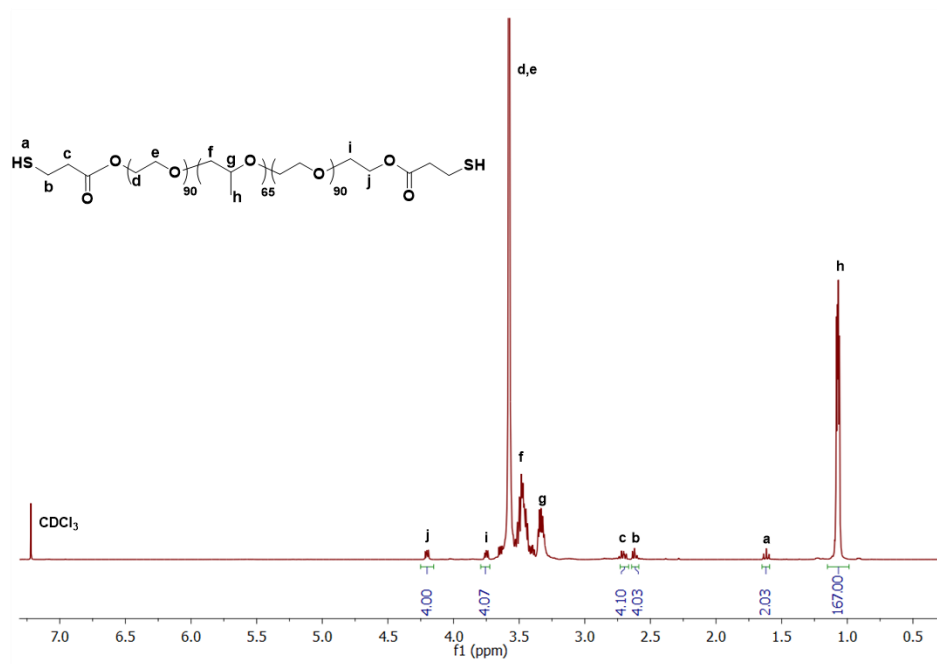
Figure C2. ^{1}H-NMR spectra (400 MHz) thiol-terminated Pluronic F127 (PF127-SH) in CDCl$_3$ with detailed integral information.
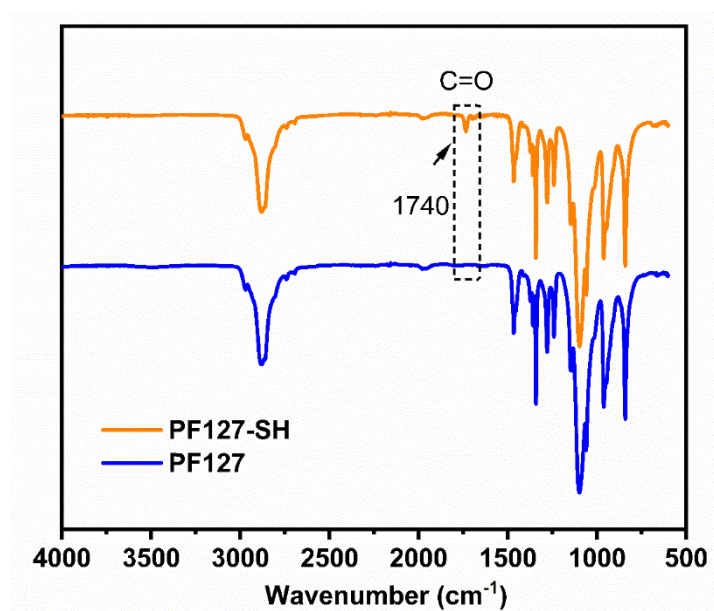
Figure C3. FT-IR spectra of thiol-terminated Pluronic F127 (PF127-SH, upper yellow line) and Pluronic F127 (PF127, bottom blue line).
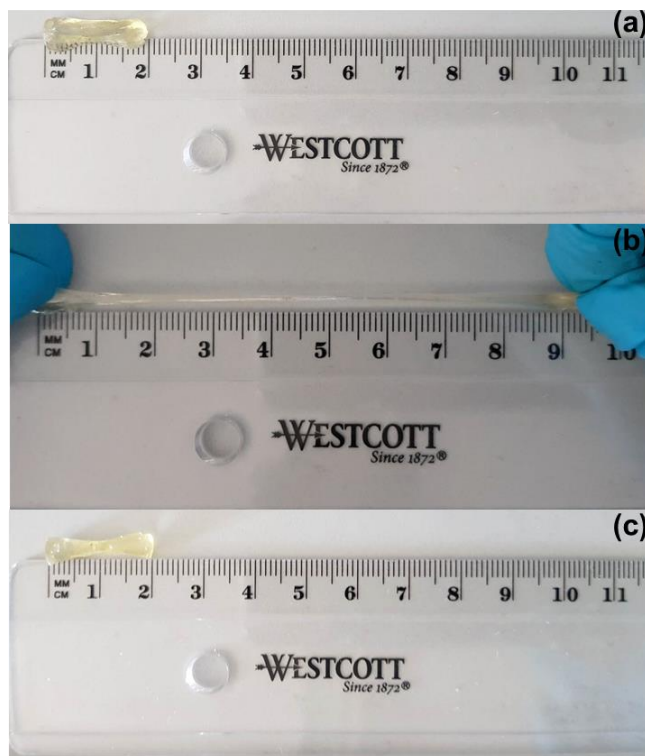
Figure C4. Photograph showing the shape recovery of the hydrogel sample: original sample (a); stretched to around 330 %; (c) after releasing the load for 30 min.
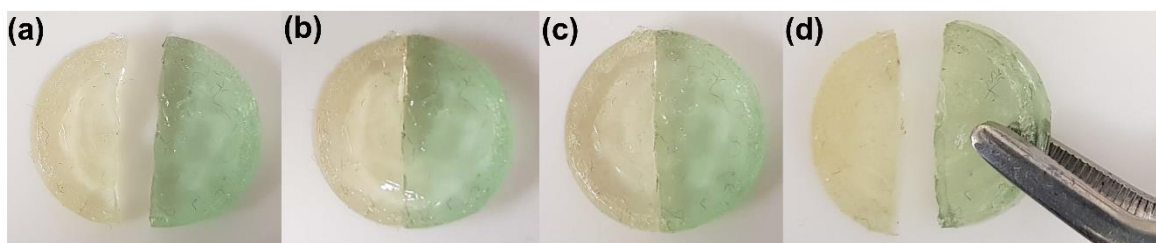
Figure C5. Photograph showing the cut-and-heal tests on P(DMA-*co*-EDA-*co*-IPA) (P2, with designated molar ratio of EDA / IPA =30 : 70) based hydrogel. (a) disk-shaped samples with and without dye were prepared and cut into pieces; (b) two pieces were put into contact; (c) self-healing for 24 h; (d) the two segments failed to integrate into one after 24 h.

Additonal figures of Chapter 6

Calculation of the conversion after the PFTR

The conversion was calculated from ^{19}F-NMR spectra by comparing the integral of parent *ortho*-, *meta*- and *para*-fluorine resonances with their corresponding *ortho'*- and *meta'*-fluorine resonances after PFTR (as shown in **Figure D1**) by using the following **equation (1)**:

$$Coversion\ (c) = \frac{0.5\ m'}{0.5\ m' + p} = \frac{0.5 * 11.34}{0.5 * 11.34 + 1} = 0.85 = 85\% \tag{1}$$

Since the molar feeding ratio of PFB : thiol =1.1 : 1, the theoretical conversion was calculated to be 90.9%. Therefore, the experimental conversion was nearly equal to its theoretical one.
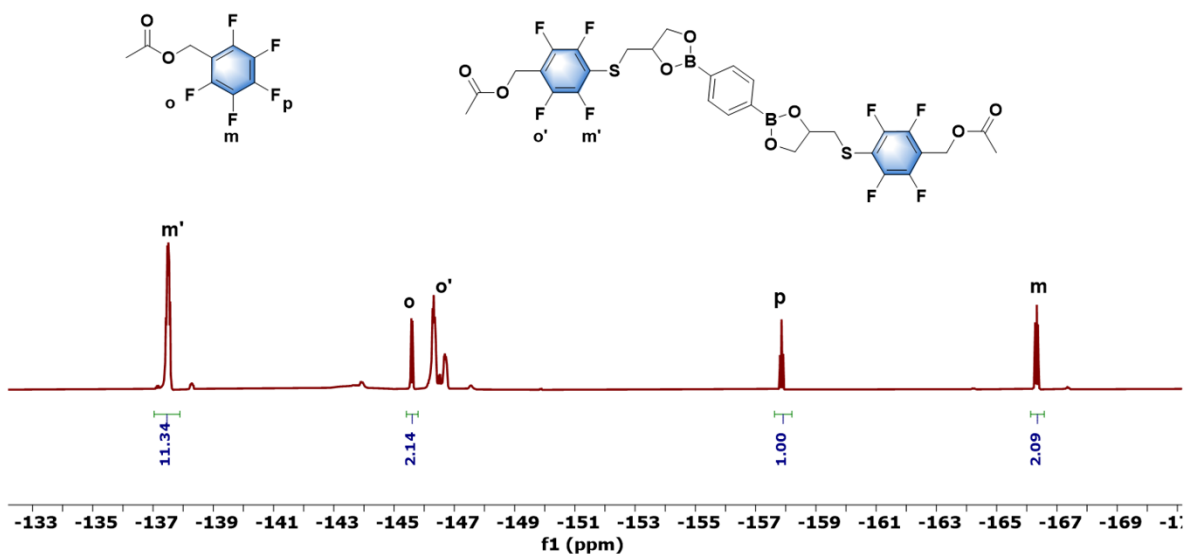

Figure D1. ^{19}F-NMR spectra (377 MHz) of the model reaction via DBU-catalyzed PFTR in THF-*d*8.

134
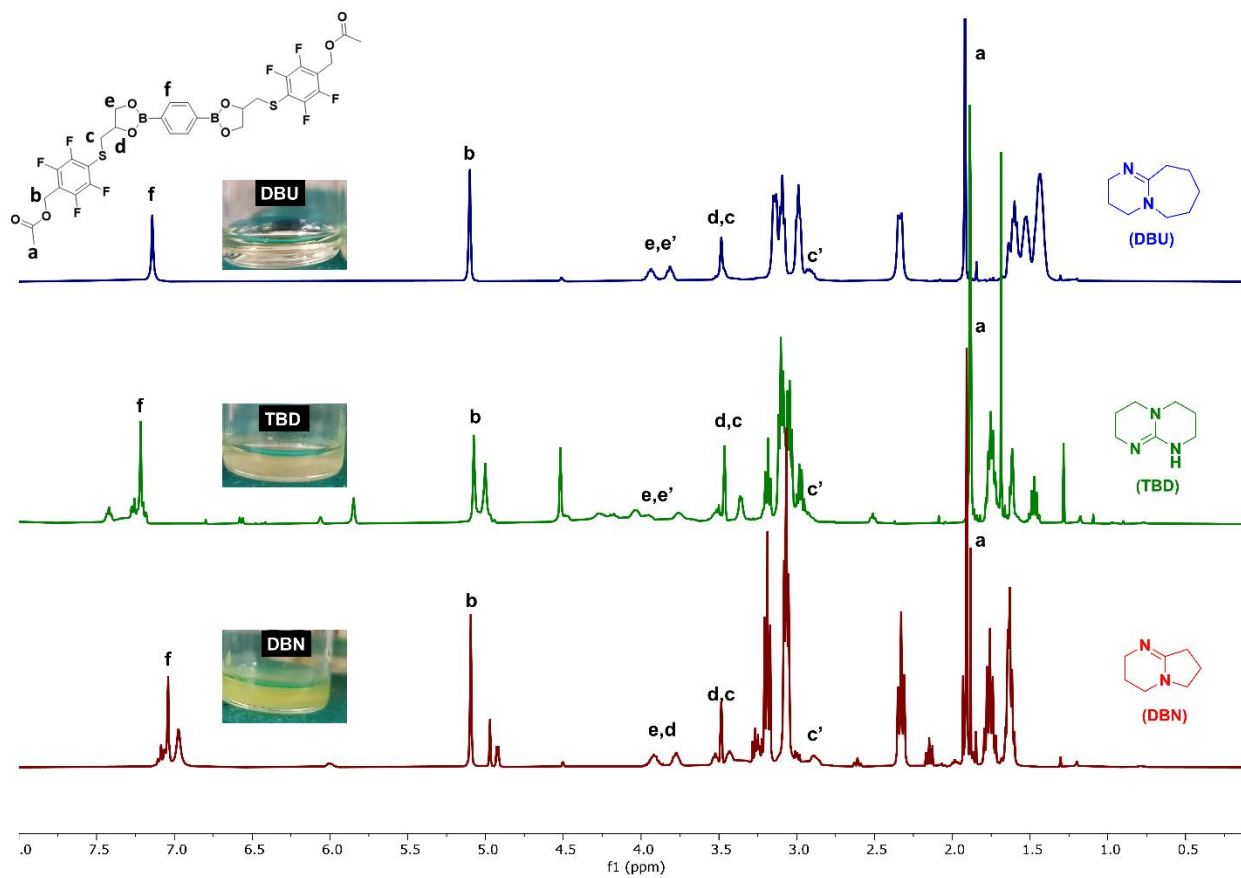
Figure D2. ^{1}H-NMR spectra (400 MHz) of the model reaction by the catalyst of DBU (blue line), TBD (green line) and DBN (red line) in THF-d_8, respectively. Insert pictures are the PFTR products in THF. From top to bottom, are the DBU, TBD and DBN catalyzed PFTR, respectively. Precipitation of a yellow gel occurred in TBD and DBN catalyzed PFTR, while the solution was transparent with the catalyst of DBU.
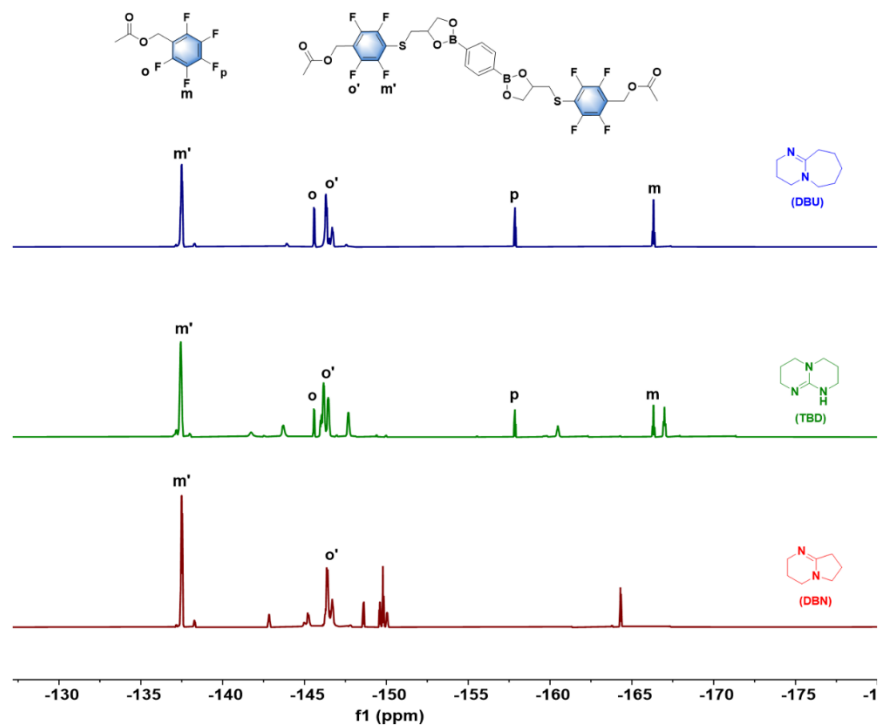
Figure D3. ^{19}F-NMR spectra (377 MHz) of the model reaction by the catalyst of DBU (blue line), TBD (green line) and DBN (red line) in THF-d_8, respectively. The resonance peaks were only identifiable for the DBU-catalyzed PFTR, while some additional peaks of TBD- and DBN-catalyzed products couldn't be assigned due to the side reactions on *ortho-* and *meta*-fluorine positions.
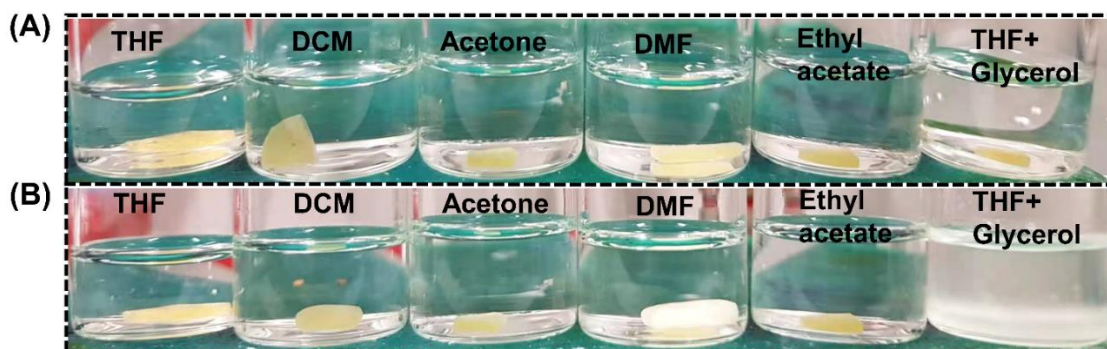
Figure D4. The solvent resistance tests of 3PFB-CN network. (A) the sample was immersed into a variety of organic solvent and (B) at room temperature after 24 h. The as-fabricated polymeric network wasn't dissolved but swollen in common organic solvents, i.e. THF, DCM, Acetone, DMF, Ethyl acetate, but dissolved into the THF/Glycerol mixture solution.

Scientific Production

List of Publications

1. **Xiaohui Li**, Xia huang, Hatice Mutlu, Sharali Malik and Patrick Theato*. Conductive hydrogel composites with autonomous self-healing properties. *Soft Matter*, 2020, **16**, 10969-10976.

2. **Xiaohui Li**, Hatice Mutlu, Christian Fengler, Manfred Wilhelm and Patrick Theato*. Dual-faced borax mediated synthesis of self-healable hydrogels merging dynamic covalent bonding and micellization. *Polymer Chemistry*, 2021, **12**, 361-369.

3. **Xiaohui Li**, Hatice Mutlu, Shouliang Nie, Manfred Wilhelm and Patrick Theato*. Two in one: Fusion of dynamic boronic ester bonds via para-fluoro-thiol reaction towards malleable and self-healable heteroatom-rich covalent polymer networks. *Polymer Chemistry*, submitted.

4. **Xiaohui Li**, Hatice Mutlu and Patrick Theato*. Conductive and self-healable hydrogel composites based on host-guest and electrostatic interactions. In preparation.

5. Hatice Mutlu, Ezgi Berfin Ceper, **Xiaohui Li**, Jingmei Yang, Wenyuan Dong, Mehmet Murat Ozmen, Patrick Theato*. Sulfur Chemistry in Polymer and Materials Science. *Macromolecular rapid communications*, 2019, **40**, 1800650.

Conference contributions

2018 *Biennial Meeting of the GDCh-Division of Macromolecular Chemistry, Karlsruhe (DE)*

Poster presentation: Conductive hydrogel composites with autonomous self-healing properties.

Acknowledgements

First, I would express my gratitude to my supervisor Prof. Dr. Patrick Théato for his dedicated mentoring through each stage of my PhD study. Thank you so such for offering the precious opportunity to join the great research group and work on the interesting topics. I am really grateful for your continuous guidance on my research work, from the beginning design of experiment to the final revise on scientific articles.

Furthermore, I would like to thank Prof. Dr. Pavel Levkin for his acceptance to be my co-referee of my thesis and I really appreciate the time he contributed for reviewing my thesis.

I would like thank to Dr. Hatice Multu for her endless support in my research work. She is somehow the real "Wonder Woman" in academic fields, who is always ready to address our problems. Thank you so much, not only for teaching me all the practical skills in scientific writing, but also being a real model for me to learn how to be an independent woman.

I want to acknowledge my collaboration partners. I want to thank Dr. Sharali Malik for providing the SWCNTs and helping me with the SEM pictures. I want to thank Dr. Shouliang Nie and Christian Fengler for their support in rheology measurements and fruitful discussions on my project.

I would like to thank the whole group members in KIT. Special thanks to our technician Katharina Elies. Thanks for your help with chemical ordering, lab safety training, as well as your support in DSC and GPC measurements. Thanks Yunji, Martin, Stefan and Andy for your help with NMR measurements. Thanks Johannes for your support in Campus North. Thanks Sergej for your support in GPC measurements and practical lab course. Thanks Dr. Xia Huang for your help in SEM images, your company from lab to office, and also the awesome food you cooked. I would like also thanks Dr. Dominik Voll, Dr. Wenwen Xue, Dr. Miriam Khodeir, Dr. Yosuke Akae, Meryem, Victoria, Edgar, Marvin, David, Vaishali, Isabella, Wenyuan and Hongxin *et al.*, thanks all for your support in the last three years and I really appreciate the time to work with you.

I would like to thank all my colleagues in Hamburg. Special thanks to Prof. Shaojian Lin and Prof. Jiaojiao Shang, thanks for your selfless support and guidance on both my life and research work, which helped me pass the tough start in Hamburg smoothly. I would thank to Dr. Xiaoxiao Zhang, Dr. Tim Krappitz, Dr.

Alexander Hoefling, Dr. Michael W. Thielke, Dr. Heba Gaballa, Julia Steicke, Fenja Moldenhauer, Sven and Xinyang, thanks all for your help in Hamburg and it's really nice to work with you.

Last but not least, my deepest gratitude is dedicated to my beloved parents and husband. Thanks for your heartfelt care and encourage, you're always my spiritual support whatever I do and wherever I go.

Thanks all the people who showed up during the last four years, it's you to make my journey in Germany meaningful and unforgettable.